Charles University in Prague
Faculty of Mathematics and Physics

DOCTORAL THESIS

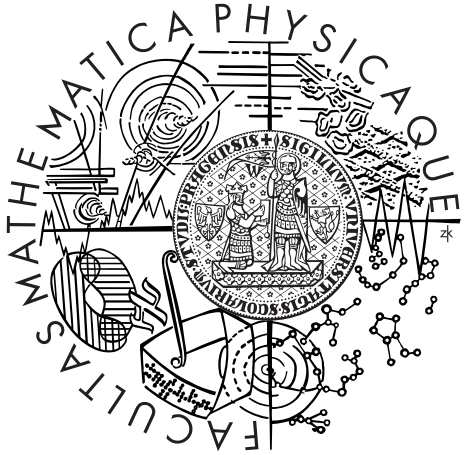

Eliška Zábranová

Numerical modeling of free oscillations applied to superconducting-gravimeter data in a low-frequency seismic range

Department of Geophysics

Supervisor of the doctoral thesis: Doc. RNDr. Ctirad Matyska, DrSc.

Study programme: Physics

Specialization: Geophysics

Prague 2015

First, I would like to thank my supervisor Doc. Ctirad Matyska for his inspiring leadership, patience and courage to share with me the adventures in the field of seismology. I am grateful to Dr. Ladislav Hanyk for his guidance in implementing the matrix eigenvalue approach and invaluable help with finalizing this thesis. I am very thankful to Dr. František Gallovič and Prof. Jiří Zahradník for long, inspiring and fruitful discussions, Dr. Jakub Velímský and Mgr. Ľubica Valentová for their help with technical stuff and broad support, and Dr. Ondřej Šrámek for English corrections of this thesis. My thanks also belong to Dr. Vladimír Plicka, Dr. Vojtech Pálinkáš and Dr. Miloš Vaľko who afforded me the seismic and gravimetric data from the Geodetic Observatory Pecný, introduced me to the data processing and thus helped me to advance my research from pure theoretical level.

My special thanks belong to all nice people at the Department of Geophysics in Prague for the friendly atmosphere. I am grateful to the Research Institute of Geodesy, Topography and Cartography for their support within the Center for Earth Dynamic Research and, especially, its head Prof. Jan Kostelecký. I would like to express my deepest gratitude to all that provided the gravimetric data through the Global Geodynamic Project. The work was supported by the Grant Agency of the Czech Republic under the project No. 14–04372S.

I declare that I carried out this doctoral thesis independently, and only with the cited sources, literature and other professional sources.

I understand that my work relates to the rights and obligations under the Act No. 121/2000 Coll., the Copyright Act, as amended, in particular the fact that the Charles University in Prague has the right to conclude a license agreement on the use of this work as a school work pursuant to Section 60 paragraph 1 of the Copyright Act.

In Prague 18. 05. 2015 Eliška Zábranová

Název práce: Modelování vlastních kmitů Země použité na data ze supravodivých gravimetrů v nízkofrekvenční seismické oblasti

Autor: Eliška Zábranová

Katedra: Katedra geofyziky

Vedoucí disertační práce: Doc. RNDr. Ctirad Matyska, DrSc.

Abstrakt: Deformace a změna gravitačního potenciálu předpjatých selfgravitujících elastických těles jsou popsány momentovou a Poissonovou rovnicí a reologickým vztahem. V případě sféricky symetrických těles převádíme tyto parciální diferenciální rovnice a okrajové podmínky pomocí sférické harmonické dekompozice na obyčejné diferenciální rovnice druhého řádu, pro jejichž diskretizaci používáme pseudospektrální diferenční schémata na sítích čebyševovského typu. Dospíváme tak k soustavě maticových úloh pro vlastní frekvence a vlastní funkce kmitů. Protože elastické parametry jsou frekvenčně závislé, řešíme problém pro několik výchozích frekvencí modelu a výsledky interpolujeme. Získané vlastní frekvence a vlastní funkce porovnáváme s výsledky programu Mineos, který je založen na přímé numerické integraci. Pomocí naší metody počítáme nízkofrekvenční syntetické akcelerogramy nedávných velkých zemětřesení, které porovnáváme s daty ze supravodivých gravimetrů. Z těchto záznamů po zemětřeseních Maule 2010 a Tohoku 2011 určujeme faktory kvality nejdelších radiálních módů, které použijeme pro vymezení velikostí složky M_{rr} momentového tenzoru. Mód ${}_0S_0$ poskytuje relativně úzký interval hodnot M_{rr}, zatímco mód ${}_1S_0$ je více citlivý na hloubku centroidu. V následné inverzi pak společně určujeme faktory kvality nejdelších sféroidálních módů a tři nízkofrekvenční složky momentového tenzoru, který pozorovaný signál generuje. Abychom dosáhli lepšího rozlišení vlivu faktorů kvality a složek momentového tenzoru, používáme nejdříve několikadenní záznamy a získané faktory kvality potom využíváme při inverzi složek momentového tenzoru z kratších záznamů. Vzájemný rozdíl obou inverzí je přitom menší než rozdíly složek momentových tenzorů rutinně poskytovaných různými seismickými agenturami.

Klíčová slova: vlastní kmity, pseudospektrální diferenční schémata, data ze supravodivých gravimetrů, faktory kvality, inverze momentového tenzoru

Title: Numerical modeling of free oscillations applied to superconducting-gravimeter data in a low-frequency seismic range

Author: Eliška Zábranová

Department: Department of Geophysics

Supervisor: Doc. RNDr. Ctirad Matyska, DrSc.

Abstract: Deformations and changes of the gravitational potential of prestressed selfgravitating elastic bodies caused by free oscillations are described by means of the momentum and Poisson equations and the constitutive relation. For spherically symmetric bodies we transform the equations and boundary conditions into ordinary differential equations of the second order by the spherical harmonic decomposition and further discretize the equations by highly accurate pseudospectral difference schemes on Chebyshev grids. We thus receive a series of matrix eigenvalue problems for eigenfrequencies and eigenfunctions of the free oscillations. Since elastic parameters are frequency dependent, we solve the problem for several fiducial frequencies and interpolate the results. Both the mode frequencies and the eigenfunctions are benchmarked against the output from the Mineos software package based on Runge-Kutta integration techniques. Subsequently, we use our method to calculate low-frequency synthetic accelerograms of the recent megathrust events and compare them with the observed superconducting-gravimeter (SG) data. We estimate the quality factors of the longest radial modes directly from the SG records of the 2010 Maule and 2011 Tohoku earthquakes and then constrain the M_{rr} component of the centroid moment tensors. The ${}_0S_0$-mode amplitude enables one to obtain a relatively narrow interval of M_{rr} values, whereas the ${}_1S_0$-mode amplitude is more sensitive to the centroid depth. We also invert the SG data to jointly determine quality factors of the gravest spheroidal modes and the three low-frequency centroid-moment-tensor (CMT) components that generate the observed signal. We employ several-day records to better resolve both the quality factors and the CMT components and, with the already inverted quality factors and substantially shorter records, we obtain new estimates of the CMT components. The differences in CMT components calculated from the long and short records are smaller than those routinely produced by different seismic agencies.

Keywords: Free oscillations, matrix eigenvalue problem, superconducting-gravimeter data, quality factors, CMT inversion

Contents

Introduction

Normal modes or free oscillations are components of standing waves with an infinite number of degrees of freedom that are created from the constructive interference of body and surface waves circling the Earth multiple times. For the commonly used spherically symmetric, non-rotating, perfectly elastic and isotropic (SNREI) Earth model the oscillations are composed of two distinct types of modes. The spheroidal modes ${}_nS_l$ correspond to standing Rayleigh waves and change the external shape and internal density of the body, and the toroidal modes ${}_nT_l$ correspond to standing Love waves with purely tangential displacements and leave the shape and the radial density distribution unaffected. The modes are labelled by the angular degree $l = 0, \ldots, \infty$ of spherical harmonic decomposition and the prefix overtone number $n = 0, \ldots, \infty$ since there is an infinite number of spheroidal and toroidal modes with angular frequencies ${}_n\omega_l^{\mathrm{S}}$ and ${}_n\omega_l^{\mathrm{T}}$ for a given value of l. In the case of a SNREI model, each of the ${}_nS_l$ and ${}_nT_l$ modes represents a multiplet containing $2l+1$ oscillations of the same frequency. This $2l+1$ degeneracy is a mathematical consequence of the model spherical symmetry. When a slightly anelastic model is considered, each multiplet is attenuated with time; the exponential decrease of modal amplitudes is described by quality factors.

Free oscillations provide information about both the internal structure of the Earth and the mechanism of a source event (earthquake, impact etc.) since the periods of the modes are given by model parameters and the amplitudes depend on the source event. Gilbert and Dziewonski (1975) employed 1064 measured eigenfrequencies of normal modes and mass and moment of inertia to derive two models of Earth parameters, 1066A and 1066B. Afterwards, the periods of about one thousand normal modes and about one hundred normal-mode quality-factor values were used in addition to travel time observations in constructing the Preliminary Reference Earth Model (Dziewonski and Anderson, 1981) that still represents the fundamental spherically symmetric seismic model of the Earth. The study of free oscillations brought the ultimate evidence of the inner-core being solid (Dziewonski and Gilbert, 1971) and anisotropic (Woodhouse et al., 1986; Tromp, 1993; Romanowicz and Bréger, 2000), and contributed to our appreciation of the large-scale lateral variations of the Earth structure (e.g., Jobert et al., 1978; Masters et al., 1982; Romanowicz and Roult, 1986).

The diversity of normal-mode periods enables us to study the Earth parameters in broad frequency and spatial ranges. The gravest modes with periods over 15 minutes are largely unaffected by local structures, so they provide information about the distribution of seismic velocities, density and attenuation with depth, averaged over the Earth, while the shorter modes bring information about lateral heterogeneities and anisotropy.

Free oscillations also become important in constraining the seismic-source properties of very large earthquakes where the frequency content of the source processes shifts to lower frequencies and determination of seismic moment using high-frequency data becomes problematic. The 2004 Sumatra-Andaman earthquake is a recent example where the standard seismological routines based on the body and surface waves (with periods of several hundred seconds) undervalued the energy released during the rupture process. On the basis of the free-oscillations analysis Park et al. (2005) showed that the seismic scalar moment M_0 was at least 1.5 times higher than the value inferred from the Global Centroid Moment Tensor (GCMT) solution based on routine procedures.

The normal modes were for the first time observed without any doubt in the seismic records following the 1960 Chilean earthquake with moment magnitude of 9.5. However, the idea of normal modes was not new as the theoretical description of this phenomenon appeared more than a century ago. The normal modes of a self-gravitating homogeneous solid sphere were discussed for example by Love (1911), who included a historical perspectives:

> *The theory of the free vibrations of a homogeneous isotropic elastic solid sphere was studied very completely by H. Lamb in 1882. At that time very little was known about the propagation of seismic waves, but, as observations concerning these were accumulated, it became increasingly desirable to discover the modifications that should be made in the theory in order to take into account the effects that might be due to the mutual gravitation of the parts of the sphere and those that might be due to the compressibility of its substance. The effects due to mutual gravitation were first investigated by T. J. I'A. Bromwich, but his investigation was incomplete in the sense that he took the material to be incompressible. Apart from their importance in connexion with the propagation of earthquake shocks, the free vibrations of the earth, considered as a deformable body, have a bearing on the theory of earth tides.*

Pekeris and Jarosch (1958) obtained the equations that are still used today. The complete theory for the Earth with arbitrary parameters and with an initial static stress field was published by Dahlen (1972), who derived linearized equations of motion and linearized boundary and continuity conditions governing small elastic-gravitational disturbances away from an equilibrium state of an arbitrary, uniformly rotating, self-gravitating, perfectly elastic Earth model with an arbitrary initial static stress field.

The traditional approach of computing eigenfrequencies and eigenfunctions of the SNREI model is based on the Runge-Kutta numerical integration of six (two) ordinary differential equations of the first order in the case of spheroidal (toroidal) oscillations. A computer program to solve these equations was written by J. F. Gilbert around the year 1966. Two successive programs arose from Gilbert's code: John Woodhouse's Obani and Guy Masters' Mineos. In order to compare our results, we use the Mineos software package available online at http://geodynamics.org/cig/software/mineos/.

Instead of the Runge-Kutta numerical integration, we have developed a different approach where the direct numerical discretization of the ordinary differential equations by high-accuracy pseudospectral schemes (Fornberg, 1996) leads to a se-

ries of matrix eigenvalue problems for evaluating eigenfrequencies and eigenfunctions (Zábranová et al., 2009). Our method is a modification of Hanyk et al. (2002) where similar ordinary differential equations are solved for postglacial rebound. Note that, according to their statement, our approach was adopted by the geodetic group from the Institute of Seismological Research, Department of Science & Technology Government of Gujarat (Annual report 2011-12, pp. 89–90).

Development of the new numerical method for normal-mode calculations represents only one part of this thesis. The other part is devoted to data analysis of the gravest normal modes. In the 1970s the worldwide network of the LaCoste-Romberg gravimeters (International Deployment of Accelerometers, IDA) was launched to monitor very-long-period phenomena (Agnew et al., 1976), especially Earth tides and free oscillations. This network was subsequently enriched by long-period seismometers (> 60s) with better parameters than spring gravimeters. Analyses of the IDA data allowed seismologists to study source effects and Earth structure at long periods, led to better models of anelasticity of the Earth and brought information about mode splitting (Buland et al., 1979; Agnew et al., 1986). Successively the network of superconducting gravimeters (SG) was created to observe seismic normal modes, the Slichter triplet, tidal gravity, ocean tidal loading, core nutations and core modes within the framework of the Global Geodynamics Project (GGP), an international program of observations of temporal variations in the Earth gravity field (Crossley et al., 1999).

While older studies have shown that the SGs were not as good as the STS-1 seismometers in the seismic band (Freybourger et al., 1997; Van Camp, 1999), the new generation of SG instruments achieved lower noise levels than any other sensor at frequencies below 0.8 mHz (Widmer-Schnidrig, 2003). Nevertheless, the longest Slichter oscillations with periods about five hours, first highlighted by Slichter (1961), have not yet been discovered with certainty in the records, in spite of the fact that the SG precision is lower than 1 nGal. The SGs are thus the most suitable instruments to detect small signals expected for the Slichter triplet ${}_1S_1$ (Hinderer et al., 1995; Rosat et al., 2003; Rosat et al., 2004). Since the ${}_1S_1$ period directly relates to the density jump at the inner-core boundary, the hunt for convincing proofs of the existence of this fundamental mode still continues (e.g., Smylie, 1992; Smylie et al., 1992; Ding and Shen, 2013a), as do debates about its excitation (e.g., Rosat, 2007; Rosat and Rogister, 2012), computation of the periods (e.g., Rogister, 2003; Grinfeld and Wisdom, 2010), influence of viscosity in the outer core (e.g., Smylie and McMillan, 2000; Rieutord, 2002) and other topics (e.g., Crossley, 1992; Rochester and Peng, 1993).

Nevertheless, observations of fundamental low-frequency modes other than the Slichter triplet are of excellent quality and new SG data enable us to solve a variety of other problems. In this thesis we chose the SG records of the 2010 Maule, 2011 Tohoku and 2012 Sumatra earthquakes in the frequency range below 1 mHz. Since source durations of these earthquakes are shorter than 200 s and the characteristic rupture lengths are smaller than 500 km, we can securely use the point-source approximation in this frequency range.

As we know from the normal-mode perturbation theory (e.g., Backus and Gilbert, 1961; Dahlen, 1968; Dziewonski and Sailor, 1976; Woodhouse and Dahlen, 1978), the free oscillations of the Earth are split by rotation, ellipticity and lateral heterogeneity. In applications to source-mechanism problems we follow the study by

Dahlen and Sailor (1979). Splitting of the low-frequency modes is almost insensible to the 3-D structure of the Earth (e.g., He and Tromp, 1996). The new observations of the gravest spheroidal modes by SGs can thus be modelled straightforwardly by taking into account multiplet splitting due to only rotation and ellipticity. These observations yield constraints that can be used to obtain low-frequency limits of the source mechanism together with new estimates of the quality factors of these modes, which we discuss in detail in the second part of this thesis. We also focused on the radial modes ${}_0S_0$ and ${}_1S_0$. Since they are not degenerated, their quality factors can be directly determined from records and the moment tensor inversion can be performed separately. Our results have already been cited by Mitsui and Heki (2012), Ding and Shen (2013b) and Bogiatzis and Ishii (2014).

Part I provides theoretical background for normal-mode computations and SG data processing of three megathrust earthquakes from the last decade. In Chapter 1 we introduce the matrix eigenvalue approach that enables us to calculate the normal-mode frequencies and eigenfunctions. The adopted formulas that describe the response of an (an)elastic, (a)spherical and (non)rotating Earth to seismic events are listed in Chapter 2. In Chapter 3 we present the SG data processing, specify the three studied events and use the SG data to constrain the low-frequency moment tensors and quality factors.

Part II consists of the three articles (Zábranová et al., 2012a; Zábranová et al., 2012b; Zábranová and Matyska, 2014) published in international scientific journals (these articles contain their separate reference lists). In Chapter 4 we deal with the seismic and gravity records from the Geodetic Observatory Pecný after the 2011 Tohoku earthquake and compare them with the synthetic records for several point- and finite-source agency solutions. Chapter 5 is devoted to the radial modes generated by the 2010 Maule and 2011 Tohoku earthquakes. We found the quality factors of the three longest radial modes using the GGP data and subsequently constrained the moment tensors of both earthquakes. In Chapter 6 we introduce the joint inversion of the quality factors of four fundamental spheroidal modes and the moment-tensors components of the 2010 Maule and 2011 Tohoku earthquakes again using GGP data.

Part I

Computational methods and SG data

Chapter 1

Matrix eigenvalue approach

1.1 Governing partial differential equations

In this section we formulate the partial differential equations (PDEs) and the boundary conditions, which describe the response of a prestressed selfgravitating elastic body to a seismic source or external gravitational force, i.e., the temporal behavior of the displacement and the incremental gravitational potential in the entire body. The reference unperturbed state of our model—the hydrostatic equilibrium—is described by the momentum equation,

$$\nabla \cdot \boldsymbol{\tau_0} + \boldsymbol{f_0} = \mathbf{0}, \tag{1.1}$$

where $\boldsymbol{\tau_0}$ represents the Cauchy stress tensor, the forcing term satisfies $\boldsymbol{f_0} = -\rho_0 \nabla \varphi_0$ and ρ_0 is the reference density. The hydrostatic gravitational potential φ_0 satisfies the Poisson equation,

$$\Delta \varphi_0 = 4\pi G \rho_0, \tag{1.2}$$

where G is the Newton gravitational constant. The boundary conditions in the reference state, required at the surface and all internal boundaries, are the continuity of the normal traction, the gravitational potential and the normal component of its gradient; moreover, the tangential traction vanishes at the free surface and liquid boundaries.

The complete system of PDEs for the Lagrangian displacement $\boldsymbol{u}$, the Eulerian incremental gravitational potential φ and the incremental stress tensor $\boldsymbol{\tau}$ consists of the momentum equation, the Poisson equation and the constitutive relation,

$$\begin{aligned} \nabla \cdot \boldsymbol{\tau} - \rho_0 \nabla \varphi + \nabla \cdot (\rho_0 \boldsymbol{u}) \nabla \varphi_0 - \nabla (\rho_0 \nabla \varphi_0 \cdot \boldsymbol{u}) &= \rho_0 \frac{\partial^2 \boldsymbol{u}}{\partial t^2}, & (1.3) \\ \nabla \cdot (\nabla \varphi + 4\pi G \rho_0 \boldsymbol{u}) &= 0, & (1.4) \\ \lambda \nabla \cdot \boldsymbol{u} \boldsymbol{I} + \mu \left[\nabla \boldsymbol{u} + (\nabla \boldsymbol{u})^{\mathrm{T}} \right] &= \boldsymbol{\tau}, & (1.5) \end{aligned}$$

where λ and μ are the elastic Lamé parameters, the latter also referred to as the shear modulus. This Lagrangian-Eulerian system of equations can be found in, e.g., Martinec (1984) or Dahlen and Tromp (1998).

Lagrangian boundary conditions have to be added to the PDEs (1.3)–(1.5) on the surface of the model and on the internal boundaries. On a boundary of two solid

layers (called "solid boundary" from now on) the displacement and the incremental traction are continuous,

$$[\boldsymbol{u}]^+_- = \boldsymbol{0}, \tag{1.6}$$
$$[\boldsymbol{\tau}\cdot\boldsymbol{n}]^+_- = \boldsymbol{0}, \tag{1.7}$$

where $\boldsymbol{n}$ is the unit vector normal to the boundaries. On a boundary of the solid and liquid layers (called "liquid boundary" from now on) the normal component of both the displacement and incremental traction are continuous and the tangential components of the traction vanish,

$$[\boldsymbol{u}\cdot\boldsymbol{n}]^+_- = 0, \tag{1.8}$$
$$[\boldsymbol{\tau}\cdot\boldsymbol{n}\cdot\boldsymbol{n}]^+_- = 0, \tag{1.9}$$
$$\boldsymbol{\tau}-(\boldsymbol{\tau}\cdot\boldsymbol{n})\,\boldsymbol{n} = \boldsymbol{0}. \tag{1.10}$$

Let us emphasize that the relation (1.10) represents four independent equations since it holds on each side of the boundary. On the free surface both the normal and tangential components of the incremental traction vanish,

$$\boldsymbol{\tau}\cdot\boldsymbol{n} = \boldsymbol{0}. \tag{1.11}$$

As this is a Neumann boundary condition, we must also exclude total translation and rotation of the body. The incremental gravitational potential tends to zero in infinity,

$$\varphi(r\to\infty)=0. \tag{1.12}$$

On all boundaries the Eulerian incremental potential is continuous, whereas the normal component of its gradient can be discontinuous because the boundary undulations are replaced by apparent surface mass densities,

$$[\varphi]^+_- = 0, \tag{1.13}$$
$$[\nabla\varphi\cdot\boldsymbol{n}+4\pi G\rho_0\boldsymbol{u}\cdot\boldsymbol{n}]^+_- = 0. \tag{1.14}$$

This way the geometry of the body remains unchanged during deformations also in the description of the gravitational potential, which is treated by means of an Eulerian formalism. The geometry of the domain, where the momentum equation (1.3) is solved, is fixed implicitly since a Lagrangian formalism is employed here.

1.2 Spherical harmonic decomposition

We consider spherically symmetric models in this chapter. In order to employ the spherical symmetry, we use a formalism of spherical harmonic functions for individual quantities. Let $(\boldsymbol{e}_r,\boldsymbol{e}_\vartheta,\boldsymbol{e}_\phi)$ be the unit spherical vector basis with the radius r, the colatitude $\vartheta\in\langle 0,\pi\rangle$ and the longitude $\phi\in\langle 0,2\pi\rangle$. On the unit sphere a quadratically integrable scalar function $f(r,\vartheta,\phi)$ can be decomposed by means of the complete orthonormal basis of scalar spherical harmonic functions $Y_{lm}(\vartheta,\phi)$,

$$f(r,\vartheta,\phi)=\sum_{l=0}^{\infty}\sum_{m=-l}^{l} f_{lm}(r)Y_{lm}(\vartheta,\phi), \tag{1.15}$$

where l is the angular degree, m the azimuthal order and $f_{lm}(r)$ are coefficients of the expansion. The scalar spherical harmonic functions are defined by the relation

$$Y_{lm}(\vartheta,\phi) = (-1)^m N_{lm} P_l^m(\cos\vartheta)\mathrm{e}^{(im\phi)}, \tag{1.16}$$

where N_{lm} are the norm factors according to Martinec (1984),

$$N_{lm} = \sqrt{\frac{(2l+1)(l-m)!}{4\pi(l+m)!}} \tag{1.17}$$

and $P_l^m(\cos\vartheta)$ are the associated Legendre functions. Such a decomposition can be applied directly to the scalar incremental gravitational potential $\varphi(\boldsymbol{r})$. Similarly, we can decompose the displacement vector to express the remaining unknowns,

$$\begin{aligned}
\boldsymbol{u}(\boldsymbol{r}) &= u_r(\boldsymbol{r})\boldsymbol{e}_r + u_\vartheta(\boldsymbol{r})\boldsymbol{e}_\vartheta + u_\phi(\boldsymbol{r})\boldsymbol{e}_\phi, && (1.18)\\
u_r(\boldsymbol{r}) &= \sum_{lm} U_{lm}(r) Y_{lm}(\vartheta,\phi), && (1.19)\\
u_\vartheta(\boldsymbol{r}) &= \sum_{lm} V_{lm}(r)\frac{\partial Y_{lm}}{\partial\vartheta}(\vartheta,\phi) - W_{lm}(r)\frac{1}{\sin\vartheta}\frac{\partial Y_{lm}}{\partial\phi}(\vartheta,\phi), && (1.20)\\
u_\phi(\boldsymbol{r}) &= \sum_{lm} V_{lm}(r)\frac{1}{\sin\vartheta}\frac{\partial Y_{lm}}{\partial\phi}(\vartheta,\phi) + W_{lm}(r)\frac{\partial Y_{lm}}{\partial\vartheta}(\vartheta,\phi), && (1.21)\\
\varphi(\boldsymbol{r}) &= \sum_{lm} F_{lm}(r) Y_{lm}(\vartheta,\phi). && (1.22)
\end{aligned}$$

This formalism agrees also with Hanyk (1999) and Hanyk et al. (2002), where the problem of postglacial rebound is studied. We introduce the vector spherical harmonic functions $\boldsymbol{S}_{lm}^{(-1)}$, $\boldsymbol{S}_{lm}^{(1)} \equiv \nabla_\Omega Y_{lm}$ and $\boldsymbol{S}_{lm}^{(0)} \equiv \boldsymbol{e}_r \times \nabla_\Omega Y_{lm}$,

$$\begin{aligned}
\boldsymbol{S}_{lm}^{(-1)}(\vartheta,\phi) &= Y_{lm}\boldsymbol{e}_r, && (1.23)\\
\boldsymbol{S}_{lm}^{(1)}(\vartheta,\phi) &= \frac{\partial Y_{lm}}{\partial\vartheta}\boldsymbol{e}_\vartheta + \frac{1}{\sin\vartheta}\frac{\partial Y_{lm}}{\partial\phi}\boldsymbol{e}_\phi, && (1.24)\\
\boldsymbol{S}_{lm}^{(0)}(\vartheta,\phi) &= -\frac{1}{\sin\vartheta}\frac{\partial Y_{lm}}{\partial\phi}\boldsymbol{e}_\vartheta + \frac{\partial Y_{lm}}{\partial\vartheta}\boldsymbol{e}_\phi. && (1.25)
\end{aligned}$$

Functions $\boldsymbol{S}_{lm}^{(0)}$ create the toroidal basis and $\boldsymbol{S}_{lm}^{(-1)}$, $\boldsymbol{S}_{lm}^{(1)}$ form the spheroidal basis. The displacement vector $\boldsymbol{u}$ and traction $\boldsymbol{T}_r$ can be written in the form

$$\begin{aligned}
\boldsymbol{u}(\boldsymbol{r}) &= \sum_{lm}\left[U_{lm}(r)\boldsymbol{S}_{lm}^{(-1)} + V_{lm}(r)\boldsymbol{S}_{lm}^{(1)} + W_{lm}(r)\boldsymbol{S}_{lm}^{(0)}\right], && (1.26)\\
\boldsymbol{e}_r\cdot\boldsymbol{\tau} \equiv \boldsymbol{T}_r &= \sum_{lm}\left[T_{rr,lm}(r)\boldsymbol{S}_{lm}^{(-1)} + T_{r\vartheta,lm}(r)\boldsymbol{S}_{lm}^{(1)} + T_{r\phi,lm}(r)\boldsymbol{S}_{lm}^{(0)}\right]. && (1.27)
\end{aligned}$$

Let us denote the derivative in the direction of the radial coordinate $f' \equiv \mathrm{d}f/\mathrm{d}r$. After the substitution of (1.5), (1.22) and (1.26) into the momentum equation (1.3) we obtain

$$\begin{aligned}
\nabla\cdot\boldsymbol{\tau} = \sum_{lm}\Bigg[&\left(T'_{rr,lm} - \frac{4\gamma}{r^2}U_{lm} + \frac{2N\gamma}{r^2}V_{lm} + \frac{4\mu}{r\beta}T_{rr,lm} - \frac{N}{r}T_{r\vartheta,lm}\right)\boldsymbol{S}_{lm}^{(-1)}\\
&+\left(T'_{r\vartheta,lm} + \frac{2\gamma}{r^2}U_{lm} - \frac{N\gamma+(N-2)\mu}{r^2}V_{lm} + \frac{\lambda}{r\beta}T_{rr,lm} + \frac{3}{r}T_{r\vartheta,lm}\right)\boldsymbol{S}_{lm}^{(1)}\\
&+\left(T'_{r\phi,lm} - \frac{(N-2)\mu}{r^2}W_{lm} + \frac{3}{r}T_{r\phi,lm}\right)\boldsymbol{S}_{lm}^{(0)}\Bigg], \qquad (1.28)
\end{aligned}$$

$$\boldsymbol{f} = \sum_{lm}\left[\left(\frac{4\rho_0 g_0}{r}U_{lm} - \frac{N\rho_0 g_0}{r}V_{lm} + \frac{(n+1)\rho_0}{r}F_{lm} - \rho_0 Q_{lm}\right)\boldsymbol{S}_{lm}^{(-1)} - \left(\frac{\rho_0 g_0}{r}U_{lm} + \frac{\rho_0}{r}F_{lm}\right)\boldsymbol{S}_{lm}^{(1)}\right], \tag{1.29}$$

where $\boldsymbol{f} = -\rho_0\nabla\varphi + \nabla\cdot(\rho_0\boldsymbol{u})\nabla\varphi_0 - \nabla(\rho_0\nabla\varphi_0\cdot\boldsymbol{u})$, $\beta = \lambda + 2\mu$, $\gamma = \mu(3\lambda+2\mu)/\beta$, $N = l(l+1)$, $\nabla\varphi_0 = g_0\boldsymbol{e}_r$ (with $g_0 > 0$) and the components of the traction $T_{rr,lm}$, $T_{r\vartheta,lm}$ a $T_{r\phi,lm}$ and the auxiliary coefficients Q_{lm} are given by

$$T_{rr,lm} = \beta U'_{lm} + \frac{\lambda}{r}\left(2U_{lm} - NV_{lm}\right), \tag{1.30}$$

$$T_{r\vartheta,lm} = \mu\left(V'_{lm} + \frac{U_{lm} - V_{lm}}{r}\right), \tag{1.31}$$

$$T_{r\phi,lm} = \mu\left(W'_{lm} - \frac{W_{lm}}{r}\right), \tag{1.32}$$

$$Q_{lm} = F'_{lm} + \frac{l+1}{r}F_{lm} + 4\pi G\rho_0 U_{lm}. \tag{1.33}$$

By substituting (1.22) and (1.26) into the Poisson equation (1.4) we obtain

$$\nabla\cdot(\nabla\varphi + 4\pi G\rho_0\boldsymbol{u}) = \sum_{lm}\left[Q'_{lm} + 4\pi G\frac{(l+1)\rho_0}{r}U_{lm} - 4\pi G\frac{N\rho_0}{r}V_{lm} - \frac{l-1}{r}Q_{lm}\right]Y_{lm}. \tag{1.34}$$

We transform (1.3) into the Fourier spectral domain. In other words, we formally replace $\frac{\partial}{\partial t}$ by $i\omega$ and $\frac{\partial^2}{\partial t^2}$ by $-\omega^2$, where ω is the angular frequency of an individual free oscillation or tidal wave, to obtain $-\rho_0\omega^2\boldsymbol{u}$ on the right-hand side of (1.3). The azimuthal order m does not play a role in the case of a spherical symmetric model due to the $2l+1$ degeneracy.

1.3 Ordinary differential equations

1.3.1 Toroidal oscillations

Toroidal free oscillations create neither volume variations (the radial component of the displacement is equal to zero), nor changes of the gravitational field, i.e.,

$$\nabla\cdot\boldsymbol{u} = 0, \quad \boldsymbol{u}\cdot\boldsymbol{e}_r = 0 \ \text{ and } \ \varphi = 0. \tag{1.35}$$

The toroidal displacement vector formulated by means of the vector spherical harmonic functions is expressed in terms of the functions $W \equiv W_{lm}$ in (1.26) and the equation (1.3) assumes the form of an ordinary differential equation of the second order (cf. Martinec, 1984 (4.37); Dahlen, 1998 (8.45)):

$$\mu W'' + \left(\frac{2\mu}{r} + \mu'\right)W' - \left(\frac{N\mu}{r} + \mu'\right)\frac{W}{r} = -\rho_0\omega^2 W. \tag{1.36}$$

The inner boundary conditions, requiring the continuity of the displacement and the incremental traction, attain the form,

$$\begin{aligned}[W]^+_- &= 0,\\ [T_{r\phi}]^+_- \equiv \left[\mu\left(W' - \frac{W}{r}\right)\right]^+_- &= 0,\end{aligned} \tag{1.37}$$

for the case of solid boundaries. Toroidal oscillations do not exist in liquid layers, hence the same equation holds on liquid boundaries and at the free surface,

$$T_{r\phi} \equiv \mu \left(W' - \frac{W}{r} \right) = 0. \tag{1.38}$$

If the model does not contain a liquid layer, toroidal displacements exist in the entire volume and vanish at the center of the model for all modes with $l \geq 1$ (see Appendix). We adopted the normalization of the free-oscillation eigenfunctions from Dahlen and Tromp (1998) where the kinetic energy $\mathcal{T}$ is equal to one,

$$\mathcal{T} = N \int_0^R \rho_0 W^2 r^2 dr = 1, \tag{1.39}$$

and R denotes the radius of the model.

1.3.2 Spheroidal oscillations

The spheroidal part of the displacement vector satisfies the equation,

$$(\nabla \times \boldsymbol{u}) \cdot \boldsymbol{e}_r = 0. \tag{1.40}$$

Spheroidal oscillations cause volume variations; as a consequence the incremental gravitational potential φ is non-zero. Equations (1.3)–(1.5) rewritten with the terms of (1.22) and (1.26) yield a set of three ordinary differential equations of the second order for the unknowns $U \equiv U_{lm}$, $V \equiv V_{lm}$ and $F \equiv F_{lm}$ (cf. Martinec, 1984 (4.54)–(4.56); Dahlen, 1998 (8.43)–(8.44), (8.53)),

$$\begin{aligned} \beta U'' + \left(\frac{2\beta}{r} + \beta' \right) U' + \left(\frac{4\rho_0 g_0}{r} - 4\pi G \rho_0^2 - \frac{2\beta + \mu N}{r^2} + \frac{2\lambda'}{r} \right) U - & \qquad (1.41) \\ - (\lambda + \mu) \frac{NV'}{r} + \left(\frac{\lambda + 3\mu}{r} - \rho_0 g_0 - \lambda' \right) \frac{NV}{r} - \rho_0 F' &= -\rho_0 \omega^2 U, \\ \mu V'' + \left(\frac{2\mu}{r} + \mu' \right) V' - \left(\frac{\beta}{r} + \mu' \right) \frac{N}{r} V + & \qquad (1.42) \\ + \frac{\lambda + \mu}{r} U' + \left(\frac{2\beta}{r} - \rho_0 g_0 + \mu' \right) \frac{U}{r} - \frac{\rho_0}{r} F &= -\rho_0 \omega^2 V, \\ F'' + \frac{2}{r} F' - \frac{N}{r^2} F + 4\pi G \rho_0 \left[U' + \left(\frac{2}{r} + \frac{\rho_0'}{\rho_0} \right) U - \frac{N}{r} V \right] &= 0. \qquad (1.43) \end{aligned}$$

The conditions on the inner boundaries and free surface for the displacement, incremental traction and incremental potential take the form

$$\begin{aligned} \text{solid boundary} \qquad & [U]_-^+ = 0, \\ & [V]_-^+ = 0, \\ & [T_{rr}]_-^+ \equiv \left[\beta U' + \frac{\lambda}{r} (2U - NV) \right]_-^+ = 0, \\ & [T_{r\vartheta}]_-^+ \equiv \left[\mu \left(V' - \frac{V}{r} + \frac{U}{r} \right) \right]_-^+ = 0, \\ & [F]_-^+ = 0, \end{aligned}$$

$$[F' + 4\pi G\rho_0 U]^+_- = 0, \tag{1.44}$$

liquid boundary

$$[U]^+_- = 0,$$

$$[T_{rr}]^+_- \equiv \left[\beta U' + \frac{\lambda}{r}(2U - NV)\right]^+_- = 0,$$

$$T_{r\vartheta} \equiv \mu\left(V' - \frac{V}{r} + \frac{U}{r}\right) = 0,$$

$$[F]^+_- = 0,$$

$$[F' + 4\pi G\rho_0 U]^+_- = 0, \tag{1.45}$$

free surface

$$T_{rr} \equiv \beta U' + \frac{\lambda}{r}(2U - NV) = 0,$$

$$T_{r\vartheta} \equiv \mu\left(V' - \frac{V}{r} + \frac{U}{r}\right) = 0,$$

$$Q \equiv F' + \frac{l+1}{r}F + 4\pi G\rho_0 U = 0. \tag{1.46}$$

The boundary conditions at the center of the model are (see Appendix),

$$U(0) = V(0) = 0, \quad F(0) = 0 \quad \text{for} \quad l > 1, \tag{1.47}$$

and

$$U'(0) = V'(0) = 0, \quad F(0) = 0 \quad \text{for} \quad l = 1. \tag{1.48}$$

We again adopted the normalization from Dahlen and Tromp (1998) where the kinetic energy $\mathcal{T}$ is equal to one,

$$\mathcal{T} = \int_0^R \rho_0(U^2 + NV^2)r^2 dr = 1, \tag{1.49}$$

and R denotes the radius of the model.

1.3.3 Radial oscillations

If the angular degree of the spheroidal modes equals zero, $l = 0$, the motion proceeds only in the radial direction and the horizontal displacement vanishes. $F \equiv F_{00}$ satisfies (1.43), that arrives at a special form,

$$F'' + \frac{2}{r}F' + 4\pi G\rho_0\left[U' + \left(\frac{2}{r} + \frac{\rho_0'}{\rho_0}\right)U\right] = \\ = \frac{1}{r^2}\left(r^2F'\right)' + \frac{4\pi G}{r^2}\left(r^2\rho_0 U\right)' = 0 \tag{1.50}$$

and because the integration constant is clearly zero (Martinec, 1984),

$$F' + 4\pi G\rho_0 U = 0. \tag{1.51}$$

By substitution of (1.51) into (1.41) we obtain the ordinary differential equation of the second order for the unknown $U \equiv U_{00}$,

$$\beta U'' + \left(\frac{2\beta}{r} + \beta'\right)U' + \left(4\rho_0 g_0 - \frac{2\beta}{r} + 2\lambda'\right)\frac{U}{r} = -\rho_0\omega^2 U. \tag{1.52}$$

Since the horizontal components of the displacement vector are zero, both the solid and liquid boundaries behave in the same way. The normal components of the displacement and traction have the form,

$$\text{all internal boundaries} \qquad [U]^+_- = 0,$$

$$[T_{rr}]^+_- \equiv \left[\beta U' + \frac{2\lambda}{r}U\right]^+_- = 0, \tag{1.53}$$

$$\text{free surface} \qquad T_{rr} \equiv \beta U' + \frac{2\lambda}{r}U = 0, \tag{1.54}$$

$$\text{the center (see Appendix)} \qquad U(0) = 0. \tag{1.55}$$

In contrast to spheroidal oscillations with $l > 0$, computation of displacement is not coupled to computation of the incremental gravitational potential.

1.4 Elastic tides

The tidal deformation is caused by an external gravitational force. The incremental gravitational potential φ can be expressed as a sum of the gravitational potential φ_d caused by the deformation and the tidal potential φ_t,

$$\varphi = \varphi_d + \varphi_t = \sum_{l=0}^{\infty}(F_l^d + F_l^t)Y_l\,, \tag{1.56}$$

where F_l^d and F_l^t are the coefficients of expansions and Y_l is abbreviation for any Y_{lm}. The boundary condition (1.14) between the internal and external incremental gravitational potential at the surface ($r = R$) reduces to

$$\left[\frac{\partial\varphi}{\partial r}\right]^+_- = 4\pi G\rho_0 u. \tag{1.57}$$

Outside the body, the coefficients F_l^d are proportional to $1/r^{l+1}$ (Jekeli, 1989) and F_l^t are proportional to r^l (Agnew, 2007). The right-hand side of (1.56) can thus be decomposed as follows,

$$F_l^{d\prime} + F_l^{t\prime} = -\frac{l+1}{r}F_l^d + \frac{l}{r}F_l^t = -\frac{l+1}{r}F_l + \frac{2l+1}{r}F_l^t\,, \tag{1.58}$$

that forms together with the left-hand side $F_l' + 4\pi G\rho_0 U$ the condition on the surface,

$$Q_l = F_l' + \frac{l+1}{r}F_l + 4\pi G\rho_0 U_l = \frac{2l+1}{R}F_l^t\,. \tag{1.59}$$

As usual (e.g., Wahr 1989), the l^{th}-degree contribution to $\boldsymbol{u}$ and φ on the surface can be related to the l^{th}-degree contribution $\varphi_{t,l} = F_l^t\,Y_l$ of the tidal potential φ^t by the definitions

$$u_{r,l}(\vartheta,\phi) = -\frac{h_l}{g_0}\varphi_{t,l}(\vartheta,\phi), \tag{1.60}$$

$$u_{\vartheta,l}(\vartheta,\phi) = -\frac{l_l}{g_0}\frac{\partial\varphi_{t,l}(\vartheta,\phi)}{\partial\vartheta}, \tag{1.61}$$

$$u_{\phi,l}(\vartheta,\phi) = -\frac{l_l}{g_0\sin\vartheta}\frac{\partial\varphi_{t,l}(\vartheta,\phi)}{\partial\phi}, \tag{1.62}$$

$$\varphi_l = \varphi_{d,l}(\vartheta,\phi) + \varphi_{t,l}(\vartheta,\phi) = (k_l+1)\varphi_{t,l}(\vartheta,\phi), \tag{1.63}$$

where g_0 is the surface acceleration. The dimensionless numbers h_l, l_l and k_l are called the tidal Love numbers. The tidal displacement vector is spheroidal, thus the differential equations (1.41)–(1.43) and the boundary conditions (1.44)–(1.46) are the same as for the spheroidal oscillations with the exception of the last relation in (1.46) which must be replaced by (1.59); ω_l is now the tidal frequency, which is the same for all l, i.e. we set $\omega_l = \omega$. For $\omega = 0$ we obtain static tides.

Carrying out the spherical decomposition of (1.60)–(1.63), we arrive at the simple expressions

$$h_l = \frac{U_l}{R}\left(-\frac{Rg_0}{F_l^t}\right), \tag{1.64}$$

$$l_l = \frac{V_l}{R}\left(-\frac{Rg_0}{F_l^t}\right), \tag{1.65}$$

$$1 + k_l = -\frac{F_l}{Rg_0}\left(-\frac{Rg_0}{F_l^t}\right). \tag{1.66}$$

The dimensionless factor $-Rg_0/F_l^t$ can be used as a normalization constant for U_l, V_l and F_l. The last boundary condition of (1.46), multiplied by this factor, can be rewritten for the normalized unknowns into the final form,

$$\bar{F}_l' + \frac{l+1}{r}\bar{F}_l + 4\pi G\rho_0\bar{U}_l = -(2l+1)g_0, \tag{1.67}$$

that we use in numerical calculations of tides. We employ the normalized unknowns $\bar{U}_l = -U_l Rg_0/F_l^t$ and $\bar{V}_l = -V_l Rg_0/F_l^t$. Relations (1.64)–(1.66) and boundary condition (1.67) are in accord with Fang (1998), where this normalization was implicitly made.

1.5 Matrix representation

Our goal is to derive a matrix eigenvalue problem for the free oscillations and a set of algebraic equations for the tides. First, we arrange the unknowns $U \equiv U_{lm}(r)$, $V \equiv V_{lm}(r)$, $F \equiv F_{lm}(r)$ and $W \equiv W_{lm}(r)$ into the vector

$$\boldsymbol{y}(r) = (U, V, F, W)^{\mathrm{T}}. \tag{1.68}$$

Then the equations (1.36), (1.41)–(1.43) can be rewritten into the matrix form,

$$\mathbf{A}(r)\cdot\boldsymbol{y}'' + \mathbf{B}(r)\cdot\boldsymbol{y}' + \mathbf{C}(r)\cdot\boldsymbol{y} = -\omega^2\mathbf{D}(r)\cdot\boldsymbol{y}, \tag{1.69}$$

where the coefficient matrices **A**–**D** are

$$\mathbf{A}(r) = \begin{pmatrix} \beta & 0 & 0 & 0 \\ 0 & \mu & 0 & 0 \\ 0 & 0 & 1 & 0 \\ 0 & 0 & 0 & \mu \end{pmatrix}, \tag{1.70}$$

$$\mathbf{B}(r) = \begin{pmatrix} \frac{2\beta}{r} + \beta' & -\frac{(\lambda+\mu)N}{r} & -\rho_0 & 0 \\ \frac{\lambda+\mu}{r} & \frac{2\mu}{r} + \mu' & 0 & 0 \\ 4\pi G\rho_0 & 0 & \frac{2}{r} & 0 \\ 0 & 0 & 0 & \frac{2\mu}{r} + \mu' \end{pmatrix}, \tag{1.71}$$

$$\mathbf{C}(r) = \begin{pmatrix} \frac{4\rho_0 g_0}{r} - 4\pi G\rho_0^2 - \frac{2\beta+\mu N}{r^2} + \frac{2\lambda'}{r} & \left(\frac{\lambda+3\mu}{r} - \rho_0 g_0 - \lambda'\right)\frac{NV}{r} & 0 & 0 \\ \frac{2\beta}{r^2} - \frac{\rho_0 g_0}{r} + \frac{\mu'}{r} & -\left(\frac{\beta}{r} + \mu'\right)\frac{N}{r} & -\frac{\rho_0}{r} & 0 \\ 4\pi G(\frac{2\rho_0}{r} + \rho') & -4\pi G\rho_0 \frac{N}{r} & -\frac{N}{r^2} & 0 \\ 0 & 0 & 0 & -\left(\frac{N\mu}{r} + \mu'\right)\frac{1}{r} \end{pmatrix}, \quad (1.72)$$

$$\mathbf{D}(r) = \begin{pmatrix} \rho_0 & 0 & 0 & 0 \\ 0 & \rho_0 & 0 & 0 \\ 0 & 0 & 0 & 0 \\ 0 & 0 & 0 & \rho_0 \end{pmatrix}. \quad (1.73)$$

In order to discretize (1.68)–(1.69) with a pseudospectral accuracy, we follow the high-order pseudospectral approach described by, e.g., Fornberg (1996). The discretization grid comes out from the local extrema of the Chebyshev polynomials

$$T_{M-1}(x) = \cos[(M-1)\arccos x] \quad (1.74)$$

on the interval $\langle -1, 1\rangle$,

$$x_i = \cos\left(\frac{\pi(i-1)}{M-1}\right), \quad i = 1, \ldots, M. \quad (1.75)$$

The Chebyshev grid $r_{min} = r_1 < \ldots < r_M = r_{max}$ thus consists of the points

$$r_{M-i+1} = r_{min} + \frac{r_{max} - r_{min}}{2}\left[\cos\left(\frac{\pi(i-1)}{M-1}\right) + 1\right], \quad i = 1, \ldots, M. \quad (1.76)$$

The values of $\boldsymbol{y}$ and its derivatives at r_i can be expressed using the weighted sum of values $\boldsymbol{y}$ on the whole grid,

$$\boldsymbol{y}(r_i) = \sum_{j=1}^{M} \alpha_{ij}\boldsymbol{y}(r_j), \quad (1.77)$$

$$\boldsymbol{y}'(r_i) = \sum_{j=1}^{M} \beta_{ij}\boldsymbol{y}(r_j), \quad (1.78)$$

$$\boldsymbol{y}''(r_i) = \sum_{j=1}^{M} \gamma_{ij}\boldsymbol{y}(r_j). \quad (1.79)$$

The elements of weight matrices α_{ij}, β_{ij} and γ_{ij} can be evaluated by means of the algorithm developed by Fornberg (1996). Note that here, where both r_i and r_j are the grid points, the α_{ij} elements are simply: $\alpha_{ii} = 1$ and $\alpha_{ij} = 0$ for $i \neq j$. With the weight matrices the equation (1.69) can be expressed in the form,

$$\begin{aligned} \sum_{j=1}^{M} [\mathbf{A}(r_i)\gamma_{ij} + \mathbf{B}(r_i)\beta_{ij} + \mathbf{C}(r_i)\alpha_{ij}] \cdot \boldsymbol{y}(r_j) &= -\omega^2 \sum_{j=1}^{M} \mathbf{D}(r_i)\alpha_{ij} \cdot \boldsymbol{y}(r_j), \quad (1.80) \\ i &= 2, \ldots, M-1. \end{aligned}$$

It is necessary to explain the meaning of the product, e.g., $\mathbf{A}\gamma_{ij}$ in (1.80). The size of the matrix $\mathbf{A}$ is 4×4, whereas γ_{ij} are elements of a matrix of the size $M \times M$. By multiplying each element of the matrix $\mathbf{A}$ by γ_{ij} we obtain a $(4M-8) \times 4M$ matrix. The equation (1.80) is solved in the internal grid points. The boundary conditions have to be satisfied at the boundary points, r_1 and r_M, as follows.

As is summarized in Appendix, the boundary conditions in the center of the model, $r_{min} = 0$, satisfy

$$\begin{aligned} l > 1: &\quad (U, V, F, W)^{\mathrm{T}}(0) = \mathbf{0}, \\ l = 1: &\quad (U', V', F, W)^{\mathrm{T}}(0) = \mathbf{0}, \end{aligned} \tag{1.81}$$

and in the matrix form

$$\mathbf{F}^{\beta} \cdot \boldsymbol{y}' + \mathbf{F}^{\alpha} \cdot \boldsymbol{y} = \mathbf{0}, \tag{1.82}$$

where

$$l > 1: \quad \mathbf{F}^{\alpha} = \begin{pmatrix} 1 & 0 & 0 & 0 \\ 0 & 1 & 0 & 0 \\ 0 & 0 & 1 & 0 \\ 0 & 0 & 0 & 1 \end{pmatrix}, \quad \mathbf{F}^{\beta} = \begin{pmatrix} 0 & 0 & 0 & 0 \\ 0 & 0 & 0 & 0 \\ 0 & 0 & 0 & 0 \\ 0 & 0 & 0 & 0 \end{pmatrix}, \tag{1.83}$$

$$l = 1: \quad \mathbf{F}^{\alpha} = \begin{pmatrix} 0 & 0 & 0 & 0 \\ 0 & 0 & 0 & 0 \\ 0 & 0 & 1 & 0 \\ 0 & 0 & 0 & 1 \end{pmatrix}, \quad \mathbf{F}^{\beta} = \begin{pmatrix} 1 & 0 & 0 & 0 \\ 0 & 1 & 0 & 0 \\ 0 & 0 & 0 & 0 \\ 0 & 0 & 0 & 0 \end{pmatrix}. \tag{1.84}$$

With the weight matrices the boundary conditions (1.81) are

$$\sum_{j=1}^{M} [\mathbf{F}^{\beta} \beta_{0j} + \mathbf{F}^{\alpha} \alpha_{0j}] \cdot \boldsymbol{y}(r_j) = \mathbf{0}. \tag{1.85}$$

The free-surface boundary conditions (1.38) and (1.46) have the matrix form

$$(T_{rr}, T_{r\vartheta}, Q, T_{r\varphi})^{\mathrm{T}} = \mathbf{A} \cdot \boldsymbol{y}' + \mathbf{E} \cdot \boldsymbol{y} = \mathbf{0}, \tag{1.86}$$

where the coefficient matrix $\mathbf{E}$ is

$$\mathbf{E}(r) = \begin{pmatrix} \frac{2\lambda}{r} & -\frac{N\lambda}{r} & 0 & 0 \\ \frac{\mu}{r} & -\frac{\mu}{r} & 0 & 0 \\ 4\pi G\rho_0 & 0 & \frac{l+1}{r} & 0 \\ 0 & 0 & 0 & -\frac{\mu}{r} \end{pmatrix}, \quad r = r_M, \tag{1.87}$$

and with the weight matrices it can be rewritten as

$$\sum_{j=1}^{M} [\mathbf{A}(r_M) \beta_{Mj} + \mathbf{E}(r_M) \alpha_{Mj}] \cdot \boldsymbol{y}(r_j) = \mathbf{0}. \tag{1.88}$$

In the case of tides, the vector $\boldsymbol{q} = (0, 0, -(2l+1)g_0, 0)^{\mathrm{T}}$ appears on the right-hand side of (1.67); we will discuss this case separately.

For a one-layer model, the whole problem is described by the equations (1.85), (1.80) and (1.88) in the form of a generalized eigenvalue problem,

$$\mathbf{P} \cdot \boldsymbol{Y} = -\omega^2 \mathbf{R} \cdot \boldsymbol{Y}, \tag{1.89}$$

where the vector $\boldsymbol{Y} = (U_1 \dots U_M, V_1 \dots V_M, F_1 \dots F_M, W_1 \dots W_M)^{\mathrm{T}}$ has the size $4M$ and the matrices $\mathbf{P}$ and $\mathbf{R}$ are $4M \times 4M$,

$$\mathbf{P} = \begin{pmatrix} \mathbf{F}^{\beta} \beta_{0j} + \mathbf{F}^{\alpha} \alpha_{0j} \\ \\ \mathbf{A} \gamma_{ij} + \mathbf{B} \beta_{ij} + \mathbf{C} \alpha_{ij} \\ \\ \mathbf{A} \beta_{Mj} + \mathbf{E} \alpha_{Mj} \end{pmatrix}, \quad \mathbf{R} = \begin{pmatrix} 0 \\ \\ \mathbf{D} \alpha_{ij} \\ \\ 0 \end{pmatrix}, \tag{1.90}$$

where $i = 2, \ldots, M-1$ and $j = 1, \ldots, M$.

The extension to K layers is quite simple. We start with the models composed of solid layers only, models with liquid layers will be discussed later. We mark vector $\boldsymbol{Y}$ as $\boldsymbol{Y}^{(k)}$ in the k^{th} layer, $k = 1, \ldots, K$. On the solid boundary the continuity conditions for the displacement, the gravitational potential, the traction and Q are described by (1.37) and (1.44). Using the expansions (1.77) and (1.78) we get

$$\sum_{j=1}^{M^{(k)}} \mathbf{I}\alpha^{(k)}_{M^{(k)}j}\boldsymbol{Y}^{(k)}(r^{(k)}_j) - \sum_{j=1}^{M^{(k+1)}} \mathbf{I}\alpha^{(k+1)}_{1j}\boldsymbol{Y}^{(k+1)}(r^{(k+1)}_j) = \mathbf{0} \tag{1.91}$$

and, for brevity with layer superscripts denoting only the unknown vectors,

$$\sum_{j=1}^{M} \left[\mathbf{A}\beta_{Mj} + \hat{\mathbf{E}}\alpha_{Mj}\right] \boldsymbol{Y}^{(k)}(r_j) - \sum_{j=1}^{M} \left[\mathbf{A}\beta_{1j} + \hat{\mathbf{E}}\alpha_{1j}\right] \boldsymbol{Y}^{(k+1)}(r_j) = \mathbf{0}, \tag{1.92}$$

where $\mathbf{I}$ is the 4×4 identity matrix. The components of the coefficient matrix $\hat{\mathbf{E}}$,

$$\hat{\mathbf{E}}(r) = \begin{pmatrix} \frac{2\lambda}{r} & -\frac{N\lambda}{r} & 0 & 0 \\ \frac{\mu}{r} & -\frac{\mu}{r} & 0 & 0 \\ 4\pi G\rho_0 & 0 & 0 & 0 \\ 0 & 0 & 0 & -\frac{\mu}{r} \end{pmatrix}, \tag{1.93}$$

come out from the boundary conditions (1.44) and (1.37). In fact, because of continuity of F in (1.44), we can use $\mathbf{E}(r)$ instead of $\hat{\mathbf{E}}(r)$.

We introduce the vector $\tilde{\boldsymbol{Y}}$ composed from the unknowns $\boldsymbol{Y}^{(k)}$ in all layers,

$$\tilde{\boldsymbol{Y}} = \left(\boldsymbol{Y}^{(1)}, \ldots, \boldsymbol{Y}^{(k)}, \ldots, \boldsymbol{Y}^{(K)}\right)^{\mathrm{T}}. \tag{1.94}$$

The total number of grid points, and the size of $\tilde{\boldsymbol{Y}}$, is $\tilde{M} = \sum_{k=1}^{K} M^{(k)}$. The matrix equation (1.89) generalized for K layers takes the form

$$\tilde{\mathbf{P}} \cdot \tilde{\boldsymbol{Y}} = -\omega^2 \tilde{\mathbf{R}} \cdot \tilde{\boldsymbol{Y}}. \tag{1.95}$$

The matrices $\tilde{\mathbf{P}}$ and $\tilde{\mathbf{R}}$ have the size $4\tilde{M} \times 4\tilde{M}$ and are given explicitly in the next sections. As the matrix $\tilde{\mathbf{P}}$ is regular and can be inverted, we arrive at the form of the standard eigenvalue problem,

$$\left(\tilde{\mathbf{P}}^{-1} \cdot \tilde{\mathbf{R}}\right) \cdot \tilde{\boldsymbol{Y}} = -\frac{1}{\omega^2}\tilde{\boldsymbol{Y}}. \tag{1.96}$$

The equations for toroidal and spheroidal motions are independent and we decouple the both parts in what follows.

1.5.1 Toroidal oscillations

The unknown subvector $\boldsymbol{y}$ for toroidal modes contains only one toroidal component of the displacement, $\boldsymbol{y} = (W)^{\mathrm{T}}$. Also, the submatrices $\mathbf{A}_{\mathrm{T}}$–$\mathbf{F}_{\mathrm{T}}$ have one element each, corresponding to the 4^{th} row and the 4^{th} column of the matrices $\mathbf{A}$–$\mathbf{F}$. If the model contains liquid layers, where the toroidal oscillations do not exist, $r^{(1)}_{min}$ is the radius of the first liquid boundary from the surface towards the center and the free-surface condition (1.88) applies also on this boundary. If there is no liquid

layer, a condition at the center following from (1.85) is required instead. The $\tilde{M} \times \tilde{M}$ matrix $\tilde{\mathbf{P}}_{\mathrm{T}}$ for K layers and a model with liquid layers takes the form,

$$\tilde{\mathbf{P}}_{\mathrm{T}} = \begin{pmatrix} \mathbf{A}_{\mathrm{T}}\beta_{1j} + \mathbf{E}_{\mathrm{T}}\alpha_{1j} & & & & \\ \mathbf{A}_{\mathrm{T}}\gamma_{ij} + \mathbf{B}_{\mathrm{T}}\beta_{ij} + \mathbf{C}_{\mathrm{T}}\alpha_{ij} & & & & \\ \mathbf{A}_{\mathrm{T}}\beta_{Mj} + \mathbf{E}_{\mathrm{T}}\alpha_{Mj} & -\mathbf{A}_{\mathrm{T}}\beta_{1j} - \mathbf{E}_{\mathrm{T}}\alpha_{1j} & & & \\ \mathbf{I}\alpha_{Mj} & -\mathbf{I}\alpha_{1j} & \ddots & & \\ & & \ddots & & \\ & & & \mathbf{A}_{\mathrm{T}}\gamma_{ij} + \mathbf{B}_{\mathrm{T}}\beta_{ij} + \mathbf{C}_{\mathrm{T}}\alpha_{ij} & \\ & & & \mathbf{A}_{\mathrm{T}}\beta_{Mj} + \mathbf{E}_{\mathrm{T}}\alpha_{Mj} & \end{pmatrix},$$

where blocks with zero elements are left blank. The omitted layer superscript k increases along the diagonal. The matrix has a nearly block-diagonal structure and, moreover, can be inverted. Similarly, the $\tilde{M} \times \tilde{M}$ matrix $\tilde{\mathbf{R}}_{\mathrm{T}}$ is

$$\tilde{\mathbf{R}}_{\mathrm{T}} = \begin{pmatrix} \mathbf{0}_{1\mathrm{x}M} & & & & \\ \mathbf{D}_{\mathrm{T}}\alpha_{ij}{}_{(M-2)\mathrm{x}M} & & & & \\ \mathbf{0}_{1\mathrm{x}M} & \mathbf{0}_{1\mathrm{x}M} & & & \\ \mathbf{0}_{1\mathrm{x}M} & \mathbf{0}_{1\mathrm{x}M} & \ddots & & \\ & & \ddots & & \\ & & & \mathbf{D}_{\mathrm{T}}\alpha_{ij}{}_{(M-2)\mathrm{x}M} & \\ & & & \mathbf{0}_{1\mathrm{x}M} & \end{pmatrix}.$$

1.5.2 Spheroidal oscillations

The subvector $\boldsymbol{y}$ contains three unknown components, $\boldsymbol{y} = (U, V, F)^{\mathrm{T}}$. The 3×3 submatrices $\mathbf{A}_{\mathrm{S}}$–$\mathbf{F}_{\mathrm{S}}$ are the upper left blocks of the matrices $\mathbf{A}$–$\mathbf{F}$. Spheroidal oscillations do exist in liquid layers and the point of origin, $r^{(1)}_{min} = 0$, is always the center of the model, where conditions (1.85) have to be satisfied. The free-surface conditions (1.88) are required on the surface. The matrices $\tilde{\mathbf{P}}_{\mathrm{S}}$ and $\tilde{\mathbf{R}}_{\mathrm{S}}$ are created from (1.85), (1.80), (1.88), (1.91) and (1.92),

$$\tilde{\mathbf{P}}_{\mathrm{S}} = \begin{pmatrix} \mathbf{F}^{\beta}_{S}\beta_{0j} + \mathbf{F}^{\alpha}_{S}\alpha_{0j} & & & & \\ \mathbf{A}_{\mathrm{S}}\gamma_{ij} + \mathbf{B}_{\mathrm{S}}\beta_{ij} + \mathbf{C}_{\mathrm{S}}\alpha_{ij} & & & & \\ \mathbf{A}_{\mathrm{S}}\beta_{Mj} + \mathbf{E}_{\mathrm{S}}\alpha_{Mj} & -\mathbf{A}_{\mathrm{S}}\beta_{1j} - \mathbf{E}_{\mathrm{S}}\alpha_{1j} & & & \\ \mathbf{I}\alpha_{Mj} & -\mathbf{I}\alpha_{1j} & \ddots & & \\ & & \ddots & & \\ & & & \mathbf{A}_{\mathrm{S}}\gamma_{ij} + \mathbf{B}_{\mathrm{S}}\beta_{ij} + \mathbf{C}_{\mathrm{S}}\alpha_{ij} & \\ & & & \mathbf{A}_{\mathrm{S}}\beta_{Mj} + \mathbf{E}_{\mathrm{S}}\alpha_{Mj} & \end{pmatrix},$$

$$\tilde{\mathbf{R}}_{\mathrm{S}} = \begin{pmatrix} \boxed{\mathbf{0}}_{3\mathrm{x}3M} & & & \\ \boxed{\mathbf{D}_{\mathrm{S}}\alpha_{ij}}_{(3M-6)\mathrm{x}3M} & & & \\ \boxed{\mathbf{0}}_{3\mathrm{x}3M} & \boxed{\mathbf{0}}_{3\mathrm{x}3M} & & \\ \boxed{\mathbf{0}}_{3\mathrm{x}3M} & \boxed{\mathbf{0}}_{3\mathrm{x}3M} & \ddots & \\ & & \ddots & \boxed{\mathbf{D}_{\mathrm{S}}\alpha_{ij}}_{(3M-6)\mathrm{x}3M} \\ & & & \boxed{\mathbf{0}}_{3\mathrm{x}3M} \end{pmatrix}.$$

The size $3\tilde{M} \times 3\tilde{M}$ of the matrices $\tilde{\mathbf{P}}_{\mathrm{S}}$ and $\tilde{\mathbf{R}}_{\mathrm{S}}$ can be reduced by separation of the equations with zero right-hand sides in (1.95), i.e. those corresponding to the Poisson equation and the boundary conditions. Thus, (1.95) can be arranged into the form

$$\begin{pmatrix} \mathbf{P_1} & \mathbf{P_2} \\ \mathbf{P_3} & \mathbf{P_4} \end{pmatrix} \begin{pmatrix} \mathbf{Y_1} \\ \mathbf{Y_2} \end{pmatrix} = -\omega^2 \begin{pmatrix} \mathbf{R_1} & \mathbf{0} \\ \mathbf{0} & \mathbf{0} \end{pmatrix} \begin{pmatrix} \mathbf{Y_1} \\ \mathbf{Y_2} \end{pmatrix}. \tag{1.97}$$

$\mathbf{P_1}$, $\mathbf{P_2}$ and $\mathbf{R_1}$ correspond to the equations (1.41)–(1.42), whereas $\mathbf{P_3}$ and $\mathbf{P_4}$ match the equation (1.43) and boundary conditions (1.44)–(1.46). Vector $\mathbf{Y_1}$ is chosen to collect the displacement components in the internal points of the layers and vector $\mathbf{Y_2}$ consists of the components of the displacement in the boundary points and the incremental gravitational potential. Since

$$\mathbf{Y_2} = -\mathbf{P_4}^{-1}\mathbf{P_3}\mathbf{Y_1}, \tag{1.98}$$

the final eigenvalue problem with the matrix of the size $(2\tilde{M}-4K) \times (2\tilde{M}-4K)$ has the form

$$\left(\mathbf{P_1} - \mathbf{P_2}\mathbf{P_4}^{-1}\mathbf{P_3}\right)^{-1} \mathbf{R_1}\mathbf{Y_1} = -\frac{1}{\omega^2}\mathbf{Y_1}. \tag{1.99}$$

1.5.3 Radial oscillations

The subvector $\boldsymbol{y}$ contains only the radial component of the displacement, $\boldsymbol{y} = (U)$. The coefficient submatrices have one element each easily obtained from (1.52)–(1.55), i.e.,

$$\mathbf{A}_{\mathrm{R}} \;\rightarrow\; \beta, \tag{1.100}$$

$$\mathbf{B}_{\mathrm{R}} \;\rightarrow\; \frac{2\beta}{r} + \beta', \tag{1.101}$$

$$\mathbf{C}_{\mathrm{R}} \;\rightarrow\; \left(4\rho_0 g_0 - \frac{2\beta}{r} + 2\lambda'\right)\frac{1}{r}, \tag{1.102}$$

$$\mathbf{D}_{\mathrm{R}} \;\rightarrow\; \rho_0, \tag{1.103}$$

$$\mathbf{E}_{\mathrm{R}} \;\rightarrow\; \frac{2\lambda}{r}, \tag{1.104}$$

$$\mathbf{F}^{\alpha}_{\mathrm{R}} \;\rightarrow\; 1, \quad \mathbf{F}^{\beta}_{\mathrm{R}} \;\rightarrow\; 0. \tag{1.105}$$

The point of origin is the center of the model, $r^{(1)}_{min} = 0$, where $U(0) = 0$, and the free-surface condition (1.54) is required on the surface. The $\tilde{M} \times \tilde{M}$ matrices $\tilde{\mathbf{P}}_{\mathrm{R}}$

and $\tilde{\mathbf{R}}_{\mathrm{R}}$ take the forms

$$\tilde{\mathbf{P}}_{\mathrm{R}} = \begin{pmatrix} \boxed{\mathbf{F}_R^{\alpha}\alpha_{0j}} & & & \\ \boxed{\mathbf{A}_{\mathrm{R}}\gamma_{ij} + \mathbf{B}_{\mathrm{R}}\beta_{ij} + \mathbf{C}_{\mathrm{R}}\alpha_{ij}} & & & \\ \boxed{\mathbf{A}_{\mathrm{R}}\beta_{Mj} + \mathbf{E}_{\mathrm{R}}\alpha_{Mj}} & \boxed{-\mathbf{A}_{\mathrm{R}}\beta_{1j} - \mathbf{E}_{\mathrm{R}}\alpha_{1j}} & \ddots & \\ \boxed{\mathbf{I}\alpha_{Mj}} & \boxed{-\mathbf{I}\alpha_{1j}} & \ddots & \\ & & & \boxed{\mathbf{A}_{\mathrm{R}}\gamma_{ij} + \mathbf{B}_{\mathrm{R}}\beta_{ij} + \mathbf{C}_{\mathrm{R}}\alpha_{ij}} \\ & & & \boxed{\mathbf{A}_{\mathrm{R}}\beta_{Mj} + \mathbf{E}_{\mathrm{R}}\alpha_{Mj}} \end{pmatrix},$$

$$\tilde{\mathbf{R}}_{\mathrm{R}} = \begin{pmatrix} \boxed{\mathbf{0}}_{1\mathrm{x}M} & & & \\ \boxed{\mathbf{D}_{\mathrm{R}}\alpha_{ij}}_{(M-2)\mathrm{x}M} & & & \\ \boxed{\mathbf{0}}_{1\mathrm{x}M} & \boxed{\mathbf{0}}_{1\mathrm{x}M} & \ddots & \\ \boxed{\mathbf{0}}_{1\mathrm{x}M} & \boxed{\mathbf{0}}_{1\mathrm{x}M} & \ddots & \\ & & & \boxed{\mathbf{D}_{\mathrm{R}}\alpha_{ij}}_{(M-2)\mathrm{x}M} \\ & & & \boxed{\mathbf{0}}_{1\mathrm{x}M} \end{pmatrix}.$$

1.5.4 Tides

The vector of unknowns is the same as for the spheroidal modes, $\boldsymbol{y} = (U, V, F)^{\mathrm{T}}$, and the same equations and boundary conditions are valid in all grid points except for the surface where the tidal potential changes the right-hand side of the free-surface boundary condition (1.67). Since the coefficient matrices $\mathbf{A}_{\mathrm{S}}$–$\mathbf{F}_{\mathrm{S}}$ are the same as for the spheroidal modes, the matrix equation has the form

$$\left(\tilde{\mathbf{P}}_{\mathrm{S}} + \omega^2\tilde{\mathbf{R}}_{\mathrm{S}}\right) \cdot \tilde{\boldsymbol{Y}} = \tilde{\boldsymbol{Q}}_{tide} \tag{1.106}$$

where the last term of the vector $\tilde{\boldsymbol{Q}}_{tide} = [0, \ldots, 0, -(2l+1)g_0]^{\mathrm{T}}$ of the size $3\tilde{M}$ contains the surface condition and ω is the frequency of the external tidal potential. Since ω is known, (1.106) represents the set of linear equations to be solved in order to get the tidal deformation and the incremental potential.

1.6 Quality factors

Anelastic dissipation of the compressional and shear energy causes the attenuation of the free oscillations. The modal amplitude decreases with time proportionally to $\exp\left(-\frac{\omega t}{2Q}\right)$, where Q is the quality factor of a mode. When Q is large, the mode is attenuated slowly. In the Earth, the quality factors vary from 90 to 5500. However, only the first few radial modes achieve the values higher than 1000, whereas Q of other modes are lower.

The value of Q can be determined by the equation (Dahlen and Tromp, 1998, eq. 9.54)

$$Q^{-1} = 2\omega^{-1}\int_0^R \left(\kappa K_\kappa Q_\kappa^{-1} + \mu K_\mu Q_\mu^{-1}\right) dr, \tag{1.107}$$

where $\kappa = \lambda + \frac{2}{3}\mu$ is the incompressibility modulus, $Q_\kappa(r)$ and $Q_\mu(r)$ are the bulk and shear quality factors of the model and the Fréchet kernels K_κ and K_μ depend on the modal frequencies and eigenfunctions by the formulas

$$\begin{aligned} 2\omega K_\mu &= (2rU' - 2U + NV)^2/3 + N(rV' - V + U)^2 + \\ &\quad + N(rW' - W)^2 + N(N-2)(V^2 + W^2), \qquad (1.108) \\ 2\omega K_\kappa &= (rU' + 2U - NV)^2. \qquad (1.109) \end{aligned}$$

In our calculations we use Q_κ and Q_μ from the PREM (Dziewonski and Anderson, 1981) but there is a series of other models (e.g., Sailor and Dziewonski, 1978; Durek and Ekström, 1996; Widmer et al., 1991; Lawrence and Wysession, 2005) because the knowledge of anelasticity is much poorer than that of elasticity and density (Masters and Gilbert, 1983). This is the reason why we reevaluate the quality factors of several gravest modes from the attenuation of superconducting-gravimeter signals, where they play a key role.

The seismic velocities $v_p = \sqrt{\kappa/\rho}$ and $v_s = \sqrt{\mu/\rho}$ are thus frequency dependent. The PREM velocities are given at the reference frequency of $\omega_{\rm ref}/(2\pi) = 1$ Hz and have to be modified according to dispersion relations by Kanamori and Anderson (1977),

$$v_s(\omega) = v_s(\omega_{\rm ref}) \left(1 + \frac{\ln \frac{\omega}{\omega_{\rm ref}}}{\pi Q_\mu}\right), \qquad (1.110)$$

$$v_p(\omega) = v_p(\omega_{\rm ref}) \left[1 + \frac{\ln \frac{\omega}{\omega_{\rm ref}}}{\pi} \left(\frac{1-E}{Q_\kappa} + \frac{E}{Q_\mu}\right)\right], \qquad (1.111)$$

where $E = \frac{4}{3}(v_s/v_p)^2$. Frequency-dependent values of $\lambda(\omega)$ and $\mu(\omega)$ stem from these relations easily.

1.7 Interpolations

When we compute modes for a chosen fiducial frequency ω_0 of the model, the question arises how to correct the modal frequencies different from the fiducial one. Dahlen and Tromp (1998) derived the explicit formula for the first-order perturbation $\delta\omega_{\rm d}$ of the eigenfrequency ω,

$$\delta\omega_{\rm d} = \omega \frac{\ln \frac{\omega}{\omega_0}}{\pi Q}. \qquad (1.112)$$

However, some spheroidal eigenfunctions are very sensitive to the fiducial frequency ω_0 (see Fig. 1.1). This is the reason why we solved the whole matrix-eigenvalue problems for several fiducial frequencies and interpolated them to obtain better approximation of both the modal eigenfunctions and eigenfrequencies and, subsequently, the quality factors. If T_1 and T_2 are the modal periods corresponding to the fiducial periods $T1$, and $T2$, $T1 < T2$, we can write approximative relation for the corrected modal period

$$T = T_1 + \frac{\log(T_1 + T_2)/2 - \log T1}{\log T2 - \log T1}(T_2 - T_1). \qquad (1.113)$$

The analogous relations can be written for the eigenfunctions U, V and F,

$$U = U_1 + \frac{\log T - \log T1}{\log T2 - \log T1}(U_2 - U_1), \quad \ldots \qquad (1.114)$$

and for the quality factors Q

$$Q = Q_1 + \frac{\log T - \log T1}{\log T2 - \log T1}(Q_2 - Q_1). \tag{1.115}$$

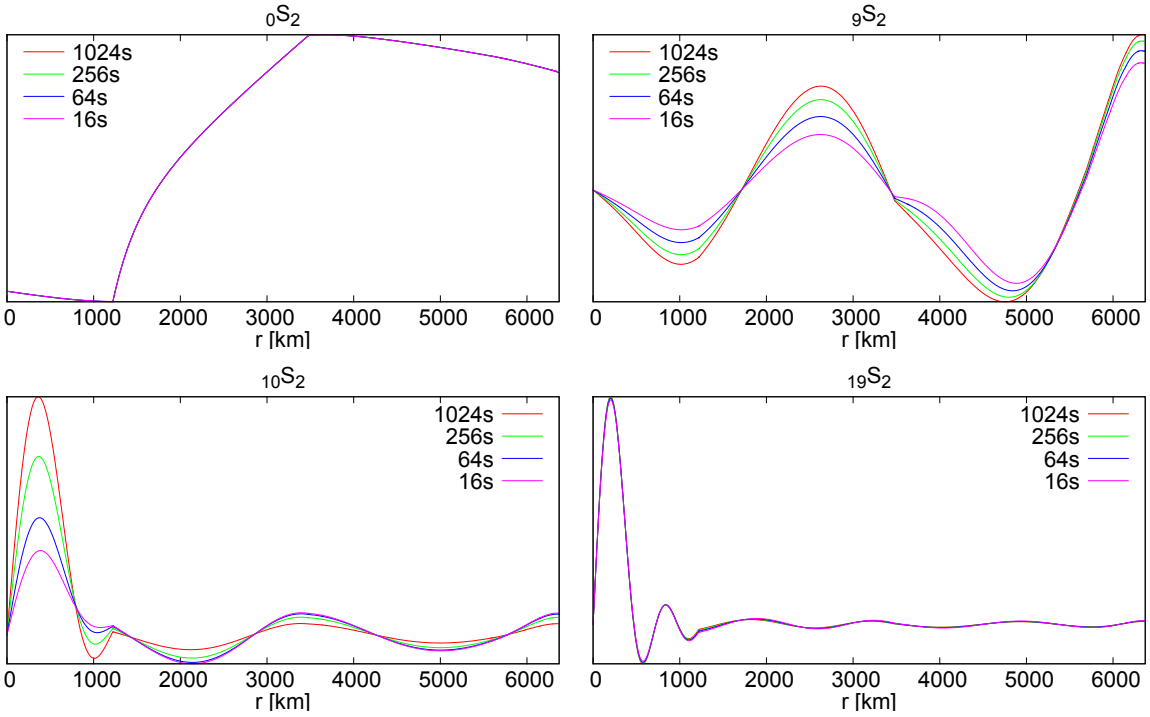

Figure 1.1: The radial eigenfunctions U of selected overtones ${}_nS_2$ for several fiducial periods.

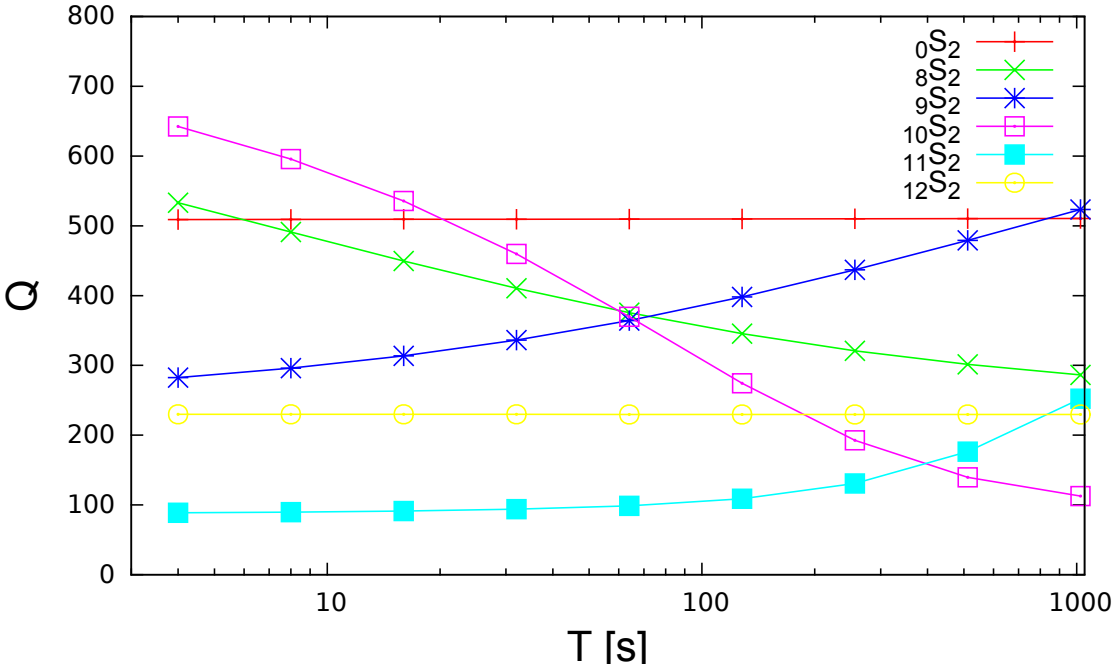

Figure 1.2: Dependence of the quality factors on the fiducial period.

If a modal quality factor Q is low (about 80–90), the correction $\delta\omega_{\mathrm{d}}$ can be so high that the sequence of the overtones is disarranged. For this reason we compute the "distance integral" $\int_0^R[(U_1-U_2)^2+(V_1-V_2)^2]\rho r^2 dr$ to evaluate the correspondence of the overtones. If Q obtained from (1.115) agrees well with the value yielded by (1.107), we consider these modes to be corresponding[1].

Fig. 1.1 shows the frequency dependence of eigenfunctions U for several overtones of the angular degree $l = 2$. The eigenfrequencies and eigenfunctions were computed for four fiducial periods of the PREM (1024 s, 256 s, 64 s, 16 s). Whereas the eigenfunctions of the fundamental mode ${}_0S_2$ are almost independent of the choice of the fiducial period, the eigenfunctions of the modes ${}_9S_2$ and ${}_{10}S_2$ are quite sensitive. Since Q depends on the eigenfunctions, its values vary between 510.4 and 509.3 for mode ${}_0S_2$, 523.4 and 313.6 for mode ${}_9S_2$, 112.6 and 535.8 for mode ${}_{10}S_2$. The former values correspond to the fiducial period of 1024 s and the latter to that of 16 s. The dependence is shown in Fig. 1.2.

1.8 Numerical tests

In order to benchmark our software, we compare our eigenfrequencies and eigenfunctions with those computed by the Mineos software package[2]. The number of radial grid points in our calculations was 2019 for spheroidal modes and 1065 for toroidal modes. The Mineos software was configured to neglect the gravitational terms for frequencies above 40 mHz and the parameter controlling the accuracy of the Runge-Kutta integration scheme *eps* was set to 10^{-9}–10^{-12}. Fig. 1.3 shows the relative differences of the eigenfrequencies and Fig. 1.4 yields the relative differences of the quality factors for both toroidal and spheroidal modes. All modes with angular degrees up to 500 and overtones with $n \leq 300$ for spheroidal modes and $n \leq 210$ for toroidal modes are included. The chosen span of the angular degrees and overtone numbers guaranties that all modes up to 50 mHz are included into this test; however, most of the frequencies are higher (but all below 250 mHz). Both the Mineos and our code computed the eigenfrequencies and eigenfunctions of the isotropic PREM with the fiducial frequency $\omega_0/(2\pi) = 100$ mHz in the toroidal case and with several fiducial frequencies with subsequent interpolations in the spheroidal case.

We achieved excellent agreement for all toroidal modes since the choice of the fiducial frequency plays a minor role in this case. As to the frequencies, we obtained relative differences less than 10^{-5} for most of the modes and less than 10^{-7} for the modes with frequencies near 100 mHz. Toroidal quality-factor uncertainties can increase up to 1% in the worst scenario. As to the spheroidal frequencies, the relative differences are less than 10^{-4} for most of the modes and the worst relative difference is about 10^{-3}. We received significant differences in quality factors of the spheroidal modes when the Mineos did not converge, otherwise the agreement was better than 95%.

[1] There are exceptional cases (less then 0.1% of the total number of the modes up to the frequency 250 mHz) when we are not able to find the corresponding mode rising from neighbouring fiducial periods. In such cases we do not interpolate and take the modal periods and eigenfunctions from the solution on the closer fiducial frequency.

[2] http://geodynamics.org/cig/software/mineos/

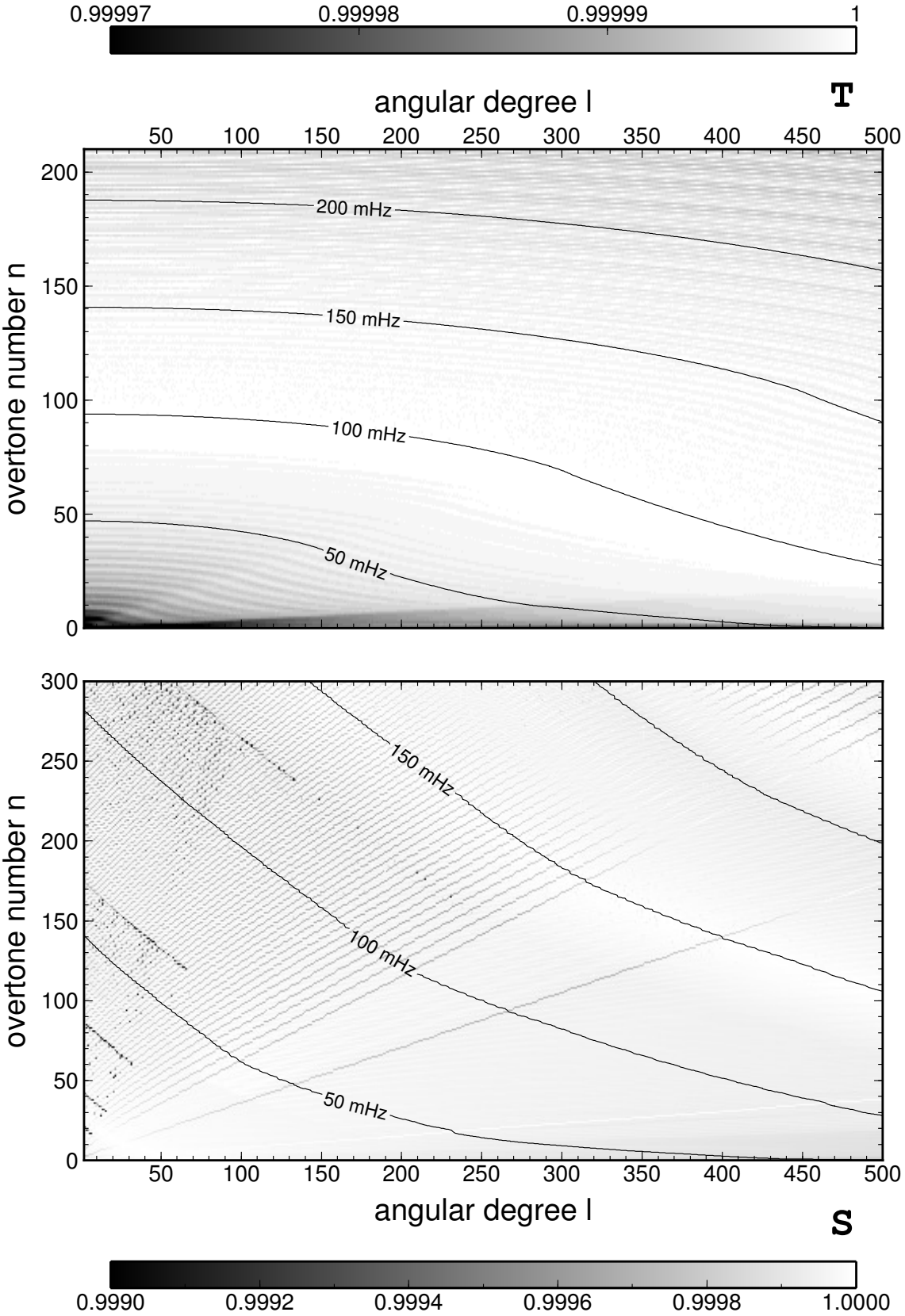

Figure 1.3: Relative differences between the normal-mode frequencies obtained by the Mineos and our matrix-eigenvalue software for the angular degrees up to 500. The upper panel show the toroidal modes and the lower panel show the spheroidal modes.

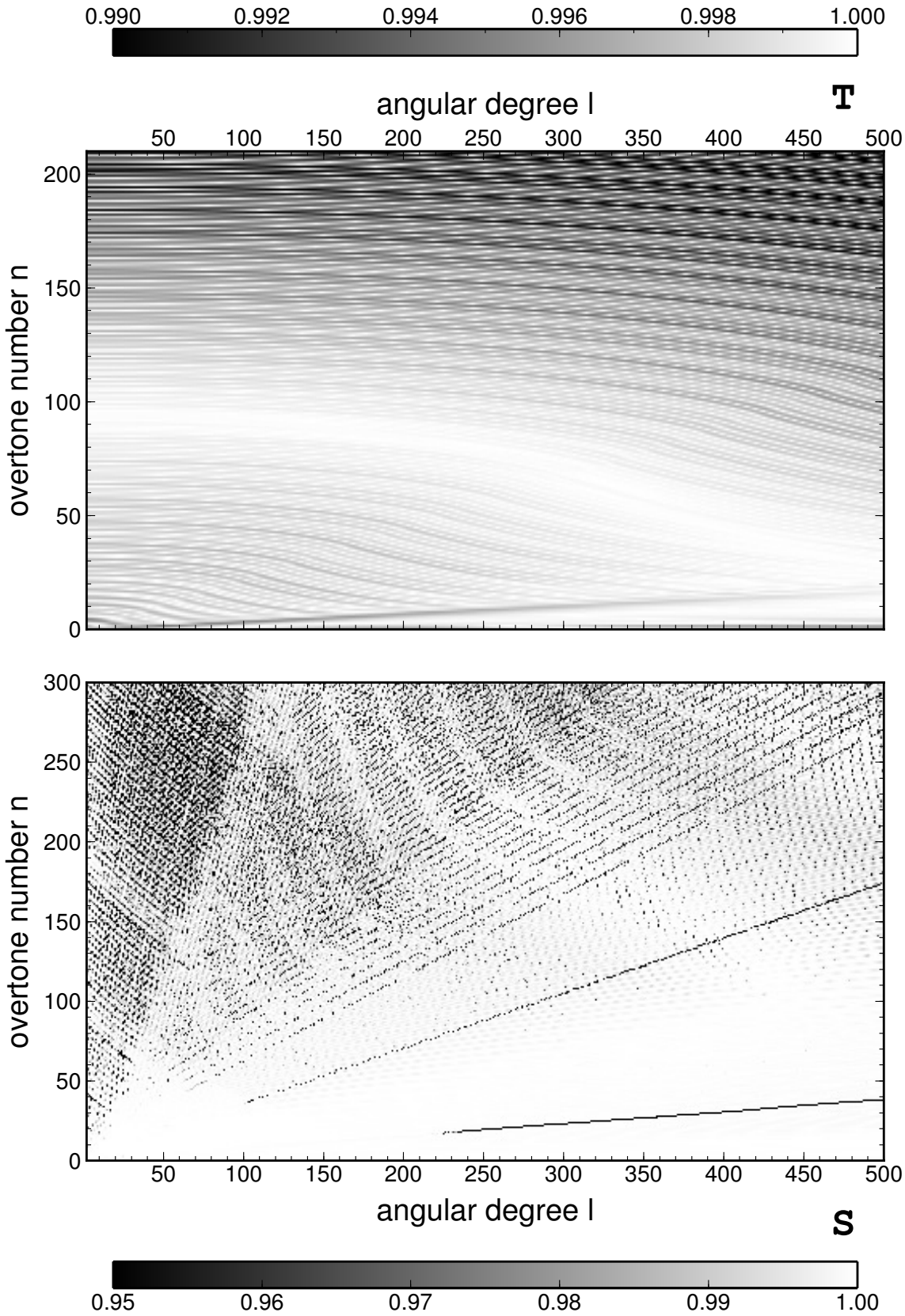

Figure 1.4: Relative differences between the normal-mode quality factors obtained by the Mineos and our matrix-eigenvalue software for the angular degrees up to 500. The upper panel show the toroidal modes and the lower panel show the spheroidal modes.

Chapter 2

Synthetic accelerograms

In the previous chapter, we described the matrix eigenvalue approach that allows us to calculate the normal-mode frequencies and eigenfunctions. In this chapter, we show how to calculate the response of an (an)elastic and (a)spherical Earth to seismic events. We start with the general equations that describe the splitting of an isolated multiplet as a consequence of the effects of the Earth rotation and hydrostatic ellipticity. Then we describe the response of a spherical non-rotating Earth. All the relations that we have used to calculate synthetic seismograms are presented in this chapter, so that one may follow all the numerical steps. The formulas are adopted from Dahlen and Tromp (1998) and Dahlen and Sailor (1979) and reproduced here without derivation.

2.1 Splitting of an isolated multiplet

The splitting of free oscillations due to the rotation and associated ellipticity significantly affects the spectra of the gravest modes; however, splitting due to other perturbations such as lateral heterogeneity and anisotropy can also be important. The multiplets of free oscillations are non-degenerated, and there are $2l+1$ singlets of close frequencies for every angular degree l. We use the azimuthal order $m = -l, \ldots, l$ to denote individual singlets.

Let $\mathbf{x}(r, \vartheta, \phi)$ be the position vector of the receiver and $\mathbf{x}_s(r_s, \vartheta_s, \phi_s)$ the position vector of the seismic point source. The unit basis of mutually perpendicular vectors $\mathbf{e}_r$, $\mathbf{e}_\vartheta$ and $\mathbf{e}_\phi$ is defined in the direction of increasing radius r, colatitude ϑ and longitude ϕ at the location of a receiver $\mathbf{x}$, and the basis $\mathbf{e}^s_r$, $\mathbf{e}^s_\vartheta$ and $\mathbf{e}^s_\phi$ is defined in the direction of increasing radius r_s, colatitude ϑ_s and longitude ϕ_s at the location of a source $\mathbf{x_s}$. We consider a seismic point source described by the moment tensor $\mathbf{M}$ and an elliptical Earth model rotating with the sidereal angular velocity Ω. The acceleration response at the receiver position $\mathbf{x}$ in time t for an isolated multiplet is

$$\begin{aligned} a(\boldsymbol{x}, t) &= \mathrm{Re} \sum_m \left[1 + m\chi(\Omega\omega_0^{-1}) - \tau(1 - 3m^2N^{-1})\right] r^*_m s_m \times \\ &\quad \times \exp\left[i\omega_0 \left(1 + a + bm + cm^2 + i(2Q)^{-1}\right) t\right], \end{aligned} \tag{2.1}$$

where $N = l(l+1)$, ω_0 is the frequency and Q the quality factor of the degenerated multiplet, χ is the Coriolis splitting parameter, see (2.7) below, a, b and c are splitting parameters (2.10)–(2.12) and τ is the auxiliary variable (2.13). Complex scalars r_m and s_m are related to the displacement evaluated in the receiver and

source positions, respectively, for each singlet denoted by m. An asterisk stands for complex conjugation. The scalar r_m represents the component of the displacement in the direction $\boldsymbol{\nu}$ in the receiver position (e.g., polarization of the accelerometer),

$$r_m(\mathbf{x}) \;=\; \boldsymbol{\nu}\cdot\mathbf{u}^*_m(\mathbf{x}) = \nu_r u^*_r + \nu_\vartheta u^*_\vartheta + \nu_\phi u^*_\phi, \quad |\boldsymbol{\nu}| = 1, \tag{2.2}$$

where the spherical components of the displacement $\mathbf{u}$ are

$$\begin{aligned} u_r &= \mathbf{e}_r\cdot\mathbf{u}_m = UY_{lm}, \\ u_\vartheta &= \mathbf{e}_\vartheta\cdot\mathbf{u}_m = V\partial_\vartheta Y_{lm} + imW(\sin\vartheta)^{-1}Y_{lm}, \\ u_\phi &= \mathbf{e}_\phi\cdot\mathbf{u}_m = imV(\sin\vartheta)^{-1}Y_{lm} - W\partial_\vartheta Y_{lm}. \end{aligned} \tag{2.3}$$

The scalar s_m is defined by

$$\begin{aligned} s_m(\mathbf{x}_s) &= \mathbf{M} : \boldsymbol{\varepsilon}^*_m(\mathbf{x}_s) \\ &= M_{rr}\varepsilon^*_{rrs} + M_{\vartheta\vartheta}\varepsilon^*_{\vartheta\vartheta s} + M_{\phi\phi}\varepsilon^*_{\phi\phi s} + 2(M_{r\vartheta}\varepsilon^*_{r\vartheta s} + M_{r\phi}\varepsilon^*_{r\phi s} + M_{\vartheta\phi}\varepsilon^*_{\vartheta\phi s}), \end{aligned} \tag{2.4}$$

where $\boldsymbol{\varepsilon}_m$ is the strain tensor, $\boldsymbol{\varepsilon}_m = \frac{1}{2}\left[\nabla\mathbf{u}_m + (\nabla\mathbf{u}_m)^{\mathrm{T}}\right]$, and the subscript s denotes evaluation at the source position $\mathbf{x}_s$. The spherical components of $\boldsymbol{\varepsilon}_m$ are

$$\begin{aligned} \varepsilon_{rr} &= U'Y_{lm}, \\ \varepsilon_{\vartheta\vartheta} &= r^{-1}UY_{lm} - r^{-1}V\left[\cot\vartheta\partial_\vartheta Y_{lm} - m^2(\sin\vartheta)^{-2}Y_{lm} + NY_{lm}\right] + \\ &\quad + imr^{-1}W(\sin\vartheta)^{-1}\left(\partial_\vartheta Y_{lm} - \cot\vartheta Y_{lm}\right), \\ \varepsilon_{\phi\phi} &= r^{-1}UY_{lm} + r^{-1}V\left[\cot\vartheta\partial_\vartheta Y_{lm} - m^2(\sin\vartheta)^{-2}Y_{lm}\right] - \\ &\quad - imr^{-1}W(\sin\vartheta)^{-1}\left(\partial_\vartheta Y_{lm} - \cot\vartheta Y_{lm}\right), \\ \varepsilon_{r\vartheta} &= \tfrac{1}{2}\left[x\partial_\vartheta Y_{lm} + imz(\sin\vartheta)^{-1}Y_{lm}\right], \\ \varepsilon_{r\phi} &= \tfrac{1}{2}\left[imx(\sin\vartheta)^{-1}Y_{lm} - z\partial_\vartheta Y_{lm}\right], \\ \varepsilon_{\vartheta\phi} &= imr^{-1}V(\sin\vartheta)^{-1}\left(\partial_\vartheta Y_{lm} - \cot\vartheta Y_{lm}\right) + \\ &\quad + r^{-1}W\left[\cot\vartheta\partial_\vartheta Y_{lm} - m^2(\sin\vartheta)^{-2}Y_{lm} + \tfrac{1}{2}NY_{lm}\right], \end{aligned} \tag{2.5}$$

where two auxiliary variables x and z are defined as

$$\begin{aligned} x &= V' - r^{-1}V + r^{-1}U, \\ z &= W' - r^{-1}W. \end{aligned} \tag{2.6}$$

The Coriolis splitting parameter, first introduced by Backus and Gilbert (1961),

$$\chi = \int_0^R \rho(V^2 + 2UV + W^2)r^2dr, \tag{2.7}$$

describes the first-order effect of the Earth rotation, while the centrifugal potential and the associated ellipticity perturbation are ignored. The eigenfrequency perturbations are then linear,

$$\delta\omega_m = m\chi\Omega, \quad -l \le m \le l. \tag{2.8}$$

The radial modes ${}_n\mathrm{S}_0$ are not affected by this first-order effect of rotation since they are non-degenerate. The normalization condition (1.39) of the toroidal modes ${}_n\mathrm{T}_l$ implies that

$$\chi = N^{-1}. \tag{2.9}$$

The rotational and elliptical splitting parameters a, b and c have the form,

$$a = \tfrac{1}{3}(1 - N\chi)(\Omega/\omega_0)^2 + \tfrac{1}{2}(\upsilon\omega_0^{-2} - \tau) + \alpha_2(\Omega/\omega_0)^2, \tag{2.10}$$

$$b = \chi(\Omega/\omega_0), \tag{2.11}$$

$$c = -\tfrac{3}{2}N(\upsilon\omega_0^{-2} - \tau) + \gamma_2(\Omega/\omega_0)^2. \tag{2.12}$$

The first term in (2.10) represents the effect of the spherical part of the centrifugal potential and the second term is caused by the combined effects of the degree-two perturbations of the centrifugal potential and ellipticity. The rotational splitting parameter b arises from the first-order effect of the Coriolis force, whereas the correction parameters α_2 and γ_2 are related to the second-order effect of the Coriolis force. The auxiliary variables τ and υ in (2.1), (2.10) and (2.12), as well as α_2 and γ_2, are expressed in the next section.

2.2 Splitting parameters

This section contains relations necessary to determine splitting parameters of a free-oscillation isolated multiplet. We use R, $R_{\rm CMB}$ and $R_{\rm ICB}$ to denote, respectively, the radius of the Earth, outer core and inner core, and ρ, μ and κ are the density, shear modulus and incompressibility modulus, respectively. Auxiliary variables τ and υ that occur in (2.1) and (2.10)–(2.12) are defined as

$$\tau = \frac{N}{4N-3}\int_0^R \tfrac{2}{3}\epsilon\rho\left[\bar{T}_\rho - (\eta+3)\check{T}_\rho\right] r^2 dr, \tag{2.13}$$

$$\begin{aligned}\upsilon = \frac{N}{4N-3}\int_0^R \tfrac{2}{3}\epsilon\Big(&\kappa\left[\bar{V}_\kappa - (\eta+1)\check{V}_\kappa\right] + \\ &+ \mu\left[\bar{V}_\mu - (\eta+1)\check{V}_\mu\right] + \rho\left[\bar{V}_\rho - (\eta+3)\check{V}_\rho\right]\Big) r^2 dr,\end{aligned} \tag{2.14}$$

where the ellipticity $\epsilon(r)$ is given by

$$\epsilon(r) \approx \epsilon_R \exp\left(-\int_r^R \tilde{\eta}\tilde{r}^{-1} d\tilde{r}\right) \tag{2.15}$$

and the auxiliary variable $\eta(r)$ defined as $\eta = r\epsilon'/\epsilon$ can be approximately written as

$$\eta(r) \approx \frac{25}{4}\left(1 - \frac{\int_0^r \tilde{\rho}\tilde{r}^4 d\tilde{r}}{r^2\int_0^r \tilde{\rho}\tilde{r}^2 d\tilde{r}}\right)^2 - 1. \tag{2.16}$$

The approximate relation of the hydrostatic surface ellipticity ϵ_R is

$$\epsilon_R \approx \frac{10\Omega^2 a^3/(GM)}{4 + 25[1 - \frac{3}{2}I/(Ma^2)]^2}, \tag{2.17}$$

where G is the gravitational constant, M the mass of the Earth model and the moment of inertia I is related to ρ by

$$I = \frac{8}{3}\pi\int_0^R \rho r^4 dr. \tag{2.18}$$

The density, incompressibility and rigidity kernels $\bar{T}_\rho$, $\check{T}_\rho$, $\bar{V}_\rho$, $\check{V}_\rho$, $\bar{V}_\mu$, $\check{V}_\mu$, $\bar{V}_\kappa$, $\check{V}_\kappa$ in equations (2.13) and (2.14) have the form,

$$\begin{aligned}
\bar{T}_\rho &= -6UV, && (2.19)\\
\check{T}_\rho &= U^2 + (N-3)(V^2+W^2), && (2.20)\\
\bar{V}_\rho &= 2f(rF' + 4\pi G\rho r U + gU) - 6r^{-1}gUV + \\
&\quad +6r^{-1}gU^2 + 2r^{-1}[(N-3)V - NU]F, && (2.21)\\
\check{V}_\rho &= 2(N-3)r^{-1}FV + U(2F' + 8\pi G\rho U - 6gr^{-1}V), && (2.22)\\
\bar{V}_\mu &= \tfrac{2}{3}(2U'-f)(2U'+9V'-12r^{-1}V) + 2x[3U' - (N-3)V' - 3r^{-1}NV] + \\
&\quad +18(N-2)r^{-1}(VV' + WW') - 2(N-3)zW', && (2.23)\\
\bar{V}_\mu &= (N-12)(N-2)r^{-2}(V^2+W^2) + (N-3)(x^2+z^2-2xV'-2zW') - \\
&\quad -\tfrac{2}{3}(2U'-f)(U' + \tfrac{1}{2}f - 6r^{-1}V), && (2.24)\\
\bar{V}_\kappa &= -2(U'+f)(U'+3r^{-1}V), && (2.25)\\
\check{V}_\kappa &= -(U'+f)(U'-f-6r^{-1}V). && (2.26)
\end{aligned}$$

where the auxiliary variable f is defined as

$$f = r^{-1}(2U - NV). \qquad (2.27)$$

The second-order Coriolis correction parameters α_2 and γ_2 for spheroidal modes given by Dahlen and Sailor (1979) have the form

$$\begin{aligned}
\alpha_2 &= \frac{2l^2(l-1)^2}{(2l+1)(2l-1)}A + \frac{2(l+2)^2(l+1)^2}{(2l+3)(2l+1)}B, && (2.28)\\
\gamma_2 &= \tfrac{1}{2}\chi^2 - \frac{2(l-1)^2}{(2l+1)(2l-1)}A - \frac{2(l+2)^2}{(2l+3)(2l+1)}B + 2C. && (2.29)
\end{aligned}$$

The quantity A represents the contribution of all toroidal modes of degree $l-1$,

$$\begin{aligned}
A &= \frac{1}{l(l-1)}\int_{R_{\rm ICB}}^{R_{\rm CMB}} \rho_0 \left[U + (l+1)V\right]^2 r^2 dr + \\
&\quad + \sum_{\check{n}\,{}_0{\rm T}_{l-1}} \left(\frac{\omega_0^2}{\omega_0^2 - \tilde{\omega}_0^2}\right)\left(\int_0^{R_{\rm ICB}} \rho_0 \left[U + (l+1)V\right]\tilde{W} r^2 dr\right)^2 + \\
&\quad + \sum_{\check{n}\,{}_0{\rm T}_{l-1}} \left(\frac{\omega_0^2}{\omega_0^2 - \tilde{\omega}_0^2}\right)\left(\int_{R_{\rm CMB}}^{R} \rho_0 \left[U + (l+1)V\right]\tilde{W} r^2 dr\right)^2, && (2.30)
\end{aligned}$$

B represents the contribution of all toroidal modes of degree $l+1$,

$$\begin{aligned}
B &= \frac{1}{(l+1)(l+2)}\int_{R_{\rm ICB}}^{R_{\rm CMB}} \rho_0 \left[U - lV\right]^2 r^2 dr + \\
&\quad + \sum_{\check{n}\,{}_0{\rm T}_{l+1}} \left(\frac{\omega_0^2}{\omega_0^2 - \tilde{\omega}_0^2}\right)\left(\int_0^{R_{\rm ICB}} \rho_0 \left[U - lV\right]\tilde{W} r^2 dr\right)^2 + \\
&\quad + \sum_{\check{n}\,{}_0{\rm T}_{l+1}} \left(\frac{\omega_0^2}{\omega_0^2 - \tilde{\omega}_0^2}\right)\left(\int_{R_{\rm CMB}}^{R} \rho_0 \left[U - lV\right]\tilde{W} r^2 dr\right)^2 && (2.31)
\end{aligned}$$

and C represents the contribution of all spheroidal modes of degree l,

$$C = \sum_{\substack{\check{n}\,{}_0{\rm S}_l \\ \check{n}\neq n}} \left(\frac{\omega_0^2}{\omega_0^2 - \tilde{\omega}_0^2}\right)\left(\int_0^R \rho_0 \left[U\tilde{V} + \tilde{U}V + V\tilde{V}\right] r^2 dr\right)^2. \qquad (2.32)$$

In both equations (2.30) and (2.31), the first term represents the contribution from the secular toroidal modes of the fluid outer core with $\omega_0 = 0$, and $W = 0$ in the inner core and mantle; in the fluid W may be selected arbitrarily. These degenerate solutions exist thanks to the inability of the fluid core to resist any shear force. The second term in equations (2.30) and (2.31) is the contribution from the inner-core toroidal modes. These modes are completely decoupled from the rest of the Earth, while the spheroidal inner-core modes generate a weak signal at the surface. The third term arises from the usual toroidal mode of the mantle. The sum in the equation (2.32) contains the usual spheroidal modes and gravitational spheroidal modes confined largely to the fluid core.

We have to treat the cases $l = 0, 1$ and 2 separately to keep the equations (2.28) and (2.29) valid,

$$\begin{aligned} l &= 0: \\ A &\rightarrow 0, \\ B &\rightarrow B + \left[\frac{\left(\int_0^{R_{\rm ICB}} \rho_0 r^3 U dr \right)^2}{2 \int_0^{R_{\rm ICB}} \rho_0 r^4 dr} + \frac{\left(\int_{R_{\rm CMB}}^{R} \rho_0 r^3 U dr \right)^2}{2 \int_{R_{\rm CMB}}^{R} \rho_0 r^4 dr} \right] \end{aligned} \tag{2.33}$$

$$\begin{aligned} l &= 1: \\ A &\rightarrow 0 \end{aligned} \tag{2.34}$$

$$\begin{aligned} l &= 2: \\ A &\rightarrow A + \left[\frac{\left(\int_0^{R_{\rm ICB}} \rho_0 r^3 [U + 3V] dr \right)^2}{2 \int_0^{R_{\rm ICB}} \rho_0 r^4 dr} + \frac{\left(\int_{R_{\rm CMB}}^{R} \rho_0 r^3 [U + 3V] dr \right)^2}{2 \int_{R_{\rm CMB}}^{R} \rho_0 r^4 dr} \right]. \end{aligned} \tag{2.35}$$

The additional terms represent the contribution of the inner-core and mantle rigid rotational modes. The rigid translational mode ${}_0S_1$ makes no additional contribution to C for $l = 1$ because of orthogonality.

The second-order Coriolis correction parameters α_2 and γ_2 for mantle toroidal modes given by Dahlen and Sailor (1979) have the form

$$\alpha_2 = \frac{2N^2}{(2l+1)(2l-1)} A + \frac{2N^2}{(2l+3)(2l+1)} B, \tag{2.36}$$

$$\gamma_2 = \frac{1}{2N} - \frac{2(l+1)^2}{(2l+1)(2l-1)} A - \frac{2l^2}{(2l+3)(2l+1)} B, \tag{2.37}$$

where the quantity A represents the contribution of all the spheroidal modes of degree $l-1$,

$$A = \sum_{\tilde{n} {\rm S}_{l-1}} \left(\frac{\omega_0^2}{\omega_0^2 - \tilde{\omega}_0^2} \right) \left(\int_{R_{\rm CMB}}^{R} \rho_0 W \left[\tilde{U} - (l-1) \tilde{V} \right] r^2 dr \right)^2 \tag{2.38}$$

and B represents the contribution of all spheroidal modes of degree $l+1$,

$$B = \sum_{\tilde{n} {\rm S}_{l+1}} \left(\frac{\omega_0^2}{\omega_0^2 - \tilde{\omega}_0^2} \right) \left(\int_{R_{\rm CMB}}^{R} \rho_0 W \left[\tilde{U} + (l+2) \tilde{V} \right] r^2 dr \right)^2. \tag{2.39}$$

As in the spheroidal case, the gravitational modes as well as the usual spheroidal modes must be included in the sums A and B. The rigid translation mode ${}_0S_1$ makes no additional contribution to A for $l = 2$ because of the fact that $U = V$.

2.3 Synthetic accelerograms on a non-rotating sphere

The angular epicentral distance Θ between the source and receiver positions is given by

$$\cos\Theta = \mathbf{e}_r \cdot \mathbf{e}_r^s = \cos\vartheta\cos\vartheta_s + \sin\vartheta\sin\vartheta_s\cos(\phi - \phi_s). \tag{2.40}$$

The azimuth to the receiver Φ, measured in a counterclockwise sense from due south at the source, is defined as

$$\cos\Phi = \frac{-\cos\theta\sin\theta_s + \sin\theta\cos\theta_s\cos(\phi - \phi_s)}{\sin\Theta}. \tag{2.41}$$

The acceleration response of a non-rotating anelastic Earth to a step-function moment-tensor source $\mathbf{M}$ situated at $\mathbf{x}_s$ is given at the location of receiver $\mathbf{x}$ by equation

$$\mathbf{a}(\mathbf{x}, t) = \sum_{n=0}^{\infty}\sum_{l=0}^{\infty} {}_n\mathbf{A}_l(\mathbf{x})\cos({}_n\omega_l t)\exp\left(-\frac{\omega t}{2Q}\right), \tag{2.42}$$

where the amplitude of excitation has the form

$${}_n\mathbf{A}_l(\mathbf{x}) = \left(\frac{2l+1}{4\pi}\right)\mathbf{D}\left(r, \Theta, \Phi\right){}_nA_l\left(\Theta, \Phi\right). \tag{2.43}$$

The displacement operator $\mathbf{D}$ of the receiver in the epicentral representation is

$$\mathbf{D}\left(r, \Theta, \Phi\right) = \left(U, \left[V\partial_\Theta + W(\sin\Theta)^{-1}\partial_\Phi\right], \left[V(\sin\Theta)^{-1}\partial_\Phi - W\partial_\Theta\right]\right)^{\mathrm{T}} \tag{2.44}$$

and the scalar function ${}_nA_l$ evaluated at the source $\mathbf{x}_s$ has the form

$$\begin{aligned}
{}_nA_l\left(\Theta, \Phi\right) &= \sum_{m=0}^{2} P_{lm}(\cos\Theta)(A_m\cos m\Phi + B_m\sin m\Phi), && (2.45)\\
A_0 &= M_{rr}\dot{U}_s + (M_{\theta\theta} + M_{\phi\phi})r_s^{-1}(U_s - \frac{1}{2}NV_s), && (2.46)\\
B_0 &= 0, && (2.47)\\
A_1 &= M_{r\theta}(\dot{V}_s - r_s^{-1}V_s + r_s^{-1}U_s) - M_{r\phi}(\dot{W}_s - r_s^{-1}W_s), && (2.48)\\
B_1 &= M_{r\phi}(\dot{V}_s - r_s^{-1}V_s + r_s^{-1}U_s) + M_{r\theta}(\dot{W}_s - r_s^{-1}W_s), && (2.49)\\
A_2 &= r_s^{-1}\left[\frac{1}{2}(M_{\theta\theta} - M_{\phi\phi})V_s - M_{\theta\phi}W_s\right], && (2.50)\\
B_2 &= r_s^{-1}\left[M_{\theta\phi}V_s + \frac{1}{2}(M_{\theta\theta} - M_{\phi\phi})W_s\right]. && (2.51)
\end{aligned}$$

Fig. 2.1 shows the three-component records of the synthetic acceleration following the 2010 Maule earthquake calculated for the station Pecný (PE: 49.92N, 14.79E), Czech Republic. The Global CMT Project Moment Tensor Solution (GCMT) with $M_0 = 1.84 \times 10^{22}$ Nm ($M_{rr} = 1.04$, $M_{\theta\theta} = -0.03$, $M_{\phi\phi} = -1.01$, $M_{r\theta} = 0.227$, $M_{r\phi} = -1.51$ and $M_{\theta\phi} = -0.12$) is used as the seismic source; the centroid location is 35.95S and 73.15W and depth of 24.1 km. The synthetic signals up to 40 mHz are

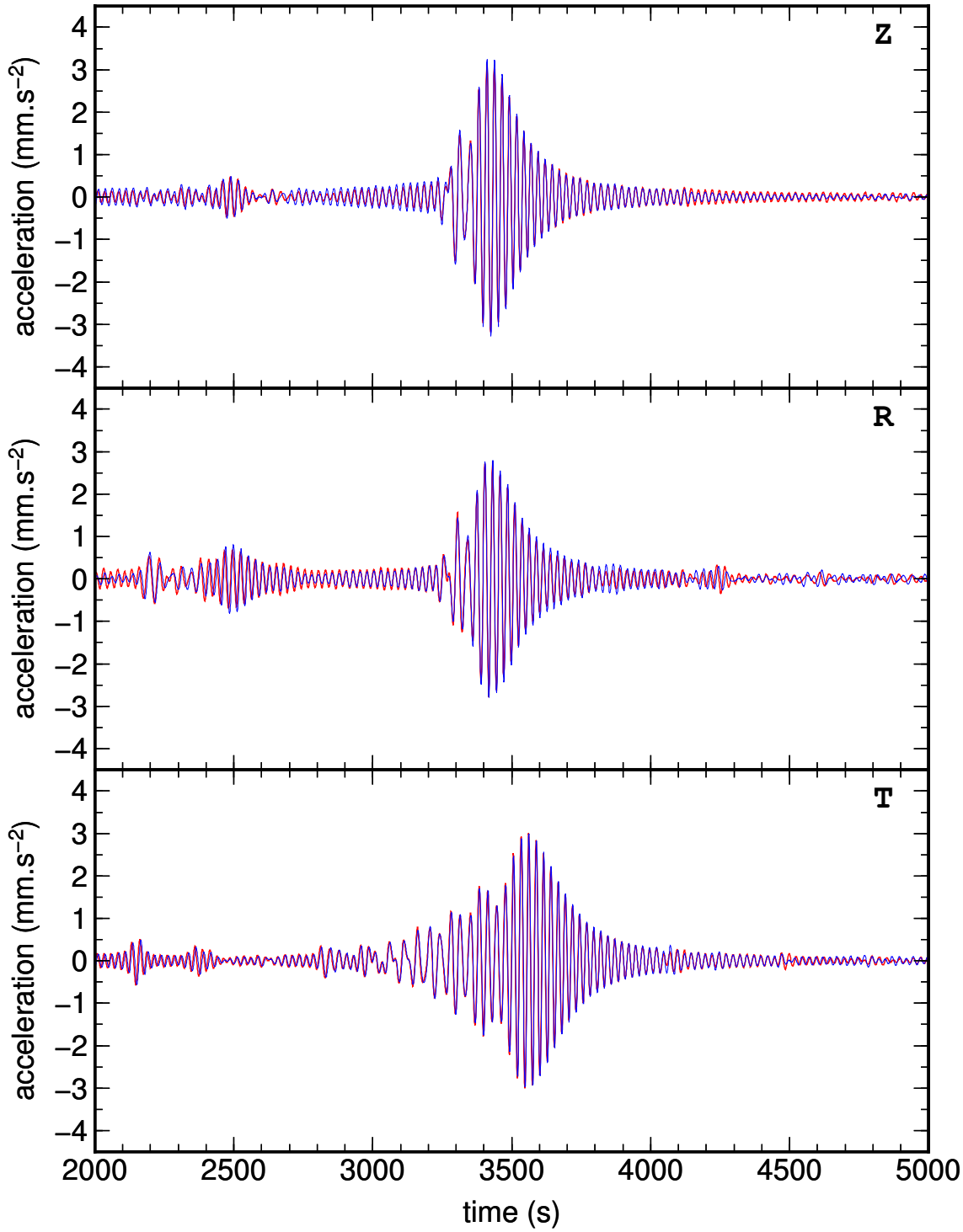

Figure 2.1: Three components (vertical Z,radial R, transverse T) of synthetic accelerograms for the spheroidal and toroidal modes up to 40 mHz generated by the Maule 2010 earthquake at the station PE. The GCMT source solution was chosen to represent the earthquake. Our accelerograms are plotted in red, those calculated using Mineos in blue. Note that the (Z, R)-components (dominated by the Rayleigh waves) are the sums of the spheroidal modes, whereas the T-component (dominated by the Love waves) is formed of toroidal modes. The zero of the time axis corresponds to the origin time of the earthquake.

computed by our code (red) and the Mineos (blue). The vertical component Z as well as the radial component R are generated by the spheroidal modes with insignificant toroidal signal, whereas the transverse component T is formed of toroidal modes.

In the high-Q approximation, the displacement response is

$$\mathbf{s}(\mathbf{x},t) \approx \sum_{n=0}^{\infty}\sum_{l=0}^{\infty} {}_n\omega_l^{-2}\,{}_n\mathbf{A}_l(\mathbf{x}) \left[1-\cos({}_n\omega_l t)\exp\left(-\frac{\omega t}{2Q}\right)\right]. \tag{2.52}$$

The final static displacement of the spherically symmetric Earth can thus be written as

$$\mathbf{s_f}(\mathbf{x}) \approx \sum_{n=0}^{\infty}\sum_{l=0}^{\infty} {}_n\omega_l^{-2}\,{}_n\mathbf{A}_l(\mathbf{x}). \tag{2.53}$$

If the receiver is situated upon the surface of the Earth and we use the fact that $g' = -2a^{-1}g$, the eigenfunctions in the displacement operator (2.44) must be corrected for the effects of the free-air change in gravity due to the radial displacement U_{free}, ground tilt and horizontal acceleration V_{tilt},

$$U_{\text{free}} = 2\,{}_n\omega_l^{-2} g a^{-1} U, \qquad V_{\text{tilt}} = -\,{}_n\omega_l^{-2} g a^{-1} U, \tag{2.54}$$

and for the effect of the perturbation F in the gravitational potential due to the redistribution of the Earth mass,

$$U_{\text{pot}} = (l+1)\,{}_n\omega_l^{-2} a^{-1} F, \qquad V_{\text{pot}} = -\,{}_n\omega_l^{-2} a^{-1} F. \tag{2.55}$$

The spheroidal eigenfunctions in the displacement operator $\mathbf{D}$ (2.44) have to be replaced by $U \to U + U_{\text{free}} + U_{\text{pot}}$ and $V \to V + V_{\text{tilt}} + V_{\text{pot}}$.

Chapter 3

SG records mining

In the previous chapter we have provided the reader with the theoretical background needed for computation of the synthetic seismograms generated by point sources. In this chapter we present its application to low-frequency seismology. We focus on the radial and spheroidal modes in the frequency range up to 1 mHz that affords several advantages by employing the superconducting-gravimeter (SG) data. The SG data following the 2004 Sumatra-Andaman, 2010 Maule, 2011 Tohoku-Oki and 2012 Sumatra earthquakes were assembled within the framework of the GGP (http://www.eas.slu.edu/GGP/ggphome.html; Crossley et al., 1999). The geograph-

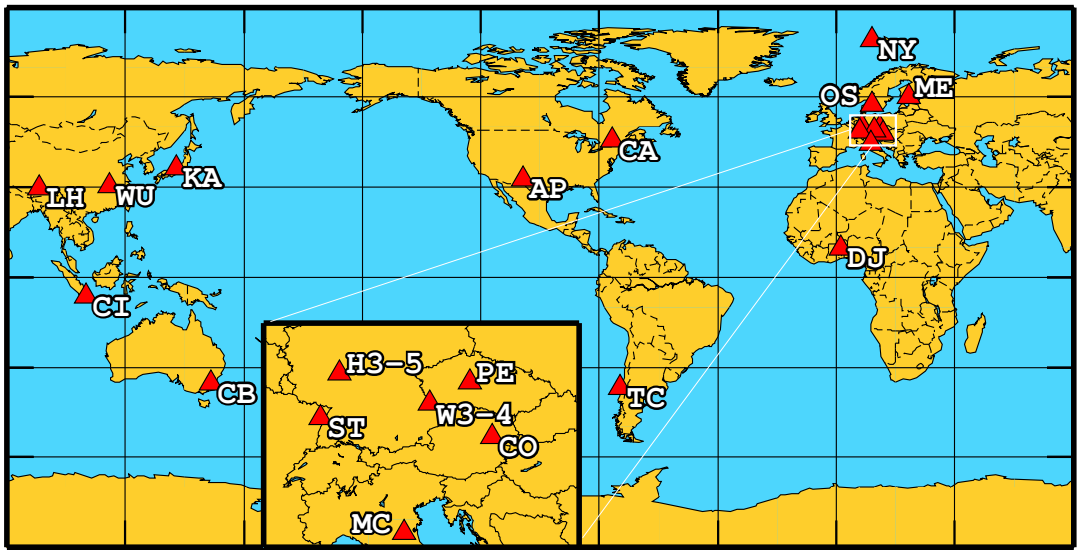

Figure 3.1: Superconducting gravimeter stations providing free data following the megathrust earthquakes within the Global Geodynamics Project.

ical distribution of the Global Geodynamics Project (GGP) stations is shown in Fig. 3.1 and their specifications are listed in Table 3.1. The noise-level analysis of these stations was provided by Rosat and Hinderer (2011).

We demonstrate the determination of the quality factors of individual modes as well as the centroid-moment tensor (CMT) of the events from the SG records. We focus mainly on the 2010 Maule, 2011 Tohoku-Oki and 2012 Sumatra earthquakes in the following text, since the 2004 Sumatra-Andaman earthquake source process is complicated by an extreme fault-plane length of about 1200 km (e.g., Park et al., 2005; Vigny et al., 2005; Ishii et al., 2005; Banerjee et al., 2005; Braitenberg

and Zadro, 2007; de Groot-Hedlin, 2005), and its relatively slow rupture velocity confirmed by many independent studies using various techniques (Krüger and Ohrnberger, 2005; Tolstoy and Bohnenstiehl, 2005; Guilbert et al., 2005; Okal and Stein, 2009; Gahalaut et al., 2010).

acronym	station	latitude	longitude	instrument
AP	Apache Point	32.78N	105.82W	OSG-046
CA	Cantley	45.58N	75.81W	T012 TT70
CB	Canberra	35.32S	149.01E	C031
CI	Cibinong	6.49S	106.85E	C022
CO	Conrad Observatory	47.93N	15.86E	C025
DJ	Djougou	9.74N	1.61E	OSG-060
H3	Bad Homburg	50.23N	8.61E	SG-044
H4	Bad Homburg	50.23N	8.61E	CD029_L
H5	Bad Homburg	50.23N	8.61E	CD029_U
KA	Kamioka	36.43N	137.31E	T016
LH	Lhasa	29.65N	91.04E	SG-057
MC	Medicina	44.52N	11.65E	C023
ME	Metsahovi	60.22N	24.40E	T020
NY	Ny-Alesund	78.93N	11.87E	C039
OS	Onsala	57.39N	11.93E	054
PE	Pecný	49.92N	14.79E	OSG-050
ST	Strasbourg	48.62N	7.68E	C026
TC	TIGO Concepcion	36.84S	73.03W	RT038
W3	Wettzell	49.14N	12.88E	CD030_L
W4	Wettzell	49.14N	12.88E	CD030_U
WU	Wuhan	30.52N	114.49E	T004 TT70

Table 3.1: Specification of the SG stations. More details about the SG sites can be found in Crossley and Hinderer (2009).

3.1 SG data

It is opportune to use the superconducting-gravimeter data for analyzing the ultra-long normal-mode amplitude spectra. Fig. 3.2 shows the range of the observable periods covering eight orders of magnitude from 1 second to several years. The periods of free oscillations are visible both in the broadband seismometer and SG spectra. The SG data are less noisy than seismometer data in the frequency range up to 1 mHz (e.g., Rosat et al., 2002; Widmer-Schnidrig, 2003; Ferreira et al., 2006; Rosat et. al., 2015), but they provide only the vertical component of oscillations.

Table 3.2 shows the header of the data file from the Pecný station in the standard PRETERNA format that is part of the ETERNA Earth tide analysis program (Wenzel, 1996b). The gravity and atmospheric-pressure data are sampled per 1 second and uncorrected to disturbances such as spikes, offsets, and other problems. Provided data files contain monthly data.

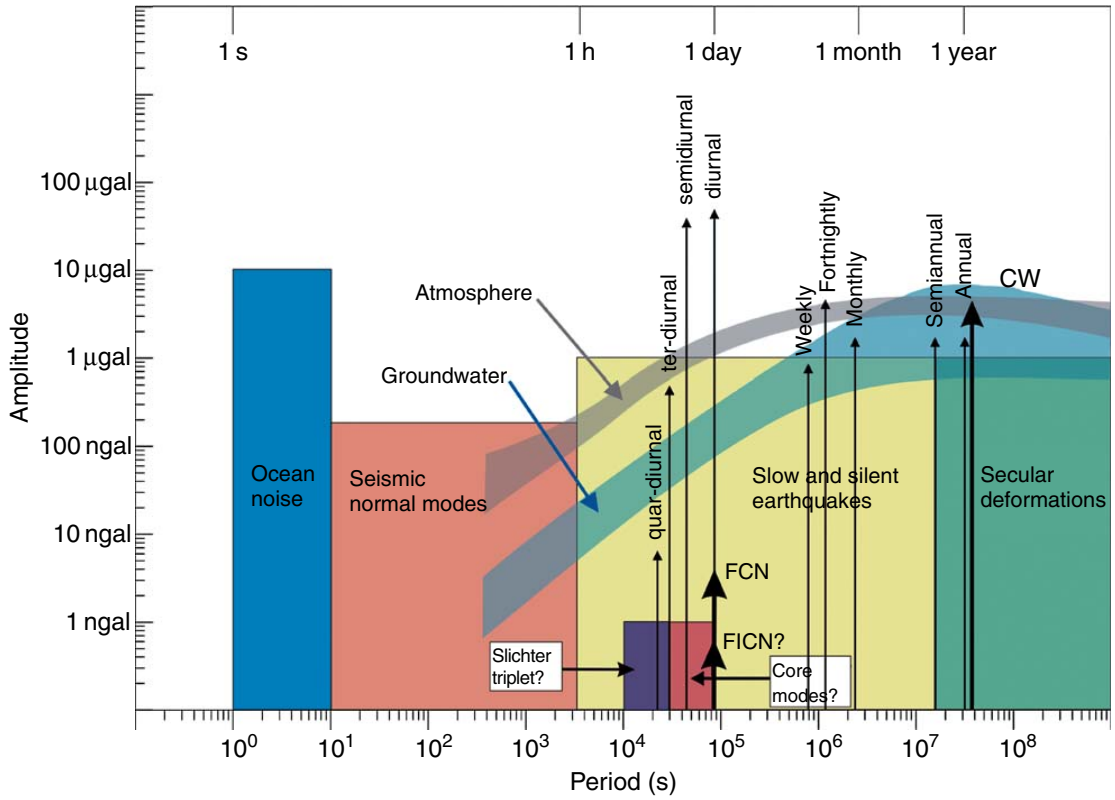

Figure 3.2: Surface gravity effects of geophysical phenomena observable by superconducting-gravimeters after Hinderer et al. (2007). FCN - the free core nutation; wobble modes for an Earth model with a fluid outer core, FCIN - free inner core nutation, CW - Chandler wobble.

```
Filename                :  PE110300.GGS
Station                 :  Pecny, Czech Republic
Instrument              :  GWR OSG-050
Time Delay (sec)        :  8.8600 0.0200 measured
N. Latitude (deg)       :  49.9137 0.0001 measured
E. Longitude (deg)      :  14.7856 0.0001 measured
Elevation MSL (m)       :  534.5800 0.0500 measured
Gravity Cal (µGal/V)    :  -73.3500 0.0200 measured
Pressure Cal (hPa/V)    :  1.0000 0.0060 measured
Author                  :  vojtech.palinkas@pecny.cz
yyyymmdd   hhmmss   gravity(V)   pressure(V)
C**************************************************
77777777            0.0          0.0
20110301   000000   0.313755     962.6310
20110301   000001   0.303011     962.6290
20110301   000002   0.297373     962.6270
20110301   000003   0.303552     962.6220
```

Table 3.2: Gravity and atmospheric-pressure data from the station Pecný sampled at 1 s in a standard PRETERNA format (Wenzel, 1996a).

The amplitude spectra of gravity are strongly affected by the solid-Earth tides. The effect of the atmospheric pressure is the second largest; the groundwater-variation influence is an order of magnitude lesser. The standard procedure to

remove tides from the recorded data is to subtract the theoretical tidal acceleration from the measured gravity. The most accurate tidal-potential catalogue for high-precision work is, according to Wenzel (1996a), HW95 described in Hartmann and Wenzel (1995a and 1995b). However, it is sufficient for our purpose to apply a high-pass Butterworth filter with a threshold of 0.1 mHz to remove local tides from the raw gravity data. In this way we also remove most of the tide-joined hydrological effects. The mean value or linear trend were removed and the data were undersampled from 1 s to 1 min by standard MATLAB procedures. Fig. 3.3 shows the three-week records, both raw and post-processed, of the gravity containing the 2011 Tohoku earthquake on the station Pecný. Although the tidal frequencies are out of our range of interest, it is advisable to remove them from the records when we compare the free-oscillation synthetic and observed SG signals in the time domain.

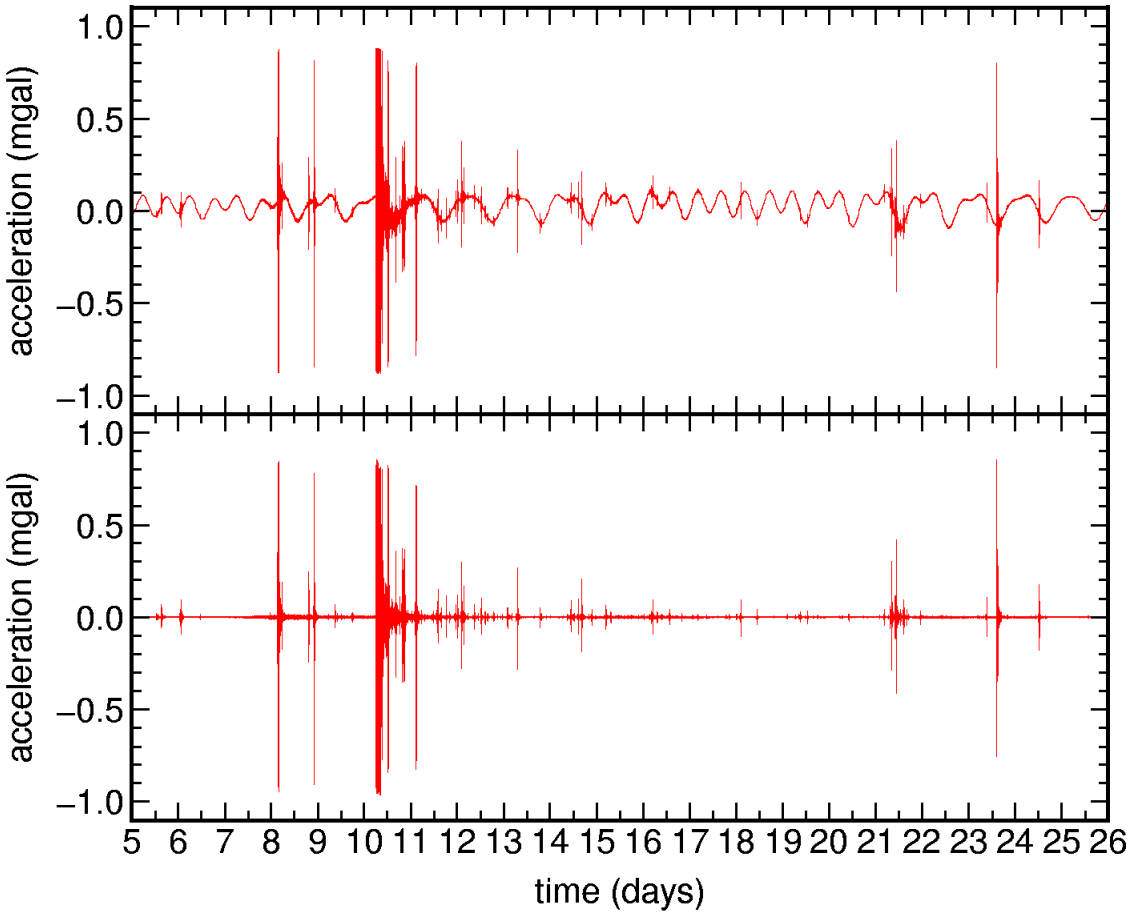

Figure 3.3: Three-week record from station Pecný observed after the 2011 Tohoku earthquake. Raw data are shown on the upper panel, whereas a high-pass Butterworth filter with 0.1 mHz threshold is applied to the data on the lower panel.

According to Hinderer et al. (2007): *The atmosphere provides a significant gravity effect (up to 10% of the tidal signal) with a transfer function (or admittance factor) that approximates -0.3 mGal hPa^{-1} for a typical continental station. The effect is a combination of gravitational attraction by atmospheric density anomalies with a loading that vertically deforms the crust and mantle. For a positive atmospheric density anomaly, simple theory gives about -0.4 mGal hPa^{-1} for the upward attraction and +0.1 mGal hPa^{-1} for the loading. A number of well-studied empirical*

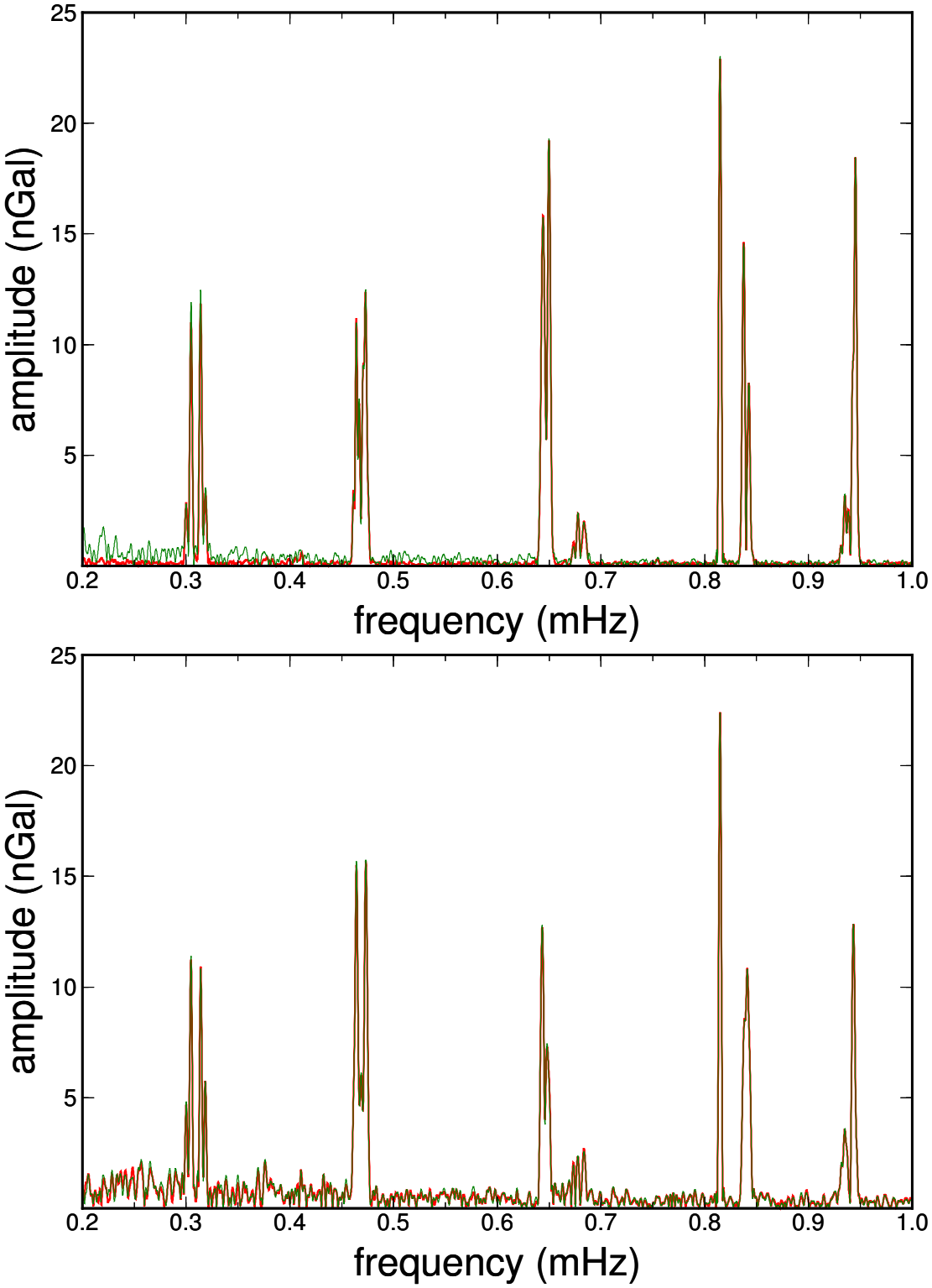

Figure 3.4: Reduction of the noise level due to atmospheric correction on stations Strasbourg (upper panel) and Apache Point (lower panel). Green lines are data without atmospheric correction, and red lines denote the data corrected for the effect of atmospheric pressure where the nominal admittance factor is -3 nm/s^2/hPa. A Hann filter, high-pass Butterworth filter with 0.1 mHz threshold and the Fourier transform were applied to 200-hour time series following the 2011 Tohoku earthquake; the amplitude spectra were averaged over the time window.

and physical methods exist for making a pressure correction to the gravity data, but even with the most sophisticated treatments it is not possible to completely remove the atmospheric pressure effect.

The effect of the atmospheric pressure is demonstrated in Figs. 3.4 and 3.5 where the amplitude spectra of 200-hour signals after the 2011 Tohoku earthquake are shown for the stations Strasbourg and Apache Point. These atmospheric corrections are relevant in the used frequency range only for the stations with high signal-to-noise ratio up to 0.6 mHz, whereas there is no improvement for the stations with higher noise level, regardless of the choice of the admittance factor; in this case the noise is not of atmospheric origin. However, one can clearly see from Fig. 3.5 that the atmospheric corrections do not influence the spectra of the modes ${}_0S_3$, ${}_0S_4$ or ${}_0S_5$, and play only the minor role in the spectrum of the mode ${}_0S_2$.

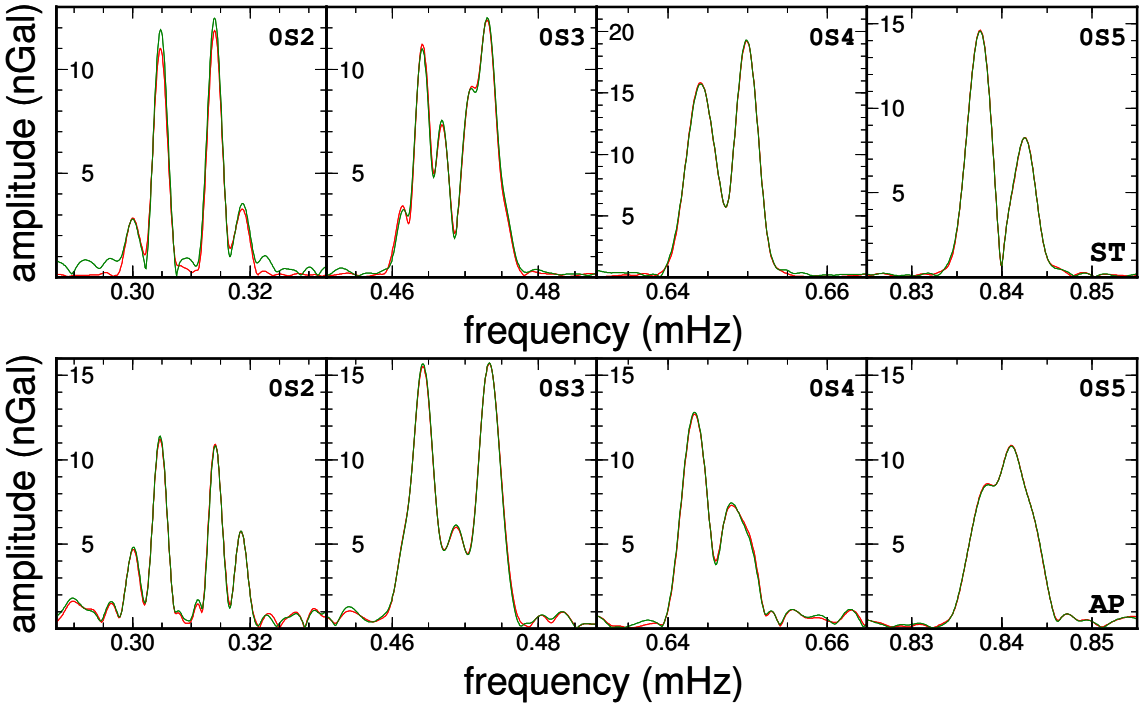

Figure 3.5: Detail of Fig. 3.4 (see caption) for the four longest fundamental spheroidal modes.

3.2 The 2010 Maule and 2011 Tohoku earthquakes

The 1952 Kamchatka, 1960 Valdivia (Great Chilean earthquake), 1964 Alaska and 2004 Sumatra-Andaman earthquakes were the strongest earthquakes in the instrumental era before the full development of the GGP network of superconducting gravimeters. The GGP subsequently registered the following three megaevents: the 2010 Maule, 2011 Tohoku and 2012 Sumatra earthquakes. In this section, we will describe the agency solutions of the 2010 Maule and 2011 Tohoku earthquakes and show the amplitude spectra of the Tohoku SG records as an example. The detailed analysis of these two earthquakes is then the topic of Chapters 4–6; the 2012 Sumatra double event is studied in Section 3.4.

The Global Centroid-Moment-Tensor (GCMT) Project was founded by Adam Dziewonski at Harvard University, and now it is continued by Göran Ekström at the Lamont-Doherty Earth Observatory of Columbia University. We denote the GCMT solutions for the 2010 Maule and 2011 Tohoku earthquakes as PS1[1,2] the U.S. Geological Survey (USGS) solution as PS2[3,4] and the W-phase source solution also provided by USGS as PS3[5,6]. The agency solutions of both earthquakes are summarized in Fig. 3.6 and Tables 3.3 and 3.4.

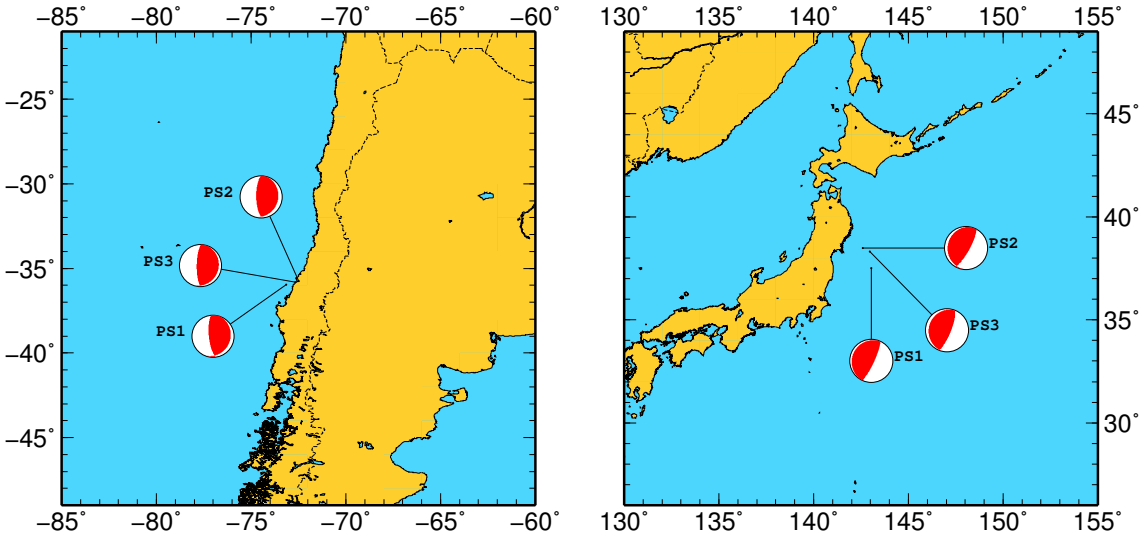

Figure 3.6: Locations and focal mechanisms determined by the different agencies. The exact locations and the moment tensors for both earthquakes are summarized in Tables 3.3 and 3.4.

The GCMTs are calculated by summation of Earth normal modes from long-period data provided by the Global Seismographic Network retrieved in a near-real-time network. The USGS uses principally the same method as the GCMT group. The W-phase source inversion algorithm was specifically developed to handle very large earthquakes like the 2010 Maule and 2011 Tohoku earthquakes. This

[1] http://earthquake.usgs.gov/earthquakes/eqinthenews/2010/us2010tfan/neic_tfan_gcmt.php
[2] http://earthquake.usgs.gov/earthquakes/eqinthenews/2011/usc0001xgp/neic_c0001xgp_gcmt.php
[3] http://earthquake.usgs.gov/earthquakes/eqinthenews/2010/us2010tfan/neic_tfan_cmt.php
[4] http://earthquake.usgs.gov/earthquakes/eqinthenews/2011/usc0001xgp/neic_c0001xgp_cmt.php
[5] http://earthquake.usgs.gov/earthquakes/eqinthenews/2010/us2010tfan/neic_tfan_wmt.php
[6] http://earthquake.usgs.gov/earthquakes/eqinthenews/2011/usc0001xgp/neic_c0001xgp_wmt.php

	latitude	longitude	depth [km]	orig. time	M_0 [10^{22} Nm]
PS1	37.52N	143.05E	20.0	05:47:32.8	5.31
PS2	38.49N	142.60E	10.0	05:47:47.2	4.50
PS3	38.32N	142.97E	24.0	05:46:23.0	3.90

[10^{22} Nm]	M_{rr}	$M_{\theta\theta}$	$M_{\phi\phi}$	$M_{r\theta}$	$M_{r\phi}$	$M_{\theta\phi}$
PS1	1.730	-0.281	-1.450	2.120	4.550	-0.657
PS2	2.03	-0.16	-1.87	2.06	3.49	-0.60
PS3	1.82	-0.13	-1.69	1.34	3.17	-0.56

Table 3.3: The March 11, 2011 Tohoku earthquake agency solutions; Global CMT solution (Nettles et al., 2011) - (PS1), USGS CMT solution (Polet and Thio, 2011) - (PS2), USGS Wphase solution (Duputel et al., 2011) - (PS3).

	latitude	longitude	depth [km]	orig. time	M_0 [10^{22} Nm]
PS1	35.95S	73.15W	24.1	06:35:15.4	1.84
PS2	35.77S	72.47W	30.0	06:35:27.5	1.80
PS3	35.83S	72.67W	35.0	06:34:17.0	2.00

[10^{22} Nm]	M_{rr}	$M_{\theta\theta}$	$M_{\phi\phi}$	$M_{r\theta}$	$M_{r\phi}$	$M_{\theta\phi}$
PS1	1.040	-0.030	-1.010	0.227	-1.510	-0.120
PS2	1.13	-0.06	-1.07	0.09	-1.43	-0.12
PS3	0.93	0.01	-0.94	-0.01	-1.72	-0.15

Table 3.4: The February 27, 2010 Maule earthquake agency solutions; Global CMT solution (Ekström and Nettles, 2010) - (PS1), USGS CMT solution (PS2), USGS Wphase solution (PS3).

method exploits the long period content (200–1000 s) of the broadband seismic record preceding the arrival of the surface waves.

Vertical acceleration amplitude spectra of SG records from stations listed in Table 3.1 are shown in Fig. 3.7 where the Hann filter, high-pass Butterworth filter with 0.1 mHz threshold and the Fourier transform were applied to 50-hour time series following the 2011 Tohoku earthquake. Fig. 3.8 corresponds to the 250-hour time series following the same earthquake. We can clearly see that the amplitude spectra from 50-hour time series have a good quality for most of the stations, except for the station KA, where the record is over-excited because of strong aftershocks; the station CI does not provide good quality record. If the amplitude spectra are calculated from 250-hour record, the signal/noise ratio gets worse for more stations and good quality 450-hour record are provided by only few stations, see Fig 3.9.

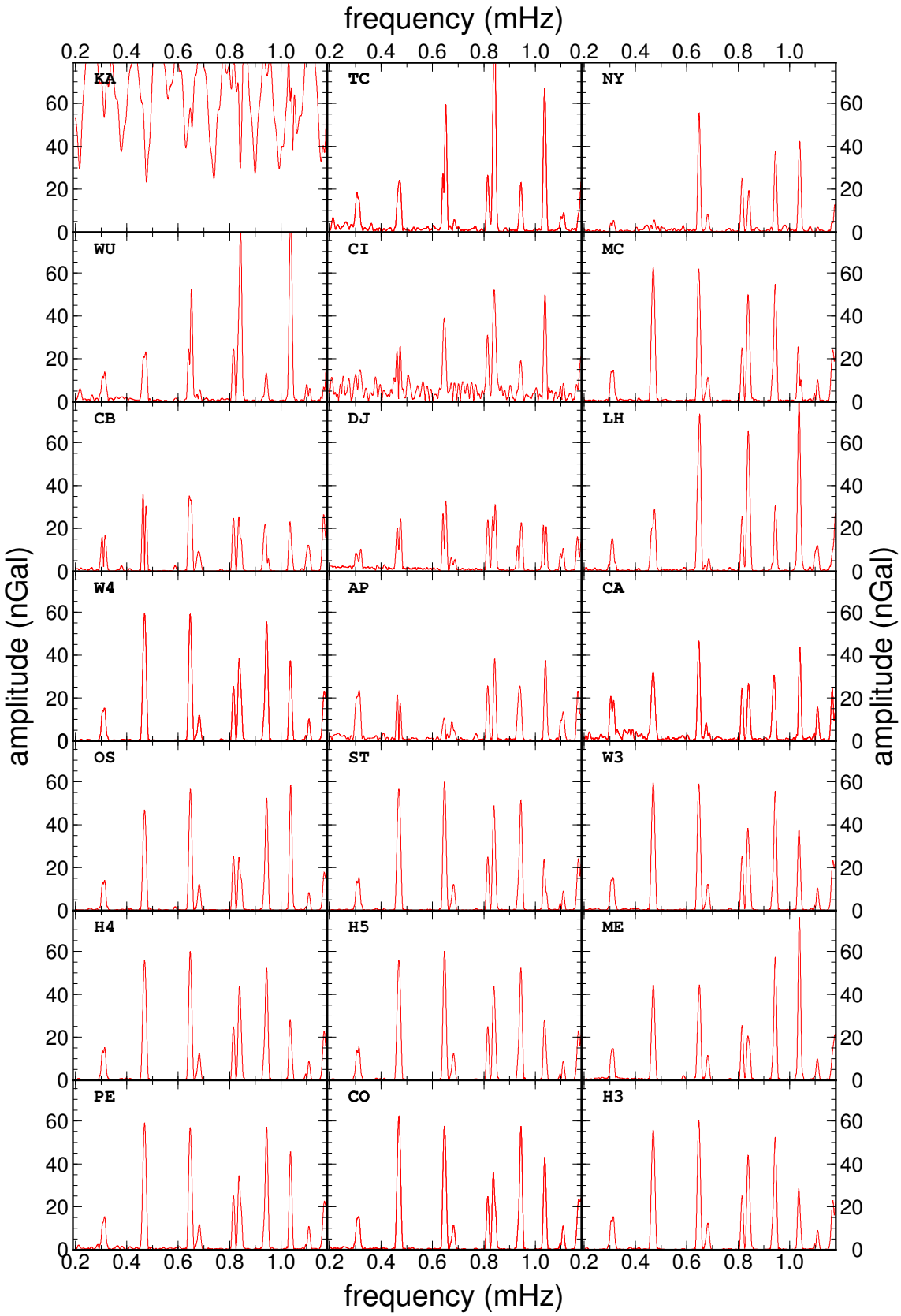

Figure 3.7: Vertical acceleration amplitude spectra of SG records from the stations listed in Table 3.1 after the 2011 Tohoku earthquake. The Hann filter, high-pass Butterworth filter with 0.1 mHz threshold and the Fourier transform were applied to 50-hour time series following the 2011 Tohoku earthquake; the spectra were averaged over the time window.

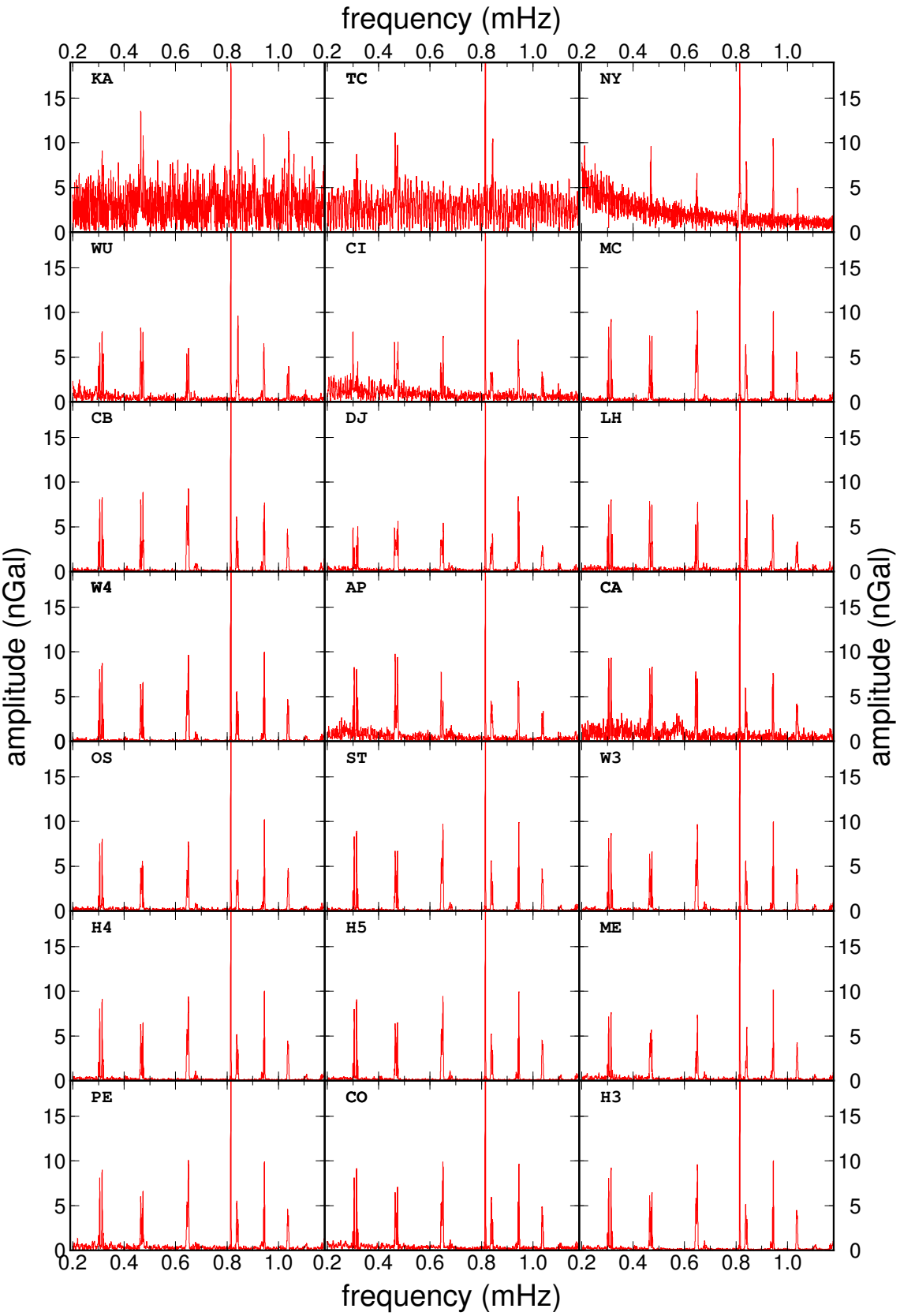

Figure 3.8: Vertical acceleration amplitude spectra of SG records from the stations listed in Table 3.1 after the 2011 Tohoku earthquake. The Hann filter, high-pass Butterworth filter with 0.1 mHz threshold and the Fourier transform were applied to 250-hour time series following the 2011 Tohoku earthquake; the spectra were averaged over the time window. The radial mode ${}_0S_0$ with the frequency 0.815 mHz has the amplitude of about 21.4 nGal.

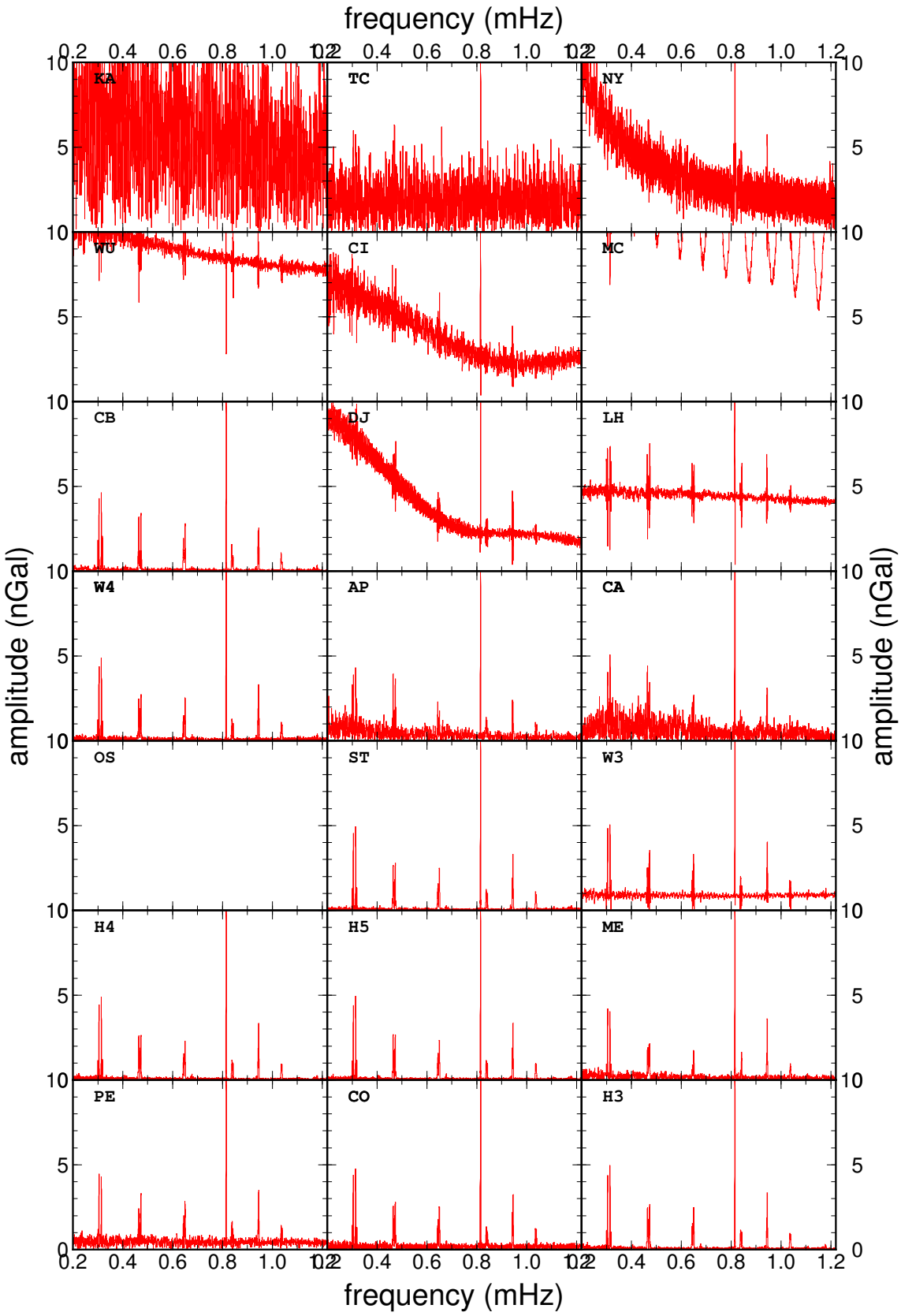

Figure 3.9: Vertical acceleration amplitude spectra of SG records from the stations listed in Table 3.1 after the 2011 Tohoku earthquake. The Hann filter, high-pass Butterworth filter with 0.1 mHz threshold and the Fourier transform were applied to 450-hour time series following the 2011 Tohoku earthquake; the spectra were averaged over the time window. The radial mode ${}_0S_0$ with the frequency 0.815 mHz has the amplitude of about 18.0 nGal.

3.3 Quality factors: data and synthetics

In principal, the modal quality factor Q can be estimated from decrease of the amplitude spectra employing the formula,

$$Q = \frac{\pi f \Delta t}{\ln(A_1/A_2)}, \tag{3.1}$$

where f is the "central" (unperturbed) modal frequency and Δt is the time shift between two time windows of the same length used to calculate spectral amplitudes A_1 and A_2. We define A_1 as

$$A_1 = \int_{\delta f} A(f) df, \tag{3.2}$$

where $A(f)$ is the amplitude spectrum of the signal and δf is a narrow frequency range covering all modal singlets. We can determine the quality factors of the radial modes directly from the data since they are not split. The estimates of Q calculated from the equation (3.1) for fixed $\Delta t = 2$ hours after the 2010 Maule and 2011 Tohoku earthquakes in the case of radial modes is displayed in Figs. 3.10 and 3.11. Horizontal axes correspond to the shift of the first time window after the origin time. Table 3.5 summarizes the lengths of employed time windows, the number of employed station and resulting quality factors. The standard deviations were calculated from the amplitudes obtained from individual station records.

mode	record length [h]	number of records	Q
${}_0S_0$	700/450	11/9	5500 ± 140
${}_1S_0$	250	9/16	2000 ± 80
${}_2S_0$	120	11/17	1120 ± 270

Table 3.5: The lengths of employed time windows (2010 Maule/2011 Tohoku), number of records and found quality factors for three radial modes.

Figs. 3.12–3.14 demonstrate the application of formula (3.1) to (tricky) determination of the quality factors from the amplitude decrease for the modes ${}_0S_2$, ${}_0S_3$, ${}_0S_4$, ${}_0S_5$ and ${}_1S_2$ using synthetic records of different lengths. Since the modal multiplets consist of several singlets with slightly different frequencies, the descent of the spectral amplitudes is very complicated. For this reason the spectral amplitude A_2 was calculated for varying Δt with a 2-hour step and the slope of $\ln(A_1/A_2)$ was estimated by linear regression. The quality factors used for computation of synthetic signals as well as the lengths of the time windows are summarized in Table 3.6.

Note that the line shapes in Figs. 3.12–3.14 depend on the choice of the stations. The simple formula (3.1) is thus, in principle, applicable also to multiplets. However, shifts Δt between the time windows used to calculate the spectral amplitudes A_1 and A_2 have to be very high and problems arise with affecting A_2 by noise. This is the reason why we use (3.1) only for radial modes and estimate the quality factors of the studied spheroidal modes by direct inversion procedure (Chapter 6).

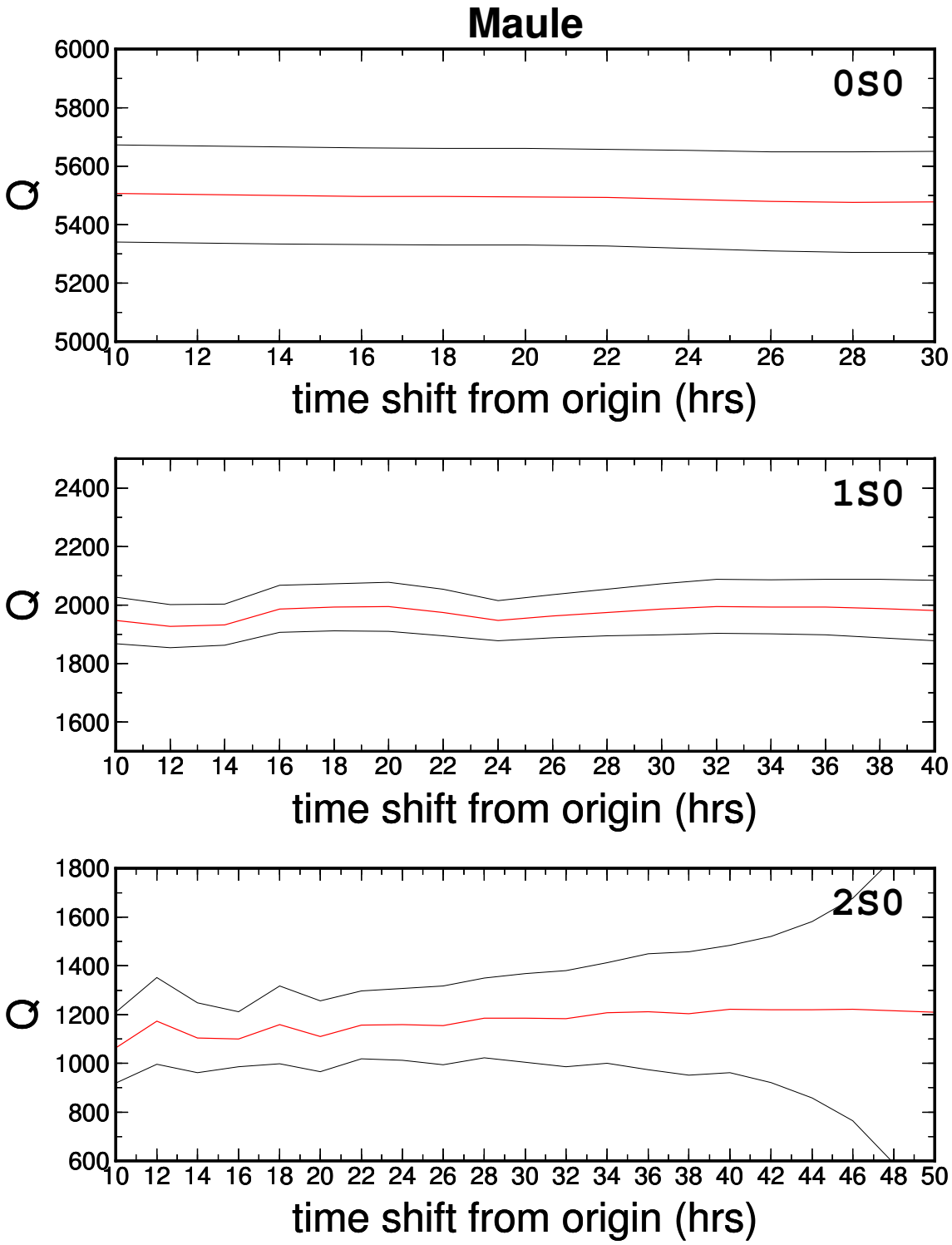

Figure 3.10: Quality factors of the radial modes estimated from the records after the 2010 Maule earthquake from the Fourier amplitude-spectra decrease by means of (3.1). Time difference between the windows $\Delta t = 2$ hours was fixed. Horizontal axis shows time shift of the first window after the origin. Red lines denote Q of the radial modes, whereas black lines represent their standard deviations.

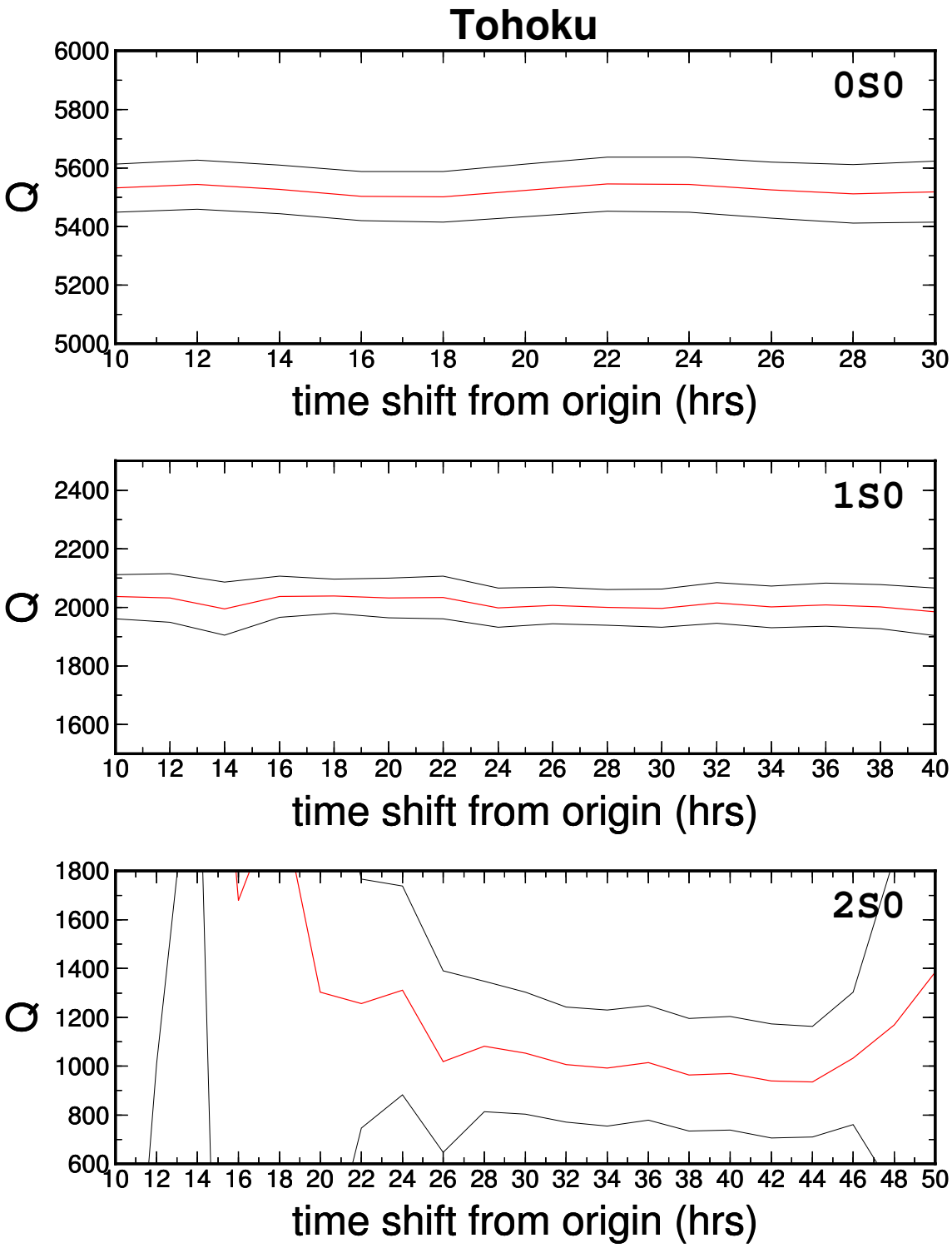

Figure 3.11: Quality factors of the radial modes estimated from the records after the 2011 Tohoku earthquake from the Fourier amplitude-spectra decrease by means of (3.1). Time difference between the windows $\Delta t = 2$ hours was fixed. Horizontal axis shows time shift of the first window after the origin. Red lines denote Q of the radial modes, whereas black lines represent their standard deviations.

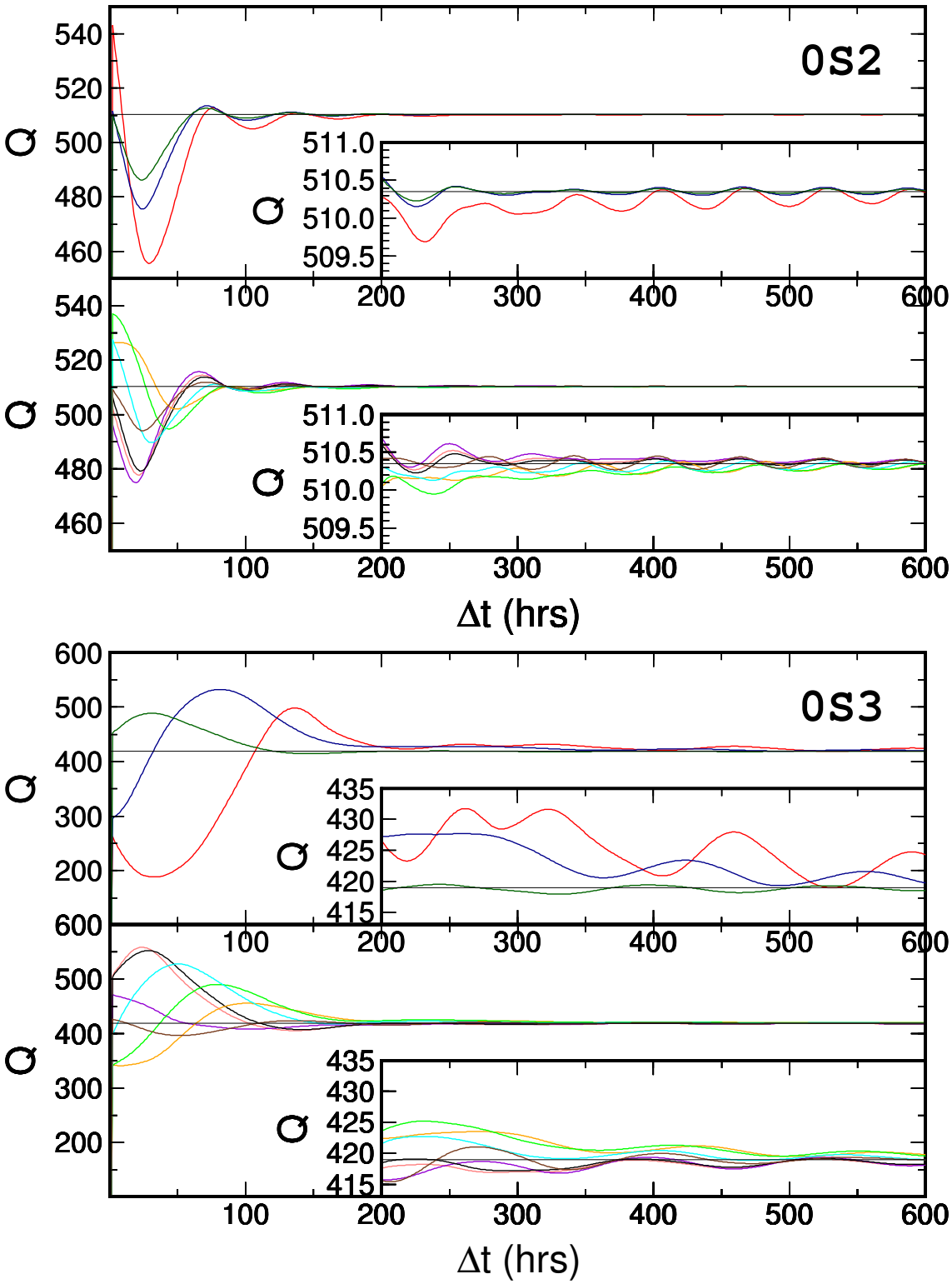

Figure 3.12: The quality factors of the fundamental spheroidal modes ${}_0S_2$ and ${}_0S_3$ derived from the slope of $\ln(A_1/A_2)$. The source was the GCMT solution for the 2011 Tohoku earthquake and synthetics were calculated for 14 stations from Table 3.1. Upper panels show the quality factors derived from the amplitude decrease over all stations; line colors correspond to the length of the synthetic records (red–$Q_0T/2$, blue–Q_0T, green–$2QT$) listed in Table 3.6. Lower panels show the quality factors derived from the amplitude decrease of individual stations for the $2QT$ length of the synthetic records; line colors correspond to stations.

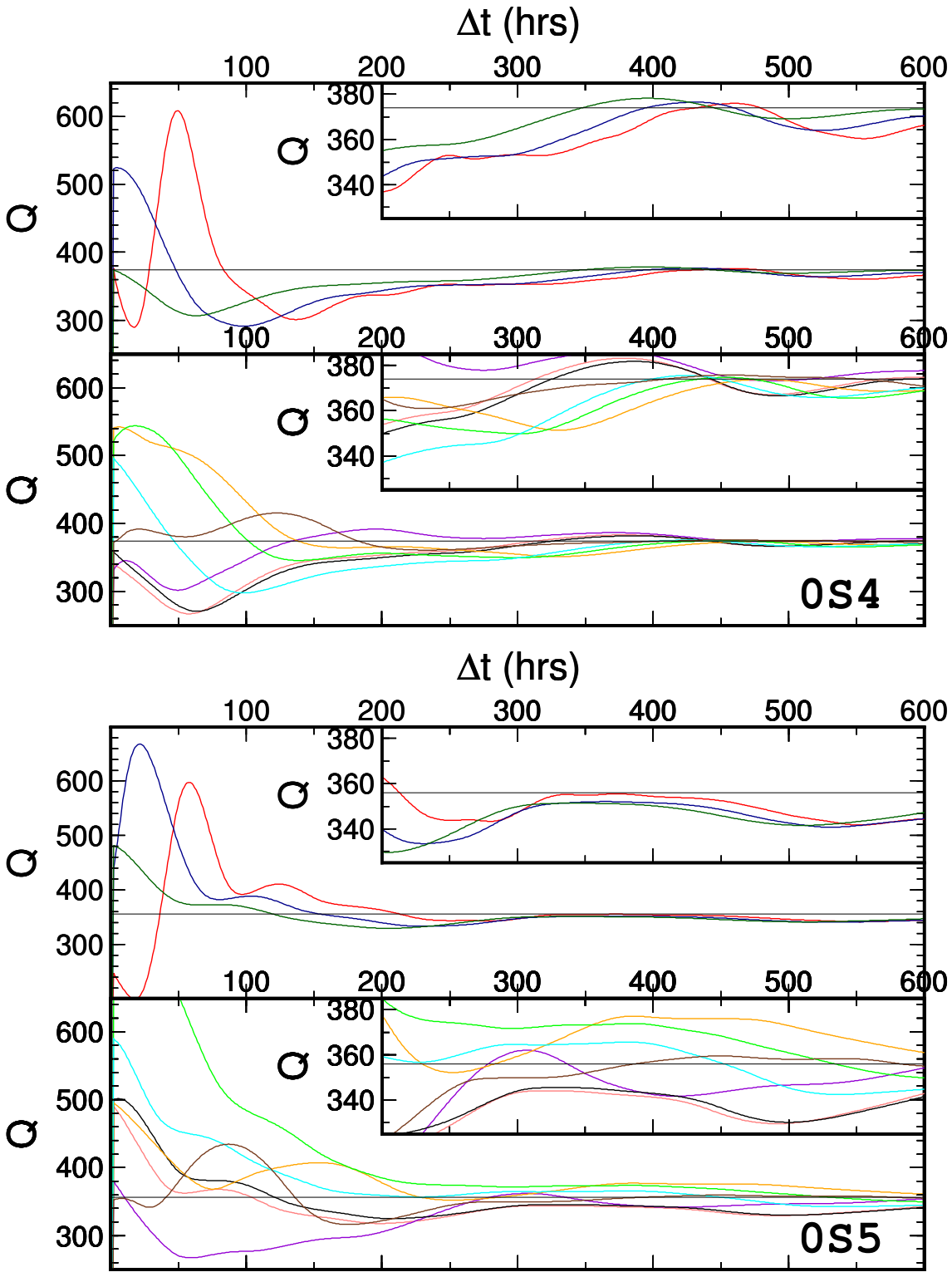

Figure 3.13: Same as Fig. 3.12 but for the modes ${}_0S_4$ and ${}_0S_5$.

mode	record lengths [h]	number of records	Q_0
${}_0S_2$	230/460/920	14	510.35
${}_0S_3$	124/248/500	14	419
${}_0S_4$	80/160/320	14	374
${}_0S_5$	59/118/236	14	356
${}_1S_2$	63/126/252	14	310

Table 3.6: Lengths of employed time windows ($Q_0T/2$, Q_0T, $2Q_0T$), number of the synthetic records and reference quality factors for five spheroidal modes. The source was GCMT solution of the 2011 Tohoku earthquake.

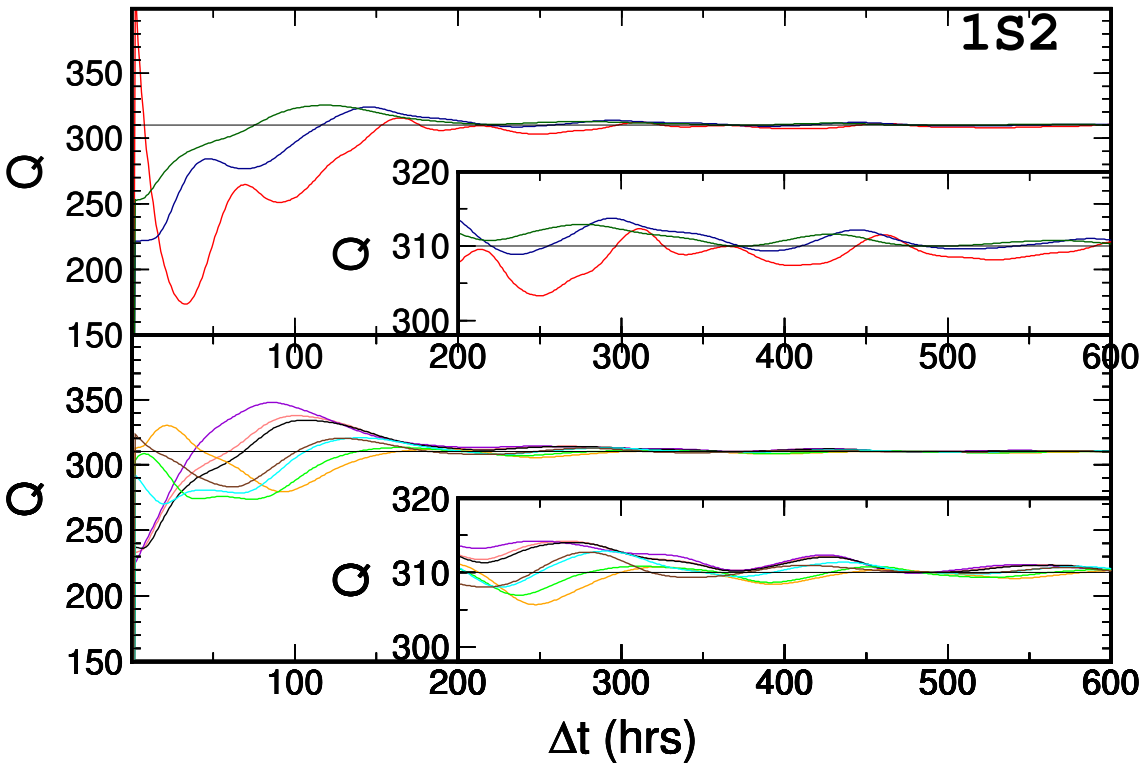

Figure 3.14: The quality factors of the mode ${}_1S_2$ derived from the slope of $\ln(A_1/A_2)$. The source was the GCMT solution for the 2011 Tohoku earthquake and synthetics were calculated for 14 stations from Table 3.1. Upper panels show the quality factors derived from the amplitude decrease over all stations; line colors correspond to the length of the synthetic records (red–$Q_0T/2$, blue–Q_0T, green–$2QT$) listed in Table 3.6. Lower panels show the quality factors derived from the amplitude decrease of individual stations for the $2QT$ length of the synthetic records; line colors correspond to the stations.

3.4 The 2012 Sumatra double earthquake

The two strike-slip earthquakes with moment magnitudes higher than 8 occurred off the west coast of northern Sumatra on a fault within the oceanic lithosphere of the Indo-Australia plate on April 11, 2012. Fig. 3.15 shows the seismicity in the Sumatra-Andaman region in years 1900–2012. Focal mechanisms plotted in this map are the W-phase source solution PS3 provided by USGS. The three standard agency solutions of both earthquakes are summarized in Tables 3.7 (the first event) and 3.8 (the second event), respectively.

	latitude	longitude	depth [km]	orig. time	M_0 [10^{21} Nm]
PS1	2.24N	92.78E	40.0	08:39:29.8	8.96
PS2	2.24N	93.10E	40.0	08:39:32.6	8.50
PS3	2.25N	92.87E	25.0	08:38:38.0	9.00

[10^{22} Nm]	M_{rr}	$M_{\theta\theta}$	$M_{\phi\phi}$	$M_{r\theta}$	$M_{r\phi}$	$M_{\theta\phi}$
PS1	1.36	-5.91	4.55	-3.96	0.46	-6.15
PS2	0.40	-5.39	4.98	1.74	-1.57	-6.31
PS3	1.25	-5.99	4.74	1.34	-0.63	-7.03

Table 3.7: M8.6: April 11, 2012 Sumatra earthquake agency solutions; Global CMT solution (PS1), USGS CMT solution (PS2), USGS Wphase solution (PS3).

	latitude	longitude	depth [km]	orig. time	M_0 [10^{21} Nm]
PS1*	0.76N	92.25E	53.7	10:43:37.4	2.53
PS2*	0.92N	92.49E	43.0	10:43:50.3	2.20
PS3*	0.77N	92.45E	16.0	10:43:09.0	3.90

[10^{22} Nm]	M_{rr}	$M_{\theta\theta}$	$M_{\phi\phi}$	$M_{r\theta}$	$M_{r\phi}$	$M_{\theta\phi}$
PS1*	0.59	-1.67	1.08	-1.08	-0.46	-1.89
PS2*	0.45	-1.30	0.85	0.21	-0.84	-1.63
PS3*	-1.18	0.18	1.00	-0.92	-1.33	-3.38

Table 3.8: M8.2: April 11, 2012 Sumatra earthquake agency solutions; Global CMT solution (PS1*), USGS CMT solution (PS2*), USGS Wphase solution (PS3*).

Since the fundamental radial mode ${}_0S_0$ has its period of about 20.5 minutes and the second event followed 124 minutes after the main shock, there is approximately a zero phase shift between the fundamental radial oscillations generated by these two events. The same applies for the first radial overtone with the period of about 10.22 minutes. The radial modes are generated only by the moment tensor component M_{rr} and depend on the depth of the centroid. We averaged three records from Pecný and Wettzell (two sensors) stations to compare observed and synthetic

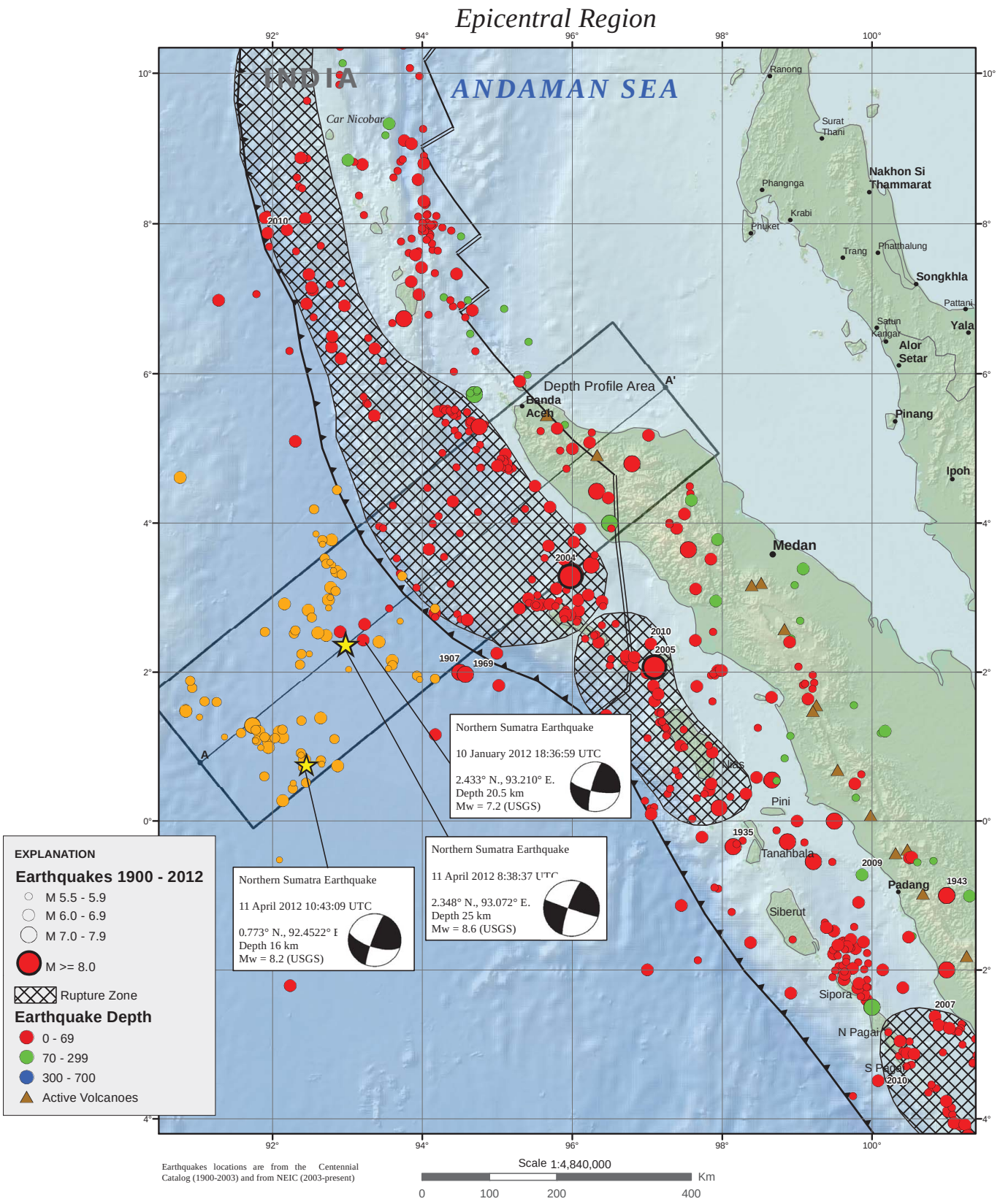

Figure 3.15: Seismicity from USGS Earthquake Summary Map, ftp://hazards.cr.usgs.gov/maps/sigeqs/20120411/20120411.pdf. Focal mechanisms of two main events and one aftershock are the W-phase source solutions provided by USGS.

signals generated by point-source solutions (PS1, PS2 and PS3). Fig. 3.16 shows the vertical acceleration amplitude spectra of these two radial modes. The PS3+PS3* solution generates a too weak signal because M_{rr} components of both events are of opposite sign. The PS2+PS2* solution generates weak signal as well; M_{rr} components are of the same sign, but the M_{rr} value of the main shock is too small. We can thus conclude that only The PS1+PS1* solution yields satisfactory fit with the data. These strike-slip earthquakes generated strong horizontal motions; the M_{rr} components generate approximately 10% of the scalar moment tensor M_0. So, the M_{rr} components are less sensitive than others if the body and surface waves are inverted. However, radial modes are created only by the M_{rr} component and thus they can be used to constrain the M_{rr} components.

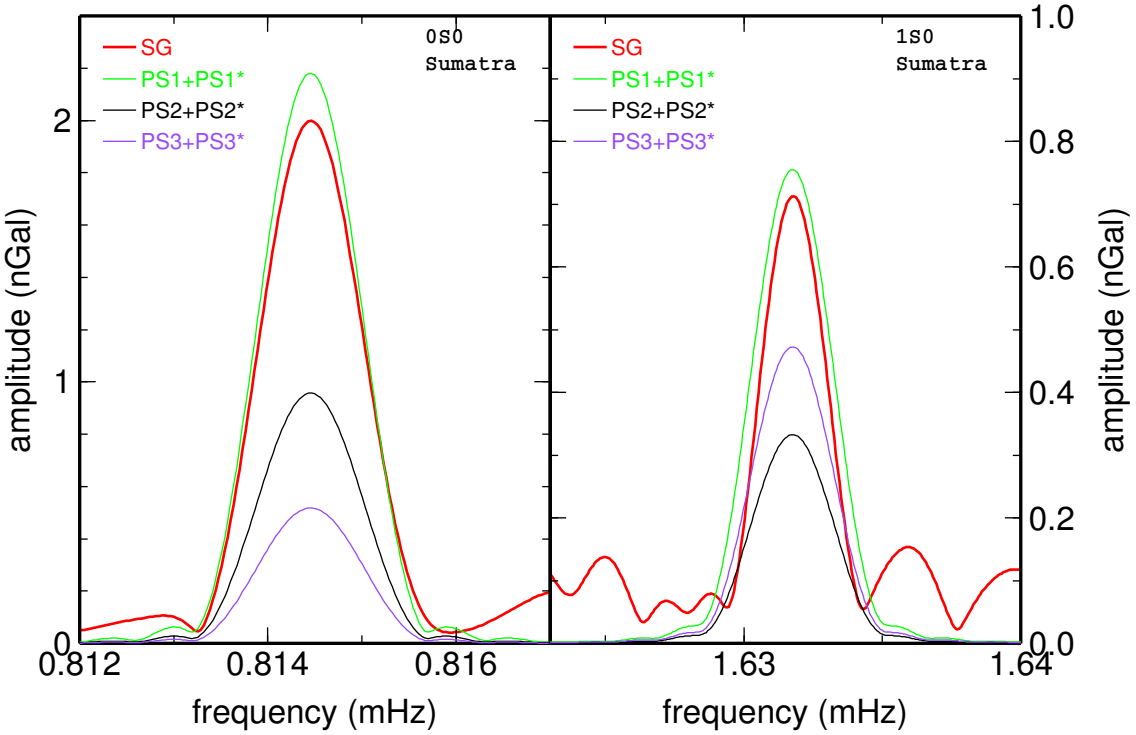

Figure 3.16: Vertical acceleration amplitude spectra of the modes ${}_0S_0$ and ${}_1S_0$ from the SG data (red - average of three records from Pecný and Wettzell stations) and the three synthetics for the agency point-source solutions. A Hann filter and Fourier transform were applied to 450- and 170-hour time series.

The intervals of admissible M_{rr} values for both events are shown in Fig. 3.17. We fixed the origin times and locations on the values given by PS1 for both earthquakes; in principle, we can use any locations or origin times from Tables 3.7 and 3.8 since there is no fundamental influence on our results. We used the quality factors of radial modes determined from data after the 2010 Maule and 2011 Tohoku earthquakes that are presented in Table 3.5 (see Section 3.3) and inverted the averaged records to find M_{rr} components. We may conclude that M_{rr}^* of the second event cannot be negative and M_{rr} of the main event is smaller than 2×10^{21}Nm. Dependence of the constraints on the studied centroid depths is very weak, as expected. We assume the possible interval of the centroid depths 15–50 km (Duputel et al., 2012). The calculations are presented for the depths of 20 and 30 km. This choice represents the optimal variation of amplitudes, since the amplitudes of the radial modes are

sensitive on the shear modulus μ at the centroid depth and our model contains discontinuity at the depth of 22 km (see Figs. 5.2 and 5.3).

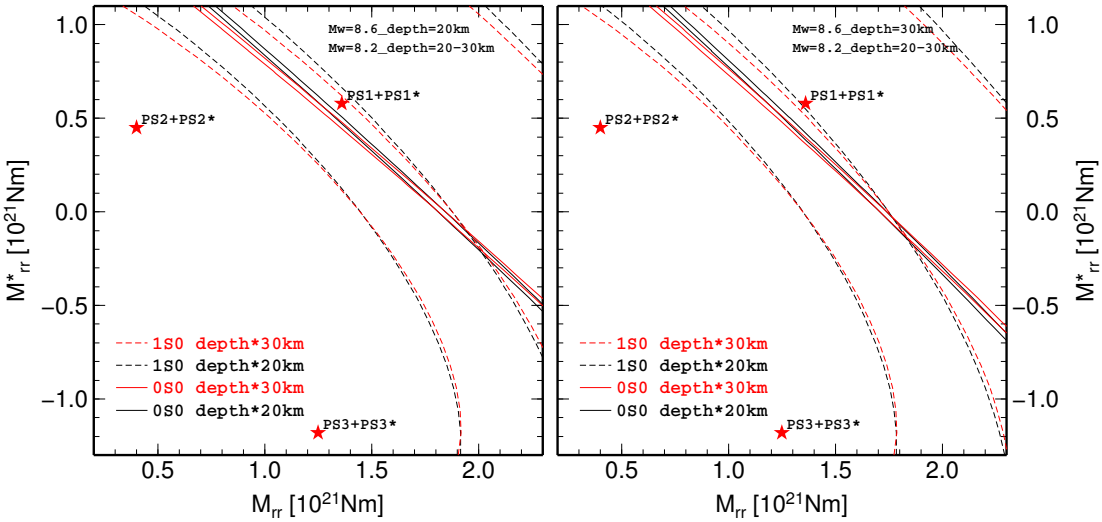

Figure 3.17: Constraints on the M_{rr} components of the 2012 Sumatra double-event (for several depths of the centroids) obtained from the mode ${}_0S_0$ (solid line) and ${}_1S_0$ (dashed line). For each depth, the interval corresponding to $\pm$ one standard deviation of amplitude spectra obtained from the used records and quality factors is drawn. Stars denote published point-source solutions (PS1, PS2 and PS3).

Part II

Seismic source and attenuation studies from SG data

Chapter 4

Tests of the 2011 Tohoku earthquake source models using free-oscillation data from GOPE

Published in Studia Geophysica et Geodaetica,
Volume 56, Issue 2, 585–594, April 2012, doi:10.1007/s11200-011-9033-5

Eliška Zábranová[1,2], Ctirad Matyska[1] and Ladislav Hanyk[1]

[1]Department of Geophysics, Faculty of Mathematics and Physics, Charles University in Prague, V Holešovičkách 2, CZ-18000, Prague, Czech Republic
[2]Research Institute of Geodesy, Topography and Cartography, Zdiby, Czech Republic

Abstract

Data from a superconducting gravimeter were obtained from the Geodetic Observatory Pecný (GOPE), Czech Republic, and compared with acceleration data from a broadband seismometer at the same location. We calculated synthetic seismograms for several point- and finite-source fast solutions of the 2011 Tohoku earthquake obtained from surface waves and tested them only against the observed gravity data because of high-noise levels in the low-frequency seismic data. We have obtained a good fit of the synthetic amplitude spectrum with the data up to 1.7 mHz without an additional increase of the moment magnitude. In this aspect, the 2011 Tohoku earthquake was similar to the 2010 Maule earthquake and not to the 2004 Sumatra-Andaman earthquake, where the free-oscillations studies resulted in an increase of the early M_w values. The degree-one mode ${}_3S_1$ dominates the ${}_3S_1$-${}_2S_2$-${}_1S_3$ triplet at the GOPE station.

Keywords: Free oscillations of the 2011 Tohoku earthquake, superconducting-gravimeter data, source solutions

4.1 Motivation

The March 11, 2011, Tohoku earthquake together with the 2004 Sumatra-Andaman and the 2010 Maule are the three largest earthquakes recorded during the last decade. Such extraordinary events generate clear signals with a broad frequency content that are strong enough for both detailed structural studies associated with the eigenfrequencies of the Earth and source studies based on modal amplitude analysis (*Park et al., 2005; Okal and Stein, 2009*). Because of the complexity of the source region of such events (*Ammon et al., 2005*) their moment magnitude M_w estimates are subject to substantial uncertainty (e.g., *Kanamori, 2006*). The aim of this study is to test several published fast source solutions of the 2011 Tohoku earthquake in the low-frequency range up to 1.7 mHz using data from a superconducting gravimeter at the Geodetic Observatory Pecný (GOPE) (49.9° N, 14.8° E) in the epicentral distance of 81°.

4.2 Gravity and seismic data

The superconducting gravimeter (SG) OSG-050 with the sampling frequency of 1 Hz was installed at the GOPE station in February 2007. The new instrumentation allows the study of a number of geodynamic phenomena towards both the higher frequencies (i.e., free oscillations, long-period seismic waves) and the lower frequencies (e.g., environmental effects, long-period tides). In May 2009 the broadband seismometer (BB) CMG-3TD was installed in a new steel-cased, 60-m deep borehole in the immediate vicinity of the gravimeter. The main characteristics of the BB include 360 s to 50 Hz flat frequency response and the high-stability variant with low self-noise up to 400 s. We have used this collocation of two modern instruments to calculate and compare amplitude spectra of the records from both instruments. Data from the SG were corrected for tides and pressure variations (*Hinderer et al., 2007*). Furthermore, the mean value and linear trend have been removed to eliminate the instrumental drift and residual tidal and air pressure signals. The mass channel of the BB, that directly yields vertical acceleration of the instrument, was used, and the same detrend procedure was applied to the seismic data.

Fig. 4.1 shows the amplitude spectra of the Tohoku earthquake for 68-hour long records (two upper panels) and 137-hour long records (two bottom panels), respectively, at the GOPE station from both the SG (red line) and the vertical acceleration of the BB (blue line) obtained from the time window starting at March 11, 9:00 UTC. The first panel shows the Fourier amplitude spectrum averaged by the length of the time window, whereas the second panel exhibits the same quantity after applying the Hann filter in the time domain; the same Fourier amplitude spectra obtained for the longer time series are demonstrated in the third and the fourth panels. The application of the Hann filter focuses spectral peaks but, on the other hand, it enhances a relative level of the low-frequency BB noise, because the BB signal of the longest free oscillations is above the noise level only at the beginning of the time series. A substantial increase of the BB noise is thus clearly visible, if the longer time series is employed for spectral analysis. To avoid the problems with the noise at the studied frequency range, we will compare synthetic calculations with the SG signal only, and the data from the BB are shown just to demonstrate a very good mutual agreement of spectral peaks measured by both instruments. The situation

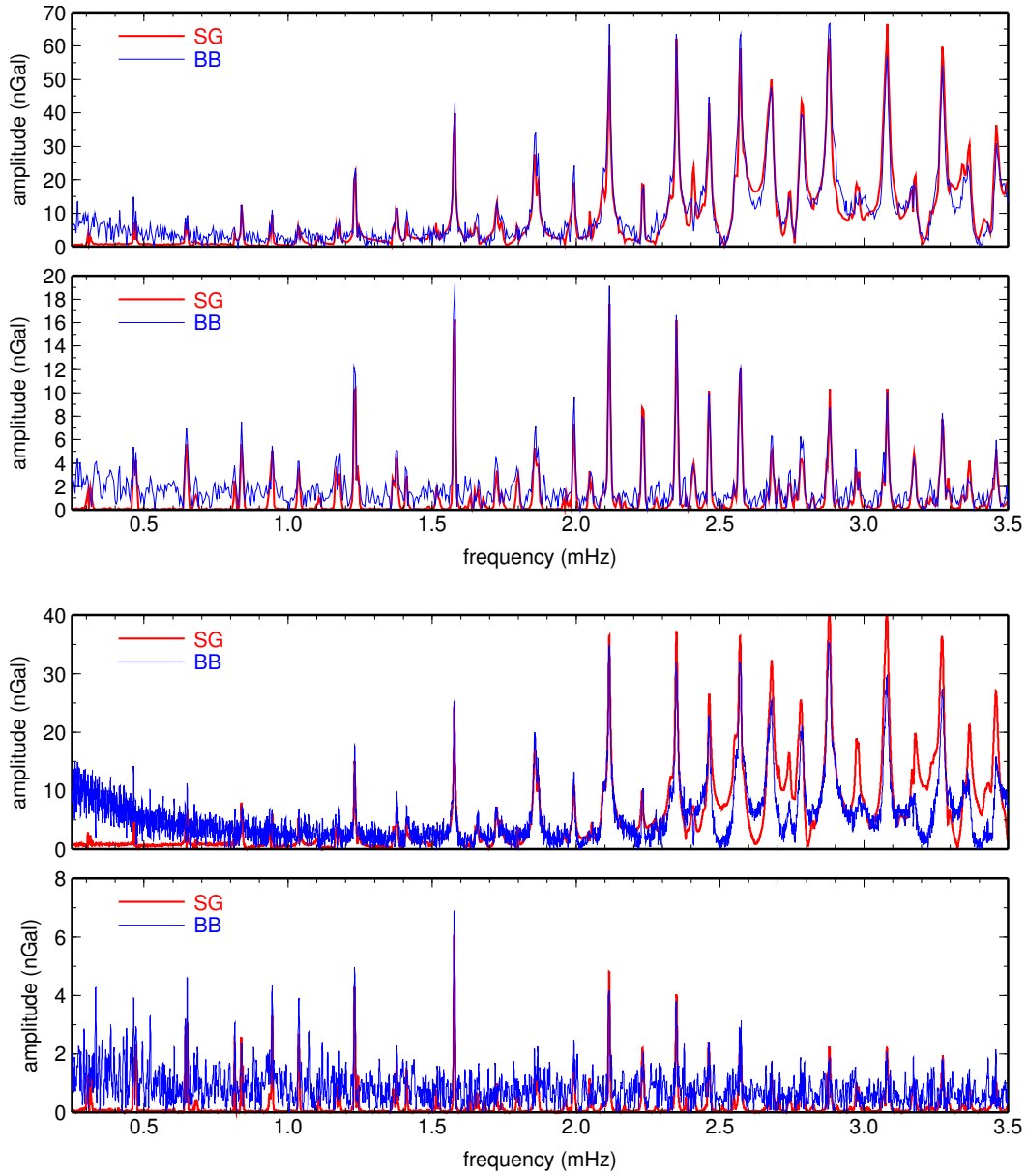

Figure 4.1: Vertical acceleration amplitude spectra of the superconducting gravimeter (red line) and the broadband seismometer (blue line) after the March 11, 2011, Tohoku earthquake. The Fourier transform was applied to 68- and 137-hour time series (upper two and bottom two panels, respectively) and the spectrum was averaged over the time window. In the second and the fourth panels the Hann filter was applied before the Fourier transform.

at the GOPE station is a good example of the fact that present low-frequency seismology needs supplementary instruments to broadband seismometers; more detailed discussion is in, e.g., *Ferreira et al. (2006)*.

4.3 Synthetic calculations

When spherical harmonic analysis is employed, the equations describing the free oscillations can be written as a system of boundary-value problems for second-order ordinary differential equations. The standard methodology developed for these

eigenvalue problems is based on numerical integration of a characteristic equation. The solution of this equation can be numerically problematic, especially when close frequencies need to be separated and/or the skin effect of the eigenfunctions is significant. Our research team has been developing a novel numerical approach, where high-accuracy pseudospectral schemes (*Fornberg, 1996*) are applied to discretize the equations in radial direction. In such a way, either a matrix eigenvalue problem (in the case of free oscillations) or a system of linear equations (in the case of tidal deformations) is obtained; the main idea of this approach is explained in the Appendix and details can be found in *Zábranová et al. (2009)*. Using numerical libraries for matrix spectral analysis, the eigenfunctions and eigenfrequencies of the fundamental modes are obtained simultaneously. Our calculations of the eigenproblem were performed for the 1-D PREM parameters (*Dziewonski and Anderson, 1981*) evaluated at the fixed frequency of 1.25 mHz. We also evaluated first-order frequency perturbations of individual modes using Rayleigh's principle and considering a complex perturbation of the isotropic elastic parameters (e.g., *Dahlen and Tromp, 1998*) to obtain the results for the frequency-dependent PREM model.

Moreover, multiplet splitting due to the Coriolis and centrifugal forces and hydrostatic ellipticity were also included following the approach by *Woodhouse and Dahlen (1978)* and *Dahlen and Sailor (1979)*. Note that 1-D structural approximations are still standard tools in low-frequency sources studies (e.g., *Kanamori and Rivera, 2008*). The source and the attenuation have been incorporated into our calculations by means of the formulas of *Dahlen and Tromp (1998)*.

4.4 Results

Fig. 4.2 demonstrates the comparisons of the three point-source (PS) and two finite-source (FS) solutions with the SG data. The first source PS1 ($M_w = 9.09$, depth 20 km) is by *Ekström* [1], see also *Nettles et al. (2011)*, the second solution PS2 ($M_w = 9.04$, depth 10 km) is the *USGS Centroid Moment Tensor Solution* [2] and the third model PS3 ($M_w = 9.00$, depth 24 km) is the *USGS WPhase Moment Solution* [3]. The source model FS1, constructed by *Wei and Sladen* [4], consists of 252 point sub-sources and its total seismic scalar moment is $M_0 = 5.39 \times 10^{22}$ Nm, which corresponds to $M_w = 9.09$. The last model FS2 is by *Shao et al.* [5]. It consists of 37050 sub-sources with $M_0 = 5.75 \times 10^{22}$ Nm, which corresponds to slightly higher $M_w = 9.11$.

It is of interest that the PS2 source model clearly yields the strongest synthetic signal for the most of the modes although the moment magnitude M_w of all the source models except PS3 are higher. The reason is that its rake (slip) of 68° is rather anomalous in comparison with the other models. A detailed analysis of individual mode spectra is in Fig. 4.3, where the data and five synthetic calculations are shown. Moreover, the frequencies of the degenerate multiplets calculated by our code as well as by the Mineos software package (*Masters, 2010*) for the PREM model are written in the panels; the agreement between these two approaches is very good. Individual modes ${}_0S_0$, ${}_0S_2$, ${}_0S_3$, ${}_0S_4$, ${}_0S_5$, ${}_0S_6$, ${}_0S_7$ and ${}_0S_9$, that are clearly separated in the spectrum, are captured by synthetic calculations very well.

The frequencies close to 0.95 mHz, where the mode triplet ${}_3S_1$-${}_2S_2$-${}_1S_3$ occurs, require a special attention, see Fig. 4.4. The coupling of the modes slightly influences the frequencies (*Zürn et al., 2000*) but we have not incorporated this effect into this

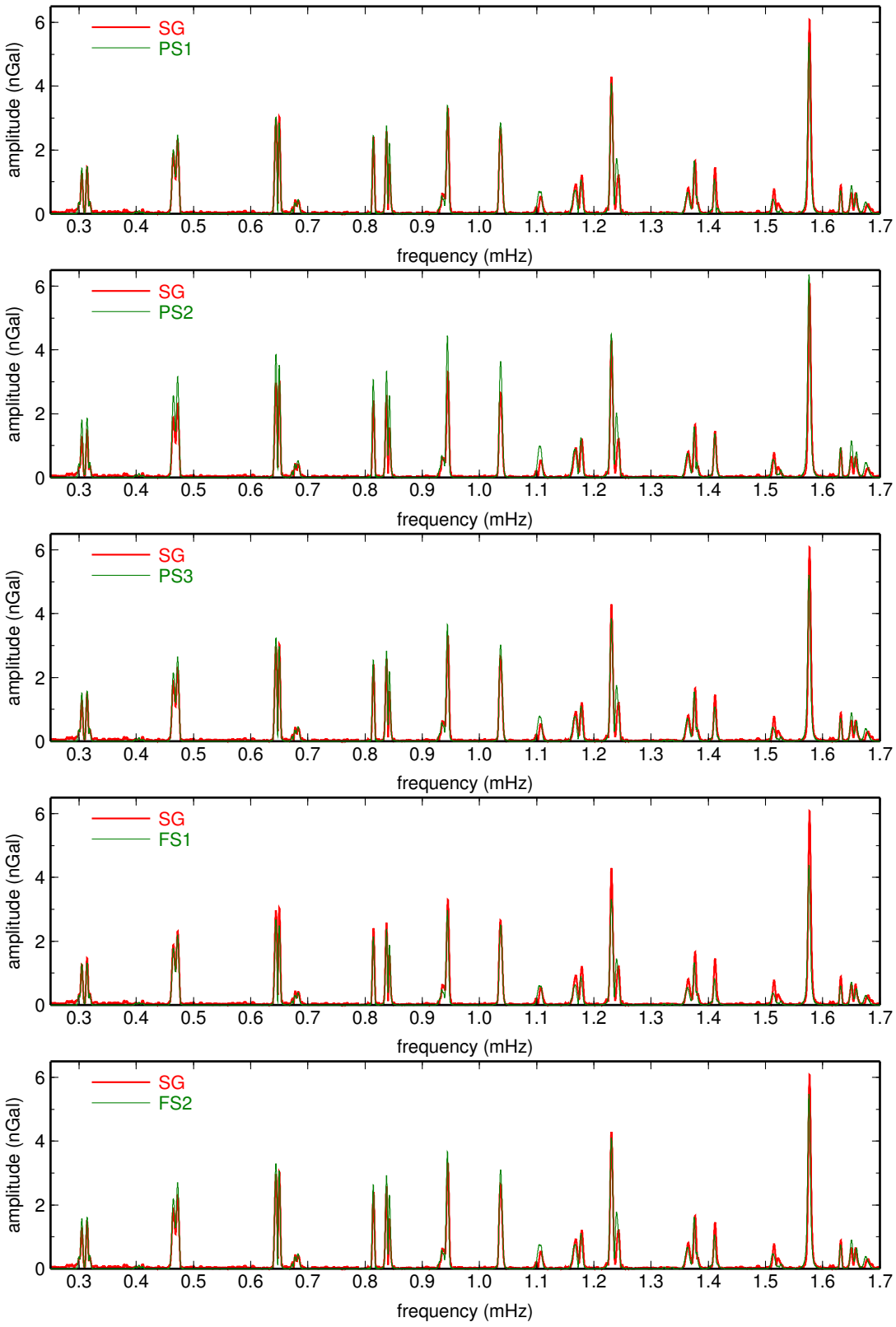

Figure 4.2: Vertical acceleration amplitude spectra after the March 11, 2011, Tohoku earthquake. Red lines - superconducting gravimeter, green lines - synthetic calculations for the five fast source solutions [1]–[5]. The Hann filter and the Fourier transform were applied to 137-hour time series.

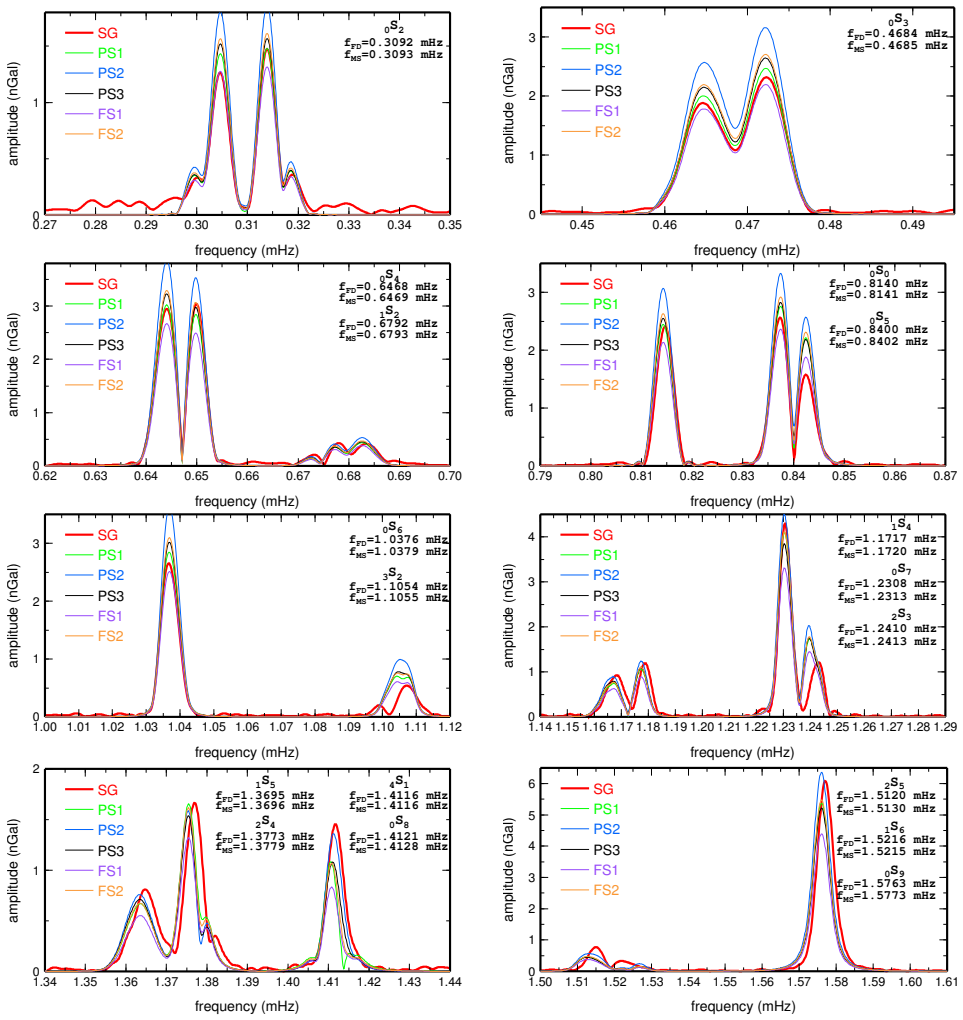

Figure 4.3: Vertical acceleration amplitude spectra of fundamental modes after the March 11, 2011, Tohoku earthquake calculated for the three point sources PS1, PS2, PS3 and two finite sources FS1 and FS2 and compared to the observed SG signal. The symbols f_{FD} and f_{MS} denote the unperturbed eigenfrequencies of the spherical PREM model calculated by means of our finite-difference approach and by the MINEOS software package (*Masters, 2010*), respectively. The Hann filter and the Fourier transform were applied to 137-hour time series.

study. Further details about the mode coupling can be found in, e.g., *Dahlen and Tromp (1998)* and *Widmer-Schnidrig and Laske (2007)*. The mode $_2S_2$ is very weak and can be ignored, similarly to the oscillations studied in *Okal and Stein (2009)*. This is the reason why it is not shown in Fig. 4.4. The calculated amplitude spectrum of the mode $_1S_3$ fits well the data peak at 0.935 mHz, which is caused by the splitting of this mode. However, it strongly underestimates the observed main peak of data at 0.945 mHz. Such a difference can easily be explained by a signal from the mode $_3S_1$, that clearly plays a dominant role in this triplet.

In order to evaluate quantitatively the fit of particular modes, we integrated their amplitude spectra over the frequency bands, where synthetic signals of individual modes are effectively non-zero. A relative fit to the data is summarized in Table 4.1. No source model can be preferred for all the modes but the total power of the studied modes is best fit by the point-source models PS1 and PS3, the geometries of which

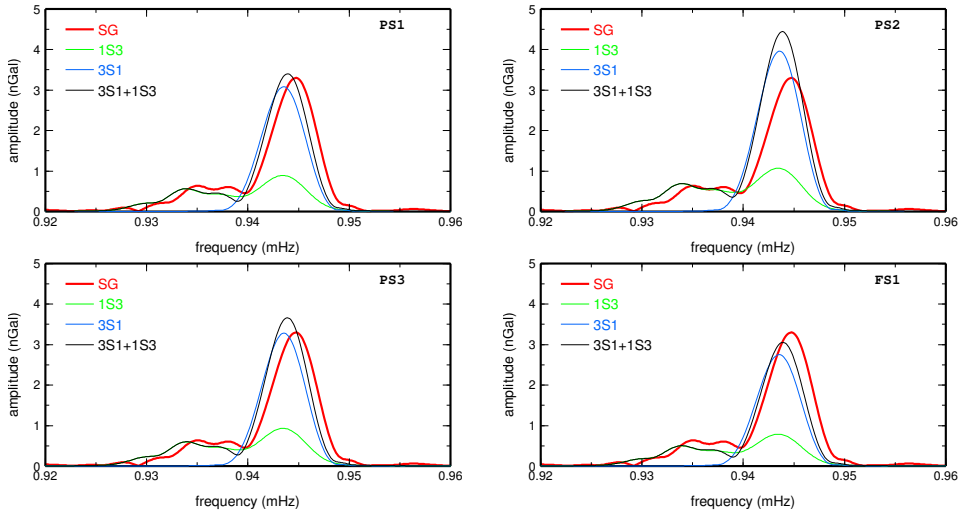

Figure 4.4: Vertical acceleration amplitude spectrum of the triplet ${}_3S_1$-${}_2S_2$-${}_1S_3$ after the March 11, 2011, Tohoku earthquake calculated for the three point sources PS1, PS2, PS3 and the finite source FS1 and compared to the observed SG signal. The synthetic spectrum of the mode ${}_2S_2$ is two orders of magnitude smaller and, therefore, not shown here. The Hann filter and the Fourier transform were applied to 137-hour time series.

source model	${}_0S_0$	${}_0S_2$	${}_0S_3$	${}_0S_4$	${}_0S_5$	${}_0S_6$	${}_0S_7$	${}_0S_9$	total
PS1	0.987	0.951	0.952	0.962	0.839	0.920	0.993	0.923	0.988
PS2	0.729	0.683	0.662	0.792	0.597	0.668	0.882	0.908	0.767
PS3	0.945	0.893	0.879	0.984	0.815	0.889	0.945	0.897	0.969
FS1	0.885	0.933	0.932	0.845	0.999	0.936	0.814	0.755	0.867
FS2	0.911	0.857	0.852	0.960	0.769	0.847	0.991	0.940	0.929

Table 4.1: The relative agreement between the synthetic calculations and the data for the fundamental clearly isolated modes defined by $1 - \left|\int_{\delta f} A_g \mathrm{d}f - \int_{\delta f} A_m \mathrm{d}f\right| / \int_{\delta f} A_g \mathrm{d}f$, where A_m is the amplitude spectrum of models, A_g is the amplitude spectrum of the gravity data and δf is the frequency width of the mode. The last column shows the relative fit after integration over all eight chosen modes.

are very similar but whose magnitudes slightly differ. Nevertheless, the finite source FS1 yields a satisfactory fit for the modes ${}_0S_2$, ${}_0S_3$, ${}_0S_5$, ${}_0S_6$ and the finite source FS2 produces a good fit to the modes ${}_0S_4$, ${}_0S_7$ and ${}_0S_9$. Therefore, one can hardly prefer any of the two solution groups.

4.5 Concluding remark

Employing the data from the superconducting gravimeter installed at the GOPE station, we have demonstrated that, in general, the studied 2011 Tohoku earthquake source models obtained from surface waves generate synthetic signals that are in a good agreement with the observed data. Whereas analysis of longest-period normal-mode data of the 2004 Sumatra-Andaman earthquake resulted in an increase of the early M_w values (*Okal and Stein, 2009*), now the M_w estimates seem to be satisfactory. In this aspect, the 2011 Tohoku earthquake is similar to the 2010 Maule

earthquake (*Okal, EGU General Assembly, Vienna 2011*). Note that a strong signal of the degree-one mode ${}_3S_1$ is clearly observed in the ${}_3S_1$-${}_2S_2$-${}_1S_3$ triplet.

Acknowledgments

We thank M. Vaľko, V. Pálinkáš and V. Plicka for providing us with the data, F. Gallovič for his help with data processing, J. Zahradník and D. A. Yuen for discussion and substantial encouragement, O. Šrámek, J. Velímský and P. Maierová for technical help and anonymous reviewers for their constructive comments and suggestions. This research has been supported by the Grant Agency of the Charles University under the projects No. 2010-141610 and No. 2012-265308 and by the research project MSM 0021620860 of the Czech Ministry of Education.

References

Ammon C.J., Ji C., Thio H-K., Robinson D., Ni S., Hjorleifsdottir V., Kanamori H., Lay T., Das S., Helmberger D., Ichinose G., Polet J. and Wald D., 2005. Rupture process of the 2004 Sumatra-Andaman earthquake, *Science*, **308**, 1133–1139.

Dahlen F.A. and Tromp J., 1998. *Theoretical Global Seismology*, Princeton University Press, Princeton.

Dahlen F.A. and Sailor R.V., 1979. Rotational and elliptical splitting of the free oscillations of the Earth, *Geophys. J. R. astr. Soc.*, **58**, 609–623.

Dziewonski A.M. and Anderson D.L., 1981. Preliminary reference Earth model, *Phys. Earth Planet. Inter.*, **25**, 297–356.

Ferreira A.M.G., d'Oreye N.F., Woodhouse J.H. and Zürn W., 2006. Comparison of fluid tiltmeter data with long-period seismograms: Surface waves and Earth's free oscillations, *J. Geophys. Res.*, **111**, B11307.

Fornberg B., 1996. *A Practical Guide to Pseudospectral Methods*, Cambridge University Press, New York.

Hinderer J., Crossley D. and Warburton R.J., 2007. Gravimetric Methods – Superconducting Gravity Meters, in *Treatise on Geophysics, Volume 3 Geodesy*, Ed. by Herring T., Elsevier, pp. 66–122.

Kanamori H., 2006. Lessons from the 2004 Sumatra-Andaman earthquake, *Phil. Trans. R. Soc. A*, **364**, 1927–1945.

Kanamori H. and Rivera L., 2008. Source inversion of Wphase: speeding up seismic tsunami warning. *Geophys. J. Int.*, **175**, 222–238.

Masters G., 2010. *Mineos Package* (geodynamics.org/cig/software/mineos).

Nettles M., Ekström G. and Koss H.C., 2011. Centroid-moment-tensor analysis of the 2011 off the Pacific coast of Tohoku Earthquake and its larger foreshocks and aftershocks, *Earth Planets Space*, **63**, 519–523.

Okal E.A. and Stein S., 2009. Observations of ultra-long period normal modes from the 2004 Sumatra-Andaman earthquake, *Phys. Earth Planet. Int.*, **175**, 53–62.

Park J., Song T.-R.A., Tromp J., Okal E., Stein S., Roult G., Clevede E., Laske G., Kanamori H., Davis P., Berger J., Braitenberg C., van Camp M., Lei X., Sun H., Xu H. and Rosat S., 2005. Earth's free oscillations excited by the 26 December 2004 Sumatra-Andaman earthquake, *Science*, **308**, 1139–1144.

Widmer-Schnidrig R. and Laske G., 2007. Theory and Observations – Normal Modes and Surface Wave Measurements, in *Treatise on Geophysics, Volume 1 Seis-*

mology and the Structure of the Earth, Ed. by Romanowicz B.A. and Dziewonski A.M., Elsevier, pp. 67–125.

Woodhouse J.H. and Dahlen F.A., 1978. The effect of a general aspherical perturbation on the free oscillations of the Earth, *Geophys. J. R. astr. Soc.*, **53**, 335–354.

Zábranová E., Hanyk L. and Matyska C., 2009. Matrix pseudospectral method for elastic tides modeling, in *Mission and Passion: Science, A volume dedicated to Milan Burša on the occasion of his 80th birthday*, Ed. by Holota P., Published by the Czech National Committee of Geodesy and Geophysics, Prague, pp. 243–260 (geo.mff.cuni.cz/documents/2009-Zabranova.pdf).

Zürn W., Laske G., Widmer-Schnidrig R. and Gilbert F., 2000. Observation of Coriolis coupled modes below 1 mHz, *Geophys. J. Int.*, **143**, 113–118.

[1] earthquake.usgs.gov/earthquakes/eqinthenews/2011/usc0001xgp/neic_c0001xgp_gcmt.php

[2] earthquake.usgs.gov/earthquakes/eqinthenews/2011/usc0001xgp/neic_c0001xgp_cmt.php

[3] earthquake.usgs.gov/earthquakes/eqinthenews/2011/usc0001xgp/neic_c0001xgp_wmt.php

[4] www.tectonics.caltech.edu/slip_history/2011_tohoku-oki-tele

[5] www.geol.ucsb.edu/faculty/ji/big_earthquakes/2011/03/0311_v3/Honshu.html

Appendix

Spherical harmonic decomposition is commonly used to evaluate eigenfrequencies and eigenfunctions of spherical models. In such a case the momentum and Poisson partial differential equations that describe the spheroidal displacement and changes of the gravity field of a prestressed self-gravitating elastic medium are rewritten into the system of the three second-order ordinary differential equations,

$$\begin{aligned} \beta U_n'' + \frac{2\beta}{r}U_n' + \left(\frac{4\rho_0 g_0}{r} - 4\pi G\rho^2 - \frac{2\beta+\mu N}{r^2}\right)U_n - \\ -\frac{N}{r}\left(\lambda+\mu\right)V_n' + \left(\frac{3\mu+\lambda}{r^2} - \frac{\rho_0 g_0}{r}\right)NV_n - \rho_0 F_n' &= -\rho_0\omega_n^2 U_n, \end{aligned} \tag{4.1}$$

$$\mu V_n'' + \frac{2\mu}{r}V_n' - \frac{\beta N}{r^2}V_n + \frac{\mu+\lambda}{r}U_n' + \left(\frac{2\beta}{r^2} - \frac{\rho_0 g_0}{r}\right)U_n - \frac{\rho_0}{r}F_n = -\rho_0\omega_n^2 V_n, \tag{4.2}$$

$$F_n'' + \frac{2}{r}F_n' - \frac{N}{r^2}F_n + 4\pi G\rho_0\left(U_n' + \frac{2}{r}U_n - \frac{N}{r}V_n\right) = 0, \tag{4.3}$$

where r is the radius, ρ_0 is the reference density, G is the Newton gravitational constant, λ and μ are the elastic Lamé parameters, $\beta = \lambda + 2\mu$, n is the degree of the spherical harmonic decomposition, $N = n(n+1)$ and the derivative in the radial direction is denoted by $f' \equiv \mathrm{d}f/\mathrm{d}r$. U_n, V_n and F_n are the coefficients of spherical harmonic expansions representing the spheroidal displacement vector and incremental gravitational potential, and ω_n are the angular frequencies of free oscillations for a fixed n.

We follow the finite-difference approach designed by *Fornberg (1996)*, where a pseudospectral accuracy of finite differences is reached by evaluating the unknowns at the extrema of the Chebyshev polynomials. Note that in layered models, such as the PREM, an independent Chebyshev grid is applied to each layer. Equations (4.1)–(4.3), including boundary conditions, can then be rewritten into the unified matrix form,

$$\left(\mathbf{P}^{-1}\cdot\mathbf{R}\right)\cdot\boldsymbol{Y} = -\frac{1}{\omega^2}\boldsymbol{Y}, \tag{4.4}$$

where $\boldsymbol{P}$ and $\boldsymbol{R}$ are the matrices of coefficients depending on model parameters and discretization, $\boldsymbol{Y}$ are eigenfunctions composed of the discrete values U_n, V_n and F_n and $-\frac{1}{\omega^2}$ are the eigennumbers. The discrete forms of the matrices $\boldsymbol{P}$, $\boldsymbol{R}$ and the vector $\boldsymbol{Y}$ are derived in *Zábranová et al. (2009)*.

The PREM model is frequency dependent and its parameters that appear in the formulas above are evaluated for a fiducial frequency $\bar{\omega}$. Following *Dahlen and Tromp (1998)*, the slight shift of an individual mode frequency ω_0 caused by isotropic anelasticity can be incorporated by the formula

$$\omega = \omega_0 + \frac{1}{\pi}\omega_0 Q^{-1}\ln\left(\omega_0/\bar{\omega}\right), \tag{4.5}$$

where Q^{-1} is the inverse quality factor.

Splitting frequency perturbations of an isolated multiplet due to the effects of the Earth's rotation and hydrostatic ellipticity can be expressed as

$$\delta\omega_m = \omega(a + bm + cm^2), \tag{4.6}$$

where m, $-n \leq m \leq n$, is the order. The term b arises from the first-order effect of the Coriolis force and the terms a and c arise from ellipticity and second-order effects of rotation.

The vertical acceleration of an instrument can be written in the form

$$\boldsymbol{a}(\boldsymbol{x}, t) = \sum_{nlm} \boldsymbol{A}_{nlm}(\boldsymbol{x}) \exp\left[i_l\omega_n \left(1 + a + bm + cm^2\right) t - {}_l\gamma_n t\right], \tag{4.7}$$

where the sum is over all multiplets defined by degrees n and overtone numbers l. The coefficients $\boldsymbol{A}_{nlm}$ are given by the moment tensor, a source-receiver geometry and the eigenfunctions, and ${}_l\gamma_n$ is the decay rate of each multiplet.

Chapter 5

Constraints on the centroid moment tensors of the 2010 Maule and 2011 Tohoku earthquakes from radial modes

Published in Geophysical Research Letters,
Volume 39, Issue 18, September 2012, doi:10.1029/2012GL052850

Eliška Zábranová[1], Ctirad Matyska[1], Ladislav Hanyk[1] and Vojtech Pálinkáš[2]

[1]Department of Geophysics, Faculty of Mathematics and Physics, Charles University in Prague, V Holešovičkách 2, CZ-18000, Prague, Czech Republic
[2]Research Institute of Geodesy, Topography and Cartography, Zdiby, Czech Republic

Abstract

Surface acceleration caused by the radial modes depends only on the M_{rr} component of the centroid moment tensor and on its depth assuming the isotropic component to be negligible. The ${}_0S_0$-mode amplitude enables one to obtain a relatively narrow interval of M_{rr} values, whereas ${}_1S_0$-mode amplitude is more sensitive to centroid depth. We have used these facts to analyze the 2010 Maule (Chile) $M_w = 8.8$ and 2011 Tohoku (Japan) $M_w = 9.1$ earthquakes using PREM. Superconducting gravimeter data available within the framework of the Global Geodynamic Project reveal that the M_{rr} components of these earthquakes should be in the interval 0.95–1.15 $\times 10^{22}$ Nm (Maule) and 1.50–1.75 $\times 10^{22}$ Nm (Tohoku), respectively. Re-evaluation of the modal quality factors Q is needed to obtain constraints on M_{rr} self-consistently. The joint analysis of gravity data from both events yields $Q = 5500 \pm 140$ for the ${}_0S_0$-mode and $Q = 2000 \pm 80$ for the ${}_1S_0$-mode. We were not able to determine the quality factor of the ${}_2S_0$ mode with an accuracy sufficient to allow meaningful constraints ($Q = 1120 \pm 270$).

5.1 Introduction

The source mechanism of the 2011 Tohoku $M_w = 9.1$ earthquake was first shown by rapid solutions published a few minutes and hours after the event [*Nettles et al.*, 2011 (abbreviated as PS1 in Fig. 5.2); *Polet and Thio*, 2011 (PS2); *Duputel et al.*, 2011 (PS3); *Hayes et al.*, 2011; *Shao et al.*, 2011] and then studied in detail by means of various seismic datasets: teleseismic and regional body and surface waves [*Koper et al.*, 2011; *Yokota et al.*, 2011; *Zhang et al.* 2011] and strong motions [*Honda et al.*, 2011; *Kurahashi and Irikura*, 2011; *Suzuki et al.*, 2011; *Yoshida et al.*, 2011]. Similarly, there are rapid solutions available for the 2010 Maule $M_w = 8.8$ earthquake [*Ekström and Nettles*, 2010 (abbreviated as PS1 in Fig. 5.3); *USGS*, 2010a (PS2); *USGS*, 2010b (PS3)] followed by further source-mechanism studies [*Delouis et al.*, 2010; *Lay et al.*, 2010; *Koper et al.*, 2012; *Okal et al.*, 2012].

Moreover, a network of superconducting gravimeters publishes data within the framework of the Global Geodynamic Project (GGP)[1]. These earthquakes (together with the 2004 Sumatra earthquake) are thus the best instrumentally recorded giant events in the history of seismology. We have used gravity data from superconducting gravimeters to obtain radial mode amplitudes and to demonstrate how they constrain the M_{rr} components of the moment tensor and centroid depths of the Maule and Tohoku earthquakes.

5.2 Method

The acceleration of a spherically symmetric, non-rotating, anelastic Earth at a receiver located at $\mathbf{x_r}(r_r, \vartheta_r, \varphi_r)$, that is excited by a moment-tensor source $\mathbf{M}$ situated at $\mathbf{x_s}(r_s, \vartheta_s, \varphi_s)$, is given by a superposition of spheroidal and toroidal modes,

$$\mathbf{a}(\mathbf{x_r}, \mathbf{x_s}, t) = \sum_k \mathbf{A}_k(\mathbf{x_r}, \mathbf{x_s}) \cos(\omega_k t) \exp\left(-\frac{\omega_k t}{2Q_k}\right) . \tag{5.1}$$

The coefficients $\mathbf{A}_k(\mathbf{x_r}, \mathbf{x_s})$ are linearly proportional to the moment-tensor components, and they depend on a source-receiver geometry and the mode eigenfunctions; ω_k are angular frequencies and Q_k quality factors of the modes.

If we consider a part of the response caused by a radial (degree-zero) mode, we can directly determine the coefficients $\mathbf{A_k}(\mathbf{x_r}, \mathbf{x_s})$ that are independent of the horizontal coordinates [*Dahlen and Tromp*, 1998, Section 10.3],

$$\mathbf{A}_0(r_r, r_s) = \frac{U_r}{4\pi}\left[M_{rr}U'_s + (M_{\theta\theta} + M_{\phi\phi})\frac{U_s}{r_s}\right]\mathbf{e_r} , \tag{5.2}$$

where the eigenfunction U and its derivative U' are only radially dependent, $U_r = U(r_r)$, $U_s = U(r_s)$, and M_{rr}, $M_{\theta\theta}$ and $M_{\phi\phi}$ are diagonal spherical polar components of the centroid moment tensor $\mathbf{M}$.

If we take into account that the isotropic component of the source is negligible [*Kikuchi and Kanamori*, 1994; *Okal*, 1996], i.e., $M_{rr} = -(M_{\theta\theta} + M_{\phi\phi})$, the surface acceleration of a device caused by the radial modes depends on only the one component of the moment tensor M_{rr} and on the depth of the centroid,

$$\mathbf{A}_0(a, r_s) = \frac{U_a}{4\pi}\left(1 + \frac{2g}{\omega^2 a}\right) M_{rr}\left(U'_s - \frac{U_s}{r_s}\right)\mathbf{e_r} , \tag{5.3}$$

[1] http://www.eas.slu.edu/GGP/ggphome.html

where $U_a = U(a)$ and the free-air change in gravity due to the radial displacement of the device is included, e.g. [*Dahlen and Tromp*, 1998]. Therefore, simultaneous employment of several radial modes enables, in principle, one to determine not only the M_{rr} component of the moment tensor but also the centroid depth [*Lundgren and Okal*, 1988]. The centroid represents a point source in space and time but megathrust events are represented by finite-source solutions in many applications where, e.g., dimension and/or directivity of the source play a role. We calculated spheroidal modes up to 1.7 mHz also for the finite-source solution by *Hayes et al.* [2011] and found that there are no significant effects if this finite source is replaced by a suitable point source; see also [*Zábranová et al.*, 2012], where finite-source representations of the Tohoku event are taken into account. On the other hand, the calculated modal amplitudes—and, subsequently, the constraints on the moment tensor—depend on local values of elastic coefficients at the source, that is the clear shortcoming of a point-source representation.

We calculate the eigenfrequencies and the eigenfunctions of the spherical equivalent-rock PREM [*Dziewonski and Anderson*, 1981], where the upper 3-km layer of water is replaced by a 1.2-km-thick rock-layer with the same mass, by means of our pseudospectral finite-difference matrix-eigenvalue approach [*Zábranová et al.*, 2009]. The frequencies and eigenfunctions of the degenerate multiplets evaluated by our code for the PREM were tested by the Mineos software package.

If non-spherical corrections due to the rotation and ellipticity are considered in this degree-zero case, only the frequencies of modes are slightly shifted, so formulas (5.1)–(5.3) can again be used because each radial mode consists just of one singlet [*Dahlen and Tromp*, 1998], and coupling with other modes is negligible [*Davis et al.*, 2005]. Moreover, *Rosat et al.* [2007] showed that for a three-dimensional rotating elliptic Earth model, the difference between theoretically predicted minimum and maximum amplitudes of the ${}_0S_0$ mode reaches only 2%; therefore, we assume that excitation is almost independent of source-station horizontal geometry, and we averaged observed signals from different stations to suppress the noise.

5.3 Data analysis and results

The data for the Maule (32 days) and Tohoku (20 days) earthquakes are freely available on the GGP web pages. Only the stations shown in Fig. 5.1 were employed because the time series available from other stations were either too short or affected by gaps and/or steps. A high-pass Butterworth filter (above 0.1 mHz) was used to remove local tides from raw gravity data (sampled at 1 s) corrected for atmospheric effects using locally recorded atmospheric pressure data and a nominal admittance factor of -3 nm/s^2/hPa.

Figs. 5.2 and 5.3 demonstrate the constraints on the M_{rr} component of the moment tensor and the depth of the Maule $M_w = 8.8$ and Tohoku $M_w = 9.1$ earthquakes obtained from the amplitudes of ${}_0S_0$ and ${}_1S_0$. They are clearly isolated in the spectrum, and the level of observed noise is low (see the mode amplitudes in Figs. 5.4 and 5.5). A Hann taper and Fourier transform were applied to averaged data signal and synthetic calculations. The synthetic solutions were found by a grid search in depth with 1-km step, using the fact that dependence of amplitude on the M_{rr} parameter is linear for a fixed depth.

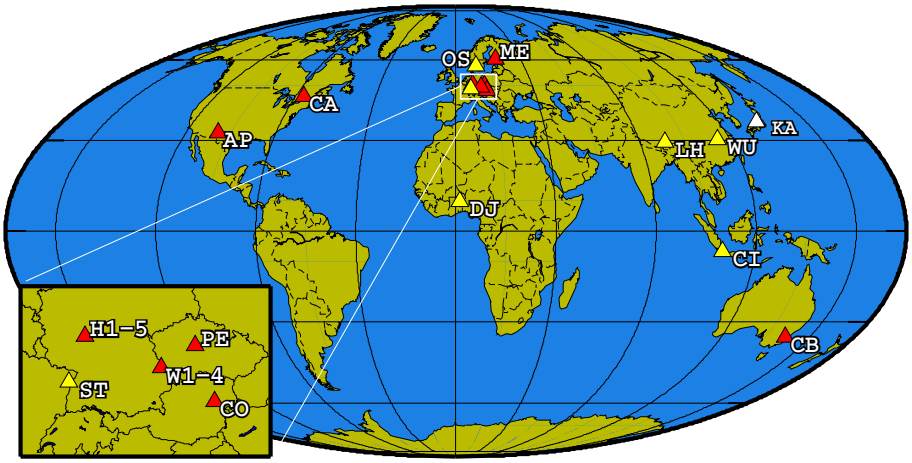

Figure 5.1: The triangles represent the SG sites used in this study. Red ones were employed for both events, white only for the 2010 Maule earthquake and yellow only for the 2011 Tohoku earthquake.

The quality factor Q is a key parameter, and its value used in synthetic calculations can substantially influence the results. For example, *Riedesel et al.* [1980] found that Q is between 5600 and 5833 for the ${}_0S_0$ mode and between 1850 and 1960 for the ${}_1S_0$ mode. Lower values for the ${}_0S_0$ mode were reported by *Roult et al.* [2006] (5489), *Xu et al.* [2008] (5400) and *Okal and Stein* [2009] (5579), who, on the other hand, obtained a higher value (2017) for the ${}_1S_0$ mode. We analyzed gravity data from the Maule and Tohoku earthquakes (32- and 20-days long records, respectively, for ${}_0S_0$, 13-days long records for ${}_1S_0$ and 5-days long records for ${}_2S_0$) using several shifted time windows and the fact that $Q^{-1} = T/(\pi\Delta t)\ln\frac{A_{ref}}{A}$ for each

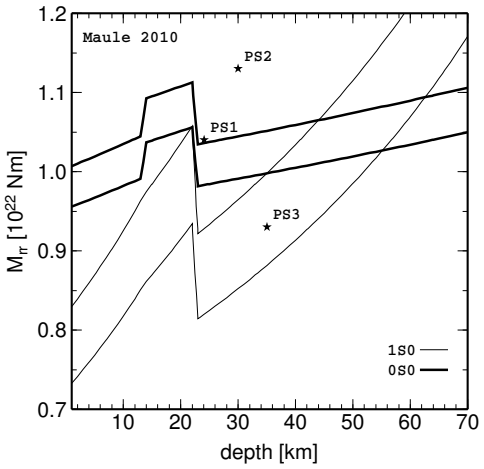

Figure 5.2: Dependence of the M_{rr} component of the centroid moment tensor on the centroid depth from the ${}_0S_0$ and ${}_1S_0$ amplitudes for the 2010 Maule earthquake. For each mode, the interval corresponding to ± one standard deviation of amplitude-spectra and quality factors is drawn. Stars denote published point-source solutions (PS1, PS2 and PS3).

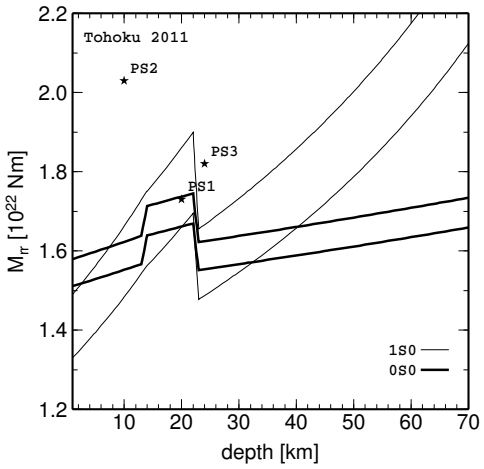

Figure 5.3: Dependence of the M_{rr} component of the centroid moment tensor on the centroid depth from the ${}_0S_0$ and ${}_1S_0$ amplitudes for the 2011 Tohoku earthquake. For each mode, the interval corresponding to ± one standard deviation of amplitude-spectra and quality factors is drawn. Stars denote published point-source solutions (PS1, PS2 and PS3).

	${}_0S_0$			${}_1S_0$		
	760h	450h	350h	190h	170h	150h
Maule	1.5	1.7	1.7	3.3	3.5	3.7
Tohoku	x	1.3	1.5	3.0	2.9	2.9

Table 5.1: The lengths of employed time windows and corresponding amplitude-spectra standard deviations (percents) for the two radial modes.

record, where T is period of a mode and Δt is time shift between time windows used to calculate spectral amplitudes A_{ref} and A. We found $Q = 5500 \pm 140$ for the ${}_0S_0$-mode, $Q = 2000 \pm 80$ for the ${}_1S_0$-mode and $Q = 1120 \pm 270$ for the ${}_2S_0$-mode. ${}_2S_0$ would confine the depth even more than the ${}_1S_0$ mode if the Q factor were determined with a similar accuracy. However, the relative error is so high that we have not been able to use this mode as another meaningful constraint.

In the case of Maule, we have employed three time series lasting up to 32 days for ${}_0S_0$ and three time series up to 8 days for ${}_1S_0$ to determine mode amplitudes as specified in Table 5.1. In the case of Tohoku, such long data sets are not available, and we were left with 20-day records. For each time window the standard deviation expressed in percents about averaged amplitude was calculated from the amplitudes obtained from individual station records.

The depth-dependence of M_{rr} obtained from the ${}_0S_0$-mode-amplitude calculations is weak (jumps at depths of 13 and 22 km are caused by jumps in the radial derivatives of the mode displacement on the corresponding structural interfaces of the equivalent-rock PREM) and this mode thus confines the M_{rr} magnitudes into relatively narrow bands of $0.95–1.15 \times 10^{22}$ Nm for the Maule earthquake and 1.50–

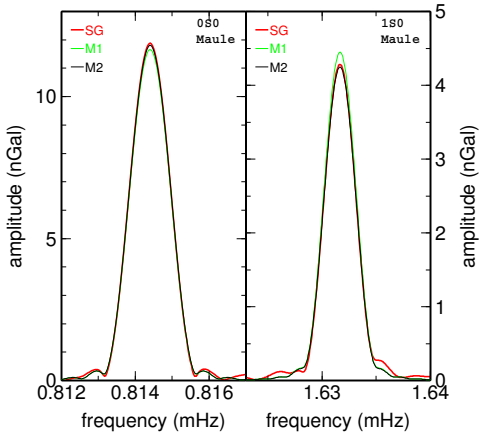

Figure 5.4: Vertical acceleration amplitude spectra of the modes ${}_0S_0$ and ${}_1S_0$ from the averaged SG data (red) and the two synthetics: M1 (green, depth 21 km; $M_{rr} = 1.055 \times 10^{22}$ Nm) and M2 (black, depth 44 km; $M_{rr} = 1.025 \times 10^{22}$ Nm) for the 2010 Maule earthquake. A Hann filter and Fourier transform were applied to 450- (170-)hour time series.

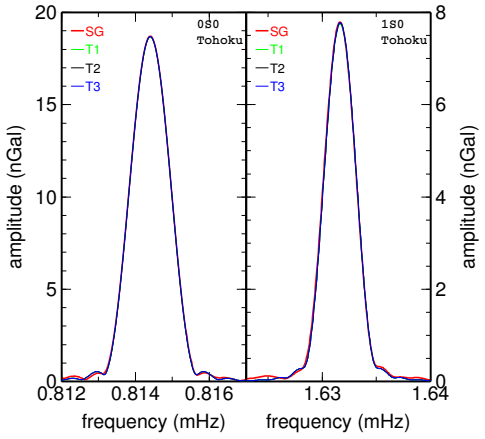

Figure 5.5: Vertical acceleration amplitude spectra of the modes ${}_0S_0$ and ${}_1S_0$ from the averaged SG data (red) and the three synthetics: T1 (green, depth 13 km; $M_{rr} = 1.60 \times 10^{22}$ Nm), T2 (black, depth 18 km; $M_{rr} = 1.69 \times 10^{22}$ Nm) and T3 (blue, depth 29 km; $M_{rr} = 1.60 \times 10^{22}$ Nm) for the 2011 Tohoku earthquake. A Hann filter and Fourier transform were applied to 450- (170-) hour time series.

1.75×10^{22} Nm for the Tohoku earthquake. On the other hand, the solution band produced by the ${}_1S_0$ mode is more depth-dependent, and it demonstrates that centroid depths should be located in the lower crust or just below the Moho for the Tohoku event but might be deeper for Maule.

Figs. 5.4 and 5.5 demonstrate an agreement in the amplitude spectra between the averaged SG data and the synthetics. We use 450-hour (${}_0S_0$) and 170-hour (${}_1S_0$) time series. Fig. 5.4 shows two solutions (M1 and M2) at the depths 21 km ($M_{rr} = 1.055 \times 10^{22}$ Nm) and 44 km (1.025×10^{22} Nm) for the Maule earthquake. Fig. 5.5 shows three solutions (T1, T2 and T3) at the depths 13 km (1.60×10^{22} Nm), 18 km (1.69×10^{22} Nm) and 29 km (1.60×10^{22} Nm) for the Tohoku earthquake.

5.4 Conclusions

We have re-evaluated the quality factor Q of the ${}_0S_0$-mode ($Q = 5500 \pm 140$) and the ${}_1S_0$-mode ($Q = 2000 \pm 80$) and demonstrated that M_{rr} of the 2010 Maule and 2011 Tohoku earthquakes should fall within the intervals 0.95–1.15×10^{22} Nm and 1.50–1.75×10^{22} Nm, respectively, to yield the observed ${}_0S_0$-mode amplitude. Moreover, the ${}_1S_0$ mode provides constraints on the centroid depth. From the three rapid centroid solutions shown in Figs. 5.2 and 5.3, only the PS1 M_{rr} component lies in the intervals mentioned above. The PS2 value is close to the upper limit for the Maule earthquake and clearly overestimates the Tohoku event. On the other hand, the PS3 value slightly underestimates the first event and overestimates the second earthquake. That these constraints on the M_{rr} component are not, in general, satisfactorily fulfilled, can be explained by the fact that radial modes are rather weak, as the non-diagonal moment-tensor terms dominate in the corresponding source solutions. Therefore, the weights of M_{rr} in full moment-tensor-waveform inversions are relatively small.

Acknowledgments We thank F. Gallovič for long and fruitful discussions, J. Zahradník for encouragement, J. Velímský for broad support, C. Bina for comments, and two anonymous reviewers for constructive reviews. This research was supported by the Grant Agency of the Charles University under projects 2010-141610 and 2012-265308 and by research project MSM 0021620860 of the Czech Ministry of Education, Youth and Sports.

References

Dahlen, F. A., and J. Tromp (1998), *Theoretical Global Seismology*, Princeton University Press, Princeton.

Davis, P., M. Ishii, and G. Masters (2005), An assessment of the accuracy of GSN sensor response information, *Seis. Research Letters, 76*, 678–683.

Delouis, B., J.-M. Nocquet, and M. Vallée (2010), Slip distribution of the February 27, 2010 Mw = 8.8 Maule Earthquake, central Chile, from static and high-rate GPS, InSAR, and broadband teleseismic data, *Geophys. Res. Lett., 37*, L17305, doi:10.1029/2010GL043899.

Duputel, Z., L. Rivera, H. Kanamori, G. P. Hayes, B. Hirshorn, and S. Weinstein (2011), Real-time W phase inversion during the 2011 off the Pacific coast of Tohoku

earthquake, *Earth Planets Space, 63*, 535–539.
http://earthquake.usgs.gov/earthquakes/eqinthenews/2011/usc0001xgp/neic_c0001xgp_wmt.php

Dziewonski, A. M., and D. L. Andersen (1981), Preliminary reference Earth model, *Phys. Earth Planet. Inter., 25*, 297–356.

Ekström, G., and Nettles, M., 2010.
http://earthquake.usgs.gov/earthquakes/eqinthenews/2010/us2010tfan/neic_tfan_gcmt.php

Hayes, G. P., X. Li, C. Ji, and T. Maeda (2011), Rapid source characterization of the 2011 Mw 9.0 off the Pacific coast of Tohoku Earthquake, *Earth Planets Space, 63*, 529–534.

Honda, R., Y. Yukutake, H. Ito, M. Harada, T. Aketagawa, A. Yoshida, S. Sakai, S. Nakagawa, N. Hirata, K. Obara, and H. Kimura (2011), A complex rupture image of the 2011 off the Pacific coast of Tohoku earthquake revealed by the MeSO-net, *Earth Planets Space, 63*, 583–588.

Kikuchi, M., and H. Kanamori (1994), The mechanism of the deep Bolivia earthquake of June 9, 1994, *Geophys. Res. Lett., 21*, 2341–2344.

Koper, K. D., A. R. Hutko, T. Lay, C. J. Ammon, and H. Kanamori (2011), Frequency-dependent rupture process of the 2011 Mw 9.0 Tohoku Earthquake: Comparison of short-period P wave backprojection images and broadband seismic rupture models, *Earth Planets Space, 63*, 599–602.

Koper, K. D., A. R. Hutko, T. Lay, and O. Sufri (2012), Imaging short-period seismic radiation from the 27 February 2010 Chile (MW 8.8) earthquake by back-projection of P, PP, and PKIKP waves, *J. Geophys. Res., 117*, B02308. doi:10.1029/2011JB008576.

Kurahashi, S., and K. Irikura (2011), Source model for generating strong ground motions during the 2011 off the Pacific coast of Tohoku earthquake, *Earth Planets Space, 63*, 571–576.

Lay, T., C. J. Ammon, H. Kanamori, K. D. Koper, O. Sufri, and A. R. Hutko (2010), Teleseismic inversion for rupture process of the 27 February 2010 Chile (Mw 8.8) earthquake, *Geophys. Res. Lett., 37*, L13301, doi:10.1029/2010GL043379.

Lundgren, P. R., and E. A. Okal (1988), Slab decoupling in the Tonga drc: The June 22, 1977, earthquake, *J. Geophys. Res., 93*, 13355–13366.

Nettles, M., G. Ekström, and H. C. Koss (2011), Centroid-moment-tensor analysis of the 2011 off the Pacific coast of Tohoku earthquake and its larger foreshocks and aftershocks, *Earth Planets Space, 63*, 519–523.
http://earthquake.usgs.gov/earthquakes/eqinthenews/2011/usc0001xgp/neic_c0001xgp_gcmt.php

Okal, E. A. (1996), Radial modes from the great 1994 Bolivian earthquake: No evidence for an isotropic component to the source, *Geophys. Res. Lett., 23*, 431–434.

Okal, E. A., and S. Stein (2009), Observations of ultra-long period normal modes from the 2004 Sumatra-Andaman earthquake, *Phys. Earth Planet. Inter., 175*, 53–62.

Okal, E. A., S. Hongsresawat, and S. Stein (2012), Split-mode evidence for no ultraslow component to the source of the 2010 Maule, Chile, earthquake, *Bull. Seismol. Soc. Am., 102*, 391–397.

Polet, J., and H. K. Thio (2011), Centroid-moment-tensor analysis of the 2011 off the Pacific coast of Tohoku Earthquake and its larger foreshocks and aftershocks, *Earth Planets Space, 63*, 519–523.
http://earthquake.usgs.gov/earthquakes/eqinthenews/2011/usc0001xgp/neic_c0001xgp_cmt.php

Riedesel, M., D. Agnew, J. Berger, and E. Gilbert(1980), Stacking for the frequencies and Qs of ${}_0S_0$ and ${}_1S_0$, *Geophys. J. R. Astr. Soc., 62*, 457–471.

Roult, G., S. Rosat, and E. Clévédé (2006), New determinations of Q quality factors and eigenfrequencies for the whole set of singlets of the Earth's normal modes ${}_0S_0$, ${}_0S_2$, ${}_0S_3$ and ${}_2S_1$ using superconducting gravimeter data from the GGP network, *J. Geod., 41*, 345–357.

Rosat, S., S. Watada, and T. Sato (2007), Geographical variations of the 0S0 normal mode amplitude: Predictions and observations after the Sumatra-Andaman earthquake, *Earth Planets Space, 59*, 307–311.

Shao, G., X. Li, C. Ji, and T. Maeda (2011), Focal mechanism and slip history of the 2011 Mw 9.1 off the Pacific coast of Tohoku earthquake, constrained with teleseismic body and surface waves, *Earth Planets Space, 63*, 559–564.

Suzuki, W., S. Aoi, H. Sekiguchi, and T. Kunugi (2011), Rupture process of the 2011 Tohoku-Oki mega-thrust earthquake (M9.0) inverted from strong-motion data, *Geophys. Res. Lett., 38*, L00G16, doi:10.1029/2011GL049136.

USGS, 2010a.
http://earthquake.usgs.gov/earthquakes/eqinthenews/2010/us2010tfan/neic_tfan_cmt.php

USGS, 2010b.
http://earthquake.usgs.gov/earthquakes/eqinthenews/2010/us2010tfan/neic_tfan_wmt.php

Xu, Y., D. Crossley, and R. B. Herrmann (2008), Amplitude and Q of ${}_0S_0$ from the Sumatra earthquake as recorded on superconducting gravimeters and seismometers, *Seis. Res. Lett., 79*, 797–805.

Yokota, Y., K. Koketsu, Y. Fujii, K. Satake, S. Sakai, M. Shinohara, and T. Kanazawa (2011), Joint inversion of strong motion, teleseismic, geodetic, and tsunami datasets for the rupture process of the 2011 Tohoku earthquake, *Geophys. Res. Lett., 38*, L00G21, doi:10.1029/2011GL050098.

Yoshida, Y., K. Miyakoshi, and K. Irikura (2011), Source process of the 2011 off the Pacific coast of Tohoku Earthquake inferred from waveform inversion with long-period strong-motion records, *Earth Planets Space, 63*, 577–582.

Zábranová, E., L. Hanyk, and C. Matyska (2009), Matrix pseudospectral method for elastic tides modeling. In: Holota P. (Ed.), *Mission and Passion: Science. Czech National Committee of Geodesy and Geophysics, Prague,* pp. 243–260.

Zábranová, E., C. Matyska, and L. Hanyk (2012), Tests of the 2011 Tohoku earthquake source models using free-oscillation data from GOPE, *Studia Geoph. Geod., 56*, 585–594, doi:10.1007/s11200-011-9033-5.

Zhang, H., Z. Ge, and L. Ding (2011), Three sub-events composing the 2011 off the Pacific coast of Tohoku earthquake (Mw 9.0) inferred from rupture imaging by back-projecting teleseismic P waves, *Earth Planets Space, 63*, 595–598.

Chapter 6

Low-frequency centroid-moment-tensor inversion from superconducting-gravimeter data: the effect of seismic attenuation

Published in Physics of the Earth and Planetary Interiors,
Volume 235, October 2014, 25–32, doi:10.1016/j.pepi.2014.06.013

Eliška Zábranová and Ctirad Matyska

Department of Geophysics, Faculty of Mathematics and Physics, Charles University in Prague, V Holešovičkách 2, CZ-18000, Prague, Czech Republic

Abstract

After the 2010 Maule and 2011 Tohoku earthquakes the spheroidal modes up to 1 mHz were clearly registered by the Global Geodynamic Project (GGP) network of superconducting gravimeters (SG). Fundamental parameters in synthetic calculations of the signals are the quality factors of the modes. We study the role of their uncertainties in the centroid-moment-tensor (CMT) inversions. First, we have inverted the SG data from selected GGP stations to jointly determine the quality factors of these normal modes and the three low-frequency CMT components, M_{rr}, $(M_{\vartheta\vartheta} - M_{\varphi\varphi})/2$ and $M_{\vartheta\varphi}$, that generate the observed SG signal. We have used several-days-long records to minimize the trade-off between the quality factors and the CMT but it was not eliminated completely. We have also inverted each record separately to get error estimates of the obtained parameters. Consequently, we have employed the GGP records of 60-hrs lengths for several published modal-quality-factor sets and inverted only the same three CMT components. The obtained CMT tensors are close to the solution from the joint Q-CMT inversion of longer records and resulting variability of the CMT components is smaller than differences among routine agency solutions. Reliable low-frequency CMT components can thus be obtained for any quality factors from the studied sets.

Keywords: Normal modes, superconducting-gravimeter data, quality factors, CMT inversion

6.1 Introduction

CMT inversions of giant earthquakes in the frequency range below 1 mHz are based on normal-mode calculations where fundamental parameters are the quality factors of the modes. Although free oscillations of the Earth have been observed for decades, precise determination of the ultralong-period-mode quality factors is still discussed (e.g., Roult et al., 2006; Okal and Stein, 2009; Tanimoto et al., 2012; Deuss et al., 2013; Ding and Shen, 2013). The modal quality factors can be estimated directly from the observed signal attenuations. Very long high-quality records are needed because multiplet splitting into singlets of near frequencies causes complicated decrease of signal amplitudes with time, but continuous non-disrupted SG records lasting several weeks are rather rare. Determination of ultra-long-period-mode-singlet attenuations from SG and seismic data yields relatively broad ranges of values (Ding and Shen, 2013), probably due to the noise in available signals. However, in quasi-spherical approximation, when only splitting due to the Earth rotation and ellipticity is considered, the quality factors of individual singlets should be very close (e.g., Dahlen and Tromp, 1998).

The other way how to obtain the modal quality factors is, therefore, based on an inversion procedure when calculated synthetic signals are compared with the observed data provided one quality factor for all singlets of a mode is to be determined. Synthetic calculations cannot be performed without a model of earthquake source which should thus be simultaneously added into the inversion procedure to obtain self-consistent results.

Here we first deal with the problem of joint determination of both the modal quality factors and the CMT components from the spheroidal-mode observations up to 1 mHz. Since they are isolated in the spectrum, influence of mode couplings and 3-D structures to amplitude spectrum is not substantial (e.g., He and Tromp 1996), it is sufficient to calculate multiplets splitting due to the rotation and ellipticity. The observations after the 2010 Maule and 2011 Tohoku earthquakes within the GGP framework provide high-quality data that exhibit lower noise level in submilihertz frequency range than broadband seismometer data; detailed discussion can be found in, e.g., Ferreira et al. (2006).

Ultralong-period-normal modes were employed in several earthquake-source studies (e.g., Okal and Stein, 2009; Okal et al., 2012; Okal, 2013; Tanimoto and Ji, 2010; Tanimoto et al., 2012) to reveal potential ultraslow components to the seismic source of giant earthquakes by evaluating low-frequency estimates of the scalar moment M_0 when the strike, dip and rake were fixed in agreement with the Global CMT double-couple-focal mechanisms. The one parameter was thus inverted using a priori estimates of the remaining source parameters (and quality factors). It is clear that such an approach stabilizes inversion of M_0 but the question arises whether the influence of errors in determination of the strike, dip and rake (Duputel et al., 2012; Tanimoto et al., 2012; Valentine and Trampert, 2012) is negligible. Moreover, potential usage of very long records (up to several weeks) require precise knowledge of the modal quality factors.

Zábranová et al. (2012) obtained the M_{rr} component of the moment tensor by inverting the amplitudes of radial modes observed after the 2010 Maule and 2011 Tohoku earthquakes by the GGP stations. Again, they had to re-evaluate quality factors of the employed modes to obtain self-consistent results. Since the radial

modes are not split, their quality factors can be obtained directly from the records; thus, this source inversion can be done independently and used as a benchmark for the most influential M_{rr} component. For this reason we do not incorporate the radial modes into this study.

Here we show that vertical acceleration of the studied spheroidal modes generated by shallow earthquakes is sensitive to the three components of the CMT, assuming the isotropic component of the source to be negligible: the diagonal terms of the CMT, M_{rr} and $(M_{\vartheta\vartheta}-M_{\varphi\varphi})/2$, and its ϑ-φ component $M_{\vartheta\varphi}$, see eqns. (6.1)-(6.3) and Table 6.1 below. Quite recently, Bogiatzis and Ishii (2014) tried to invert the whole CMT tensor from the analysis of 15 modes observed by the Global Seismograph Network after the 2011 Tohoku earthquake but the $M_{r\vartheta}$ and $M_{r\varphi}$ components were not resolved. We demonstrate that the three resolvable CMT components can be, in principle, obtained simultaneously with the quality factors of the modes in a joint inversion procedure utilizing long SG records. However, there is still a trade-off between the quality factors and the M_{rr} component of the CMT. Therefore, we deal also with the CMT inversion from short SG records where influence of quality-factor uncertainties is more suppressed.

6.2 Synthetic calculations of SG signals

The total ground acceleration at $\mathbf{x_r}(r_r, \vartheta_r, \varphi_r)$, excited by a source situated at $\mathbf{x_s}(r_s, \vartheta_s, \varphi_s)$, is given by a superposition of spheroidal and toroidal modes,

$$\mathbf{a}(\mathbf{x_r}, \mathbf{x_s}, t) = \mathrm{Re}\left[\sum_k \mathbf{A}_k(\mathbf{x_r}, \mathbf{x_s}) \exp\left(i\omega_k t - \frac{\omega_k t}{2Q_k}\right)\right] , \tag{6.1}$$

where index k contains all degrees (angular order), overtones (radial order) and singlets (azimuthal order), ω_k are angular frequencies and Q_k are quality factors of the modes.

The coefficients $\mathbf{A}_k(\mathbf{x_r}, \mathbf{x_s})$ are linearly dependent on $\mathbf{M} : \mathbf{e}_k(\mathbf{x_s})\mathbf{s}_k(\mathbf{x_r})$, where $\mathbf{M}$ is the source moment tensor, $\mathbf{e}_k = \frac{1}{2}\left[\nabla\mathbf{s}_k + (\nabla\mathbf{s}_k)^{\mathrm{T}}\right]$ is the strain and $\mathbf{s}_k(\mathbf{x_s})$ and $\mathbf{s}_k(\mathbf{x_r})$ are eigenfunctions evaluated in a source and a receiver location, respectively. We included the potential-perturbation, free-air and tilt to model a realistic device response (Dahlen and Tromp, 1998), as well as the Earth ellipticity and rotation leading to multiplets splitting (Dahlen and Sailor, 1979), and calculated the coefficients $\mathbf{A}_k(\mathbf{x_r}, \mathbf{x_s})$ using the formulas that are given explicitly for splitting of an isolated multiplet (Dahlen and Tromp, 1998; Chapter 14.2 and Appendix D1). We calculate the eigenfrequencies and eigenfunctions by our pseudospectral finite-difference matrix-eigenvalue approach (Zábranová et al., 2009) applied to the spherical equivalent-rock PREM (Dziewonski and Anderson, 1981), where the upper 3-km layer of water is replaced by a 1.2-km-thick rock layer with the same mass. We thus keep the mass of the Earth and avoid calculations in a thin water layer at the surface.

Assuming negligible isotropic component of the source we decompose the moment tensor $\mathbf{M} = (M_{rr}, M_{\vartheta\vartheta}, M_{\varphi\varphi}, M_{r\vartheta}, M_{r\varphi}, M_{\vartheta\varphi})$, where M_{rr},...,$M_{\vartheta\varphi}$ are its spherical components, into five suitable base moment tensors,

$$\mathbf{M} = M_{rr}\mathbf{G}_1 + \frac{M_{\vartheta\vartheta} - M_{\varphi\varphi}}{2}\mathbf{G}_2 + M_{r\vartheta}\mathbf{G}_3 + M_{r\varphi}\mathbf{G}_4 + M_{\vartheta\varphi}\mathbf{G}_5 , \tag{6.2}$$

where

$$\begin{aligned}
\mathbf{G}_1 &= (1, -1/2, -1/2, 0, 0, 0) \ , \\
\mathbf{G}_2 &= (0, 1, -1, 0, 0, 0) \ , \\
\mathbf{G}_3 &= (0, 0, 0, 1, 0, 0) \ , \\
\mathbf{G}_4 &= (0, 0, 0, 0, 1, 0) \ , \\
\mathbf{G}_5 &= (0, 0, 0, 0, 0, 1) \ .
\end{aligned} \tag{6.3}$$

We use this representation of the CMT to distinguish between the CMT components that are able to generate strong vertical acceleration and those of negligible influence. Relative strengths of signals produced by the base moment tensors for the centroid depth of 20 km are shown in Table 6.1. The $M_{r\vartheta}$ and $M_{r\varphi}$ components do not generate any significant vertical acceleration, i.e., tangential stress vanishes near the surface (see also, e.g., Dziewonski et al., 1981; Ferreira and Woodhouse, 2006; Bukchin et al., 2010; Bogiatzis and Ishii, 2014). The mode ${}_0S_2$ is generated mainly by M_{rr}, and its sensitivity to the remaining components is weak. Nevertheless, the other modes are sensitive also to $(M_{\vartheta\vartheta} - M_{\varphi\varphi})/2$ and $M_{\vartheta\varphi}$, and these two components can thus be inverted together with M_{rr}. Note that the signal generated by $\mathbf{G}_3$ and $\mathbf{G}_4$ raises with the source depth and, in principal, full CMT of the deepest earthquakes could be achieved from the SG-data inversion.

relative strength of signals					
	G_1	G_2	G_3	G_4	G_5
${}_0S_2$	0.907	0.045	0.0015	0.0015	0.045
${}_0S_3$	0.670	0.165	0.0000	0.0000	0.165
${}_0S_4$	0.589	0.204	0.0010	0.0010	0.205
${}_1S_2$	0.404	0.282	0.0159	0.0159	0.282
${}_0S_5$	0.553	0.221	0.0024	0.0024	0.221

Table 6.1: The ratios between maximal $|\mathbf{A}_k|$ of vertical acceleration around the globe for individual base moment tensors and maximal amplitude of a signal generated by the sum of all 5 base moment tensors located at the 20-km depth.

6.3 Determination of quality factors from GGP data and the CMT inversion

We have used GGP data sets registered at the stations AP, BH (averaged from three sensors), CA, CB, CO, ME, PE, WE (averaged from two sensors) after the 2010 Maule earthquake and AP, BH (averaged from three sensors), CA, CB, CO, ME, OS, PE, ST, after the 2011 Tohoku earthquake having neither gaps nor steps in the recordings and with only weak signals from aftershocks (Fig. 6.1). We have averaged the signals from several sensors located at one station to suppress the noise level and not to increase the weight of such a station in the inversion. After correcting raw gravity data (sampled at 1 s) for atmospheric effects using locally recorded atmospheric pressure data and a standard barometric admittance of -3 nm/s^2/hPa (Hinderer et al., 2007), we apply a high-pass Butterworth filter (above 0.1 mHz) to

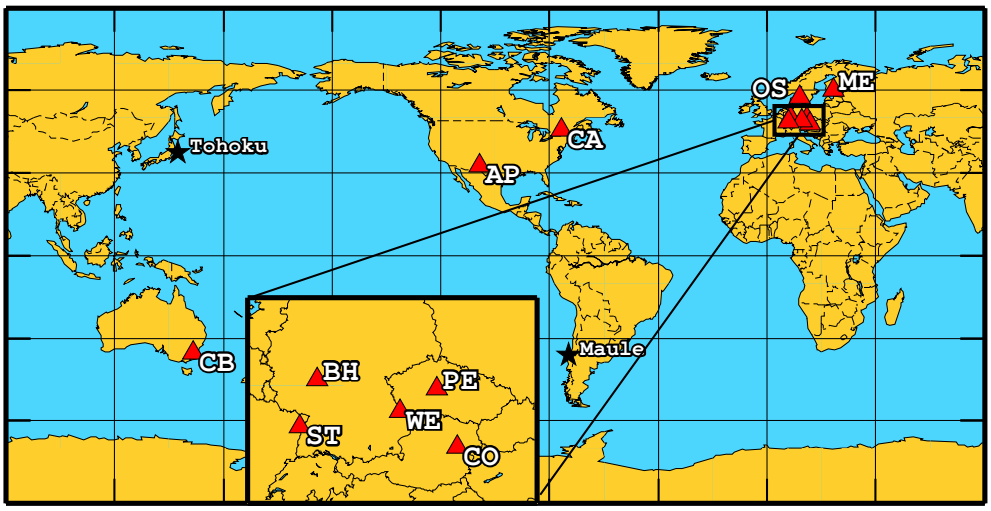

Figure 6.1: GGP stations used in this study.

remove local tides. In the studied frequency band, superconducting gravity data are less noisy than seismometer data (e.g., Ferreira et al., 2006), but they provide only the vertical component of oscillations.

The quality factors Q of individual modal multiplets are key parameters, and their values used in synthetic calculations can substantially influence the results. We determined the Qs by their simultaneous inversion together with the three CMT components M_{rr}, $(M_{\vartheta\vartheta} - M_{\varphi\varphi})/2$ and $M_{\vartheta\varphi}$. In all calculations two "low-sensitive" remaining components of $\mathbf{M}$ were fixed on the Global CMT solution, i.e. $M_{r\vartheta} = 0.23 \times 10^{22}$ Nm, $M_{r\varphi} = -1.51 \times 10^{22}$ Nm for the 2010 Maule earthquake (Ekström and Nettles, 2010) and $M_{r\vartheta} = 2.12 \times 10^{22}$ Nm, $M_{r\varphi} = 4.55 \times 10^{22}$ Nm for the 2011 Tohoku earthquake (Nettles et al., 2011). It is clear from Table 6.1 that such a choice of $M_{r\vartheta}$ and $M_{r\varphi}$ influences amplitudes of all studied fundamental modes negligibly when the remaining components of the CMT are of the same order. The overtone ${}_1S_2$ is the only exception but still these two components generate much weaker ${}_1S_2$ signal than the remaining considered components of the CMT. Since the total amplitude of this overtone is about one order of magnitude smaller than the amplitudes of the other modes, its role in the CMT inversion is very small.

	T [s]	Q_0	Q_1	Q_2	Q_3	$Q_0\,T/2$ [h]
${}_0S_2$	3234	510	496 ± 16	525	477 ± 177	230
${}_0S_3$	2135	417	409 ± 11	380	405 ± 14	124
${}_0S_4$	1546	373	394 ± 27	365	373 ± 9	80
${}_0S_5$	1190	356	350 ± 16	350	364 ± 5	59

Table 6.2: Periods T of the modes, their quality factors Q used in this study and optimal lengths of the signals according to Dahlen (1982). Q_0 was calculated from the PREM, Q_1 is our estimate contained by averaging over 4 inversion results: inversions started from the Q-values of the PREM and were performed for the centroid depth of 10 and 20 km for the 2010 Maule (20 and 30 km for the 2011 Tohoku) earthquake, Q_2 was estimated by Tanimoto *et al.* (2012) and Q_3 by Deuss *et al.* (2013).

We define the misfit function calculated for each station s and each mode m as the square of the difference between the data and synthetic-signal-amplitude spectra averaged over a narrow frequency range δf_{sm} covering all singlets, where the amplitudes are above noise level, i.e. we minimize the functional

$$\sum_{sm} \frac{1}{\delta f_{sm}} \int_{\delta f_{sm}} \left(A_s^{(d)}(f) - A_s^{(c)}(f) \right)^2 df \ ,$$

where $A^{(d)}$ ($A^{(c)}$) is the amplitude spectrum of the data (calculated synthetic signal). We do not employ the phase spectra since they are sensitive to the source finiteness and duration, noise and aftershocks (Lambotte et al., 2007; Bogiatzis and Ishii, 2014). We calculated the misfit from the optimal record lengths according to Dahlen (1982), see the last column in Table 6.2, derived for the case when amplitudes for the retrieval of source mechanism and the Hann taper for spectra calculations are utilized. All records started two hours after the origin time of the earthquakes and the synthetic calculations were performed for the two centroid depths, see Table 6.3.

We have used two-step iterative inversion procedure starting from the Q-values of the PREM: in the first step all quality factors are fixed and the three CMT components are inverted, in the second step the obtained CMT is fixed and the quality factors are inverted. The first step is then repeated with the new quality factors, then we continue with the second step etc. The convergence is very fast and only several loops (up to ten) of both steps are needed to reach misfit minimum. Note that we use grid-search in both steps with higher accuracy than 10^{20} Nm in the first step and 1 in the second step. Since the studied modes are isolated in the spectrum, the quality factor of each mode can be inverted separately in the second step. The first step could be solved as an linear inverse problem but the direct linear problem is extremely fast and thus this straightforward minimization method can be easily implemented.

Obtained quality factors in our inversion procedure are almost independent of changes in the source depth and the choice of the earthquake. Fig. 6.2 shows the amplitude spectra of synthetic and measured signals averaged by the time-window lengths to demonstrate data fitting reached in our inversion procedure. We obtained excellent fit for the modes ${}_0S_2$, ${}_0S_3$ and ${}_0S_5$ but worse results for the mode ${}_0S_4$.

centroid depth [km]	M_{rr} [10^{22} Nm]	$(M_{\vartheta\vartheta} - M_{\varphi\varphi})/2$ [10^{22} Nm]	$M_{\vartheta\varphi}$ [10^{22} Nm]
2010 Maule			
20	1.10 ± 0.01	0.55 ± 0.19	-0.09 ± 0.09
30	1.05 ± 0.01	0.54 ± 0.20	-0.10 ± 0.09
2011 Tohoku			
10	1.61 ± 0.02	0.63 ± 0.16	-0.52 ± 0.10
20	1.70 ± 0.02	0.60 ± 0.17	-0.56 ± 0.10

Table 6.3: The CMT components obtained from the joint inversion with the quality factors of the records from the stations AP, BH, CA, CB, CO, ME, PE, WE (2010 Maule) and AP, BH, CA, CB, CO, ME, OS, PE, ST (2011 Tohoku), see Fig. 6.1 and Q_1 in Table 6.2.

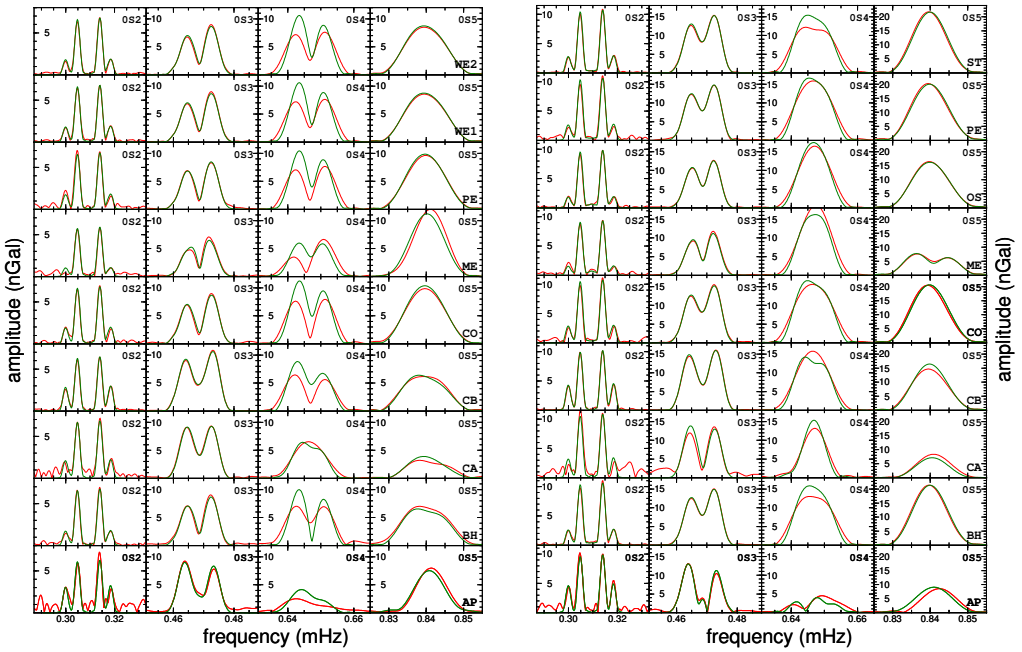

Figure 6.2: Vertical acceleration amplitude spectra of the studied modes from the SG data (red) and synthetics (green) after the 2010 Maule (left panel) and 2011 Tohoku (right panel) earthquakes. The synthetic signal was calculated for the solution of joint inversion at the depth 20 km (10 km) for the Maule (Tohoku) earthquake. A Hann filter and Fourier transform were applied to the time series of the length shown in the last column of Table 6.2 starting 2 hrs after the origin times and averaged by the length of the time windows.

In order to estimate the errors of our inversion procedure, we performed single-record inversions and then calculated the standard deviations of inverted parameters from the resultant set of these individual inversions. We first determined the quality factors from the records separately for each station (fixing the CMT components on all-station inversion values) and then obtained the CMT independently for each station (fixing the quality factors on all-station inversion values).

In Table 6.2 we compare our Q values of fundamental modes averaged over performed inversions for both earthquakes with the results obtained by Tanimoto et al. (2012) from cross-correlations in the time domain, by Deuss et al. (2013) performing splitting function inversions, as well as with those from the PREM (Dziewonski and Anderson, 1981). The fundamental-mode-quality factors of the PREM and almost all of Deus et al. (2013) lie within the obtained confidence interval but the results of Tanimoto et al. (2012) differ more. The highest standard deviation was obtained for the mode ${}_0S_4$ which corresponds to the problems with its fit as demonstrated in Fig. 6.2. We also tried to determine the quality factor of the mode ${}_1S_2$ and attained its reasonable value of $Q \simeq 310$ for the 2010 Maule earthquake but most of individual-station inversions of this quality factor were unstable; therefore, we were not able to obtain standard deviations. Moreover, the data for the Tohoku 2011 earthquake exhibit much higher values ($Q \geq 340$). These two analyses are not consistent, and we decided not to deal with this mode.

The review of the obtained CMT components is in Table 6.3; we used Global CMT source location. Our M_{rr} component for the 2011 Tohoku earthquake is in

good agreement with the recently published low-frequency-normal-mode inversion based on Global Seismographic Network data, see Table 6.2 in Bogiatzis and Ishii (2014), but the remaining components are in better agreement with the Global CMT solution (Nettles et al., 2011), the USGS CMT solution (Polet and Thio, 2011) as well as the USGS Wphase solution (Duputel et al., 2011). Note that the dependence on a source depth (mainly that of the component M_{rr}) is primarily due to the changes of the model elastic parameters. On the other hand, inversions of individual records yield almost identical values of the M_{rr} component for fixed depths that are, moreover, in a very good agreement with the M_{rr} estimates obtained from the radial mode ${}_0S_0$ inversion, see Zábranová et al. (2012).

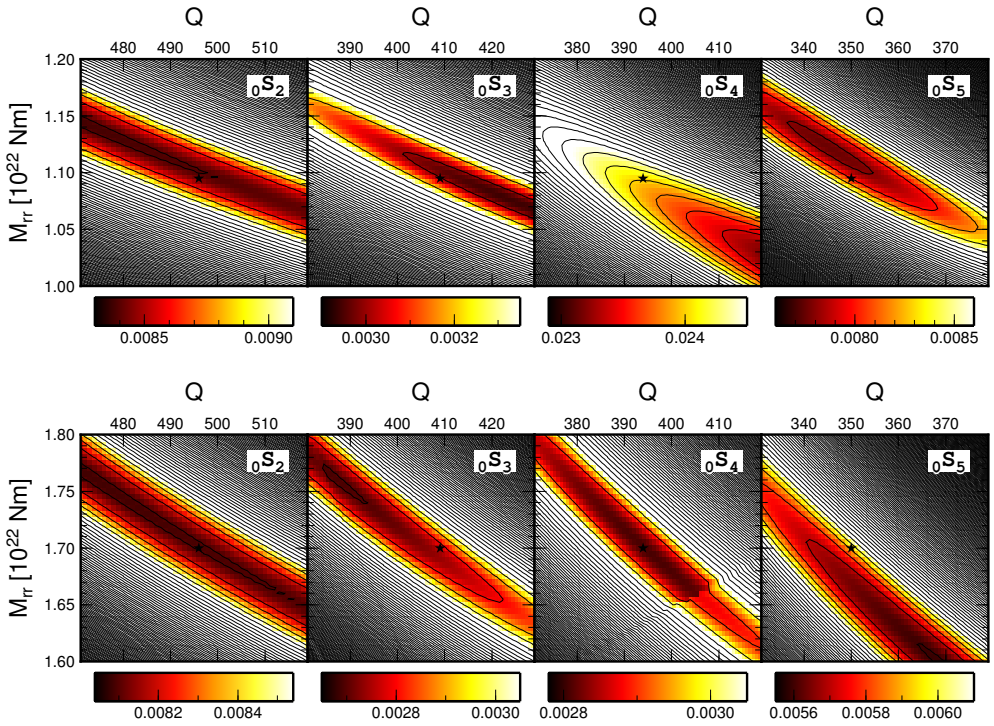

Figure 6.3: Relative misfits of individual modes for the 2010 Maule (upper panel) and 2011 Tohoku (lower panel) earthquakes for the centroid depth of 20 km showing the trade-off between the M_{rr} component and quality factors of the modes. The components $(M_{\vartheta\vartheta} - M_{\varphi\varphi})/2$ and $M_{\vartheta\varphi}$ were fixed on their values from Table 6.3 and the stars denote our solutions presented in Tables 6.2 and 6.3. The contour intervals are the same in all panels of a row but the colour scales are different.

In order to study potential trade-off between the CMT components and the quality factors, we chose the quality factors by Tanimoto et al. (2012) and Deuss et al. (2013) in the role of starting models and repeated the simultaneous inversion of all records. The results obtained from the joint inversions starting from the different quality factors lie within the confidence intervals obtained in the inversion starting from the PREM quality-factor set Q_0. Then we computed the CMT components for the fixed quality-factor sets (Q_0–Q_3) for both the 2010 Maule and 2011 Tohoku earthquakes assuming the depth of 20 km. The lowest values correspond to the Q_0 quality factors ($M_{rr} = 1.06 \times 10^{22}$ Nm for 2010 Maule; $M_{rr} = 1.70 \times 10^{22}$ Nm for 2011 Tohoku) and the highest values correspond to the Q_2 quality factors ($M_{rr} = 1.11 \times 10^{22}$ for 2010 Maule; $M_{rr} = 1.77 \times 10^{22}$ for 2011 Tohoku). The spans of the

remaining two CMT components are within the confidence intervals. The trade-off between the quality factors and M_{rr} is demonstrated in Fig. 6.3. One can clearly recognize that an increase of the M_{rr} component is connected with decreases of the quality factors and the "minima valleys" are shallow. Since the trade-off between the CMT and quality factors complicated the joint Q-CMT inversion although relatively long records were utilized, we will continue with the CMT inversion of short records fixing the quality factors.

6.4 CMT inversion from short time series for fixed quality factor sets

We will demonstrate now that relatively short SG records can be employed to obtain reasonable low-frequency CMT parameters provided the quality factor set is fixed on "reasonable" values. From the point of view of mode-amplitude attenuation with time, the optimal length of a signal to determine the amplitude of a mode is given by its Q multiplied by half of the period (Dahlen, 1982). Therefore, when all studied modes are used in the inversions together, it is important to employ signals where neither of the modes is too much attenuated. This is the reason why we used only 60 hr-long signals; the Hann taper and Fourier transform were applied to the time series starting again two hours after the earthquake-origin time. In principle, even shorter records could be employed but too short time series would not lead to narrow spectral peaks and an approach in the time domain would have to be applied (Tanimoto et al., 2012).

We have inverted three "sensitive" components of the moment tensor M_{rr}, $(M_{\vartheta\vartheta} - M_{\varphi\varphi})$ and $M_{\vartheta\varphi}$ again from the L_2-inversion with variable source depth. A depth-grid search with 1-km stepping has been applied. The results of inversion are shown in Fig. 6.4. For the 2011 Tohoku earthquake all inversions yield better misfit than the reference Global CMT solution with the PREM Q-values, i.e., the re-evaluation of the CMT components plays a substantial role in the misfit reduction. Moreover, our new re-evaluation of the modal quality factors results in further misfit improvement.

	M_{rr} [10^{22} Nm]	$(M_{\vartheta\vartheta} - M_{\varphi\varphi})/2$ [10^{22} Nm]	$M_{\vartheta\varphi}$ [10^{22} Nm]
2010 Maule			
Q_0	1.09	0.50	-0.11
Q_1	1.10	0.50	-0.11
Q_2	1.13	0.53	-0.13
Q_3	1.11	0.54	-0.15
2011 Tohoku			
Q_0	1.73	0.74	-0.54
Q_1	1.73	0.72	-0.53
Q_2	1.78	0.78	-0.53
Q_3	1.75	0.79	-0.51

Table 6.4: Components of the inverted CMT located in 20-km depth from 60-hrs-long records.

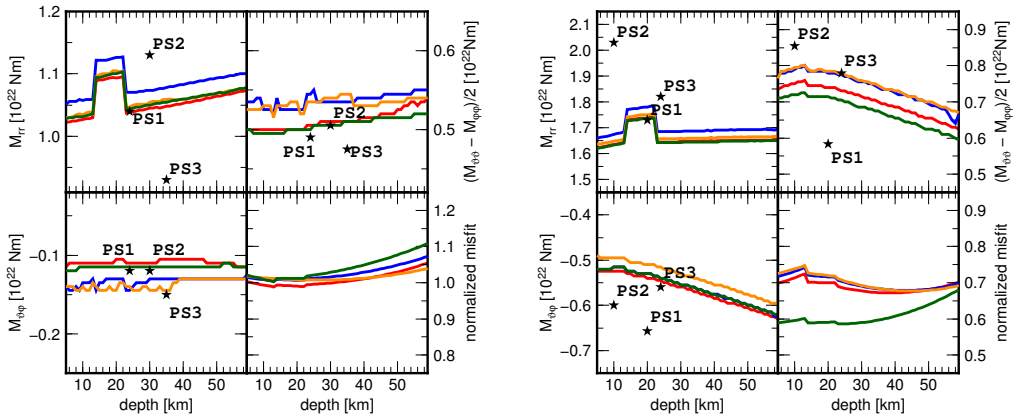

Figure 6.4: Dependence of the M_{rr}, $(M_{\vartheta\vartheta} - M_{\varphi\varphi})/2$ and $M_{\vartheta\varphi}$ components of the centroid moment tensor on the centroid depth obtained from the inversion of vertical acceleration of the spheroidal modes up to 1 mHz for four sets of Q (red Q_0, green Q_1, blue Q_2, orange Q_3). The left (right) panel is for the 2010 Maule (2011 Tohoku) earthquake. Stars denote published point-source solutions: Global CMT solutions (Ekström and Nettles, 2010; Nettles et al., 2011) (PS1), USGS CMT solutions (Maule[1]; Tohoku: Polet and Thio, 2011) (PS2), USGS Wphase solutions (Maule[2]; Tohoku: Duputel et al., 2011) (PS3). The last panel shows the relative misfits of inversions as functions of depth normalized by the misfits of the solution PS1 calculated for the PREM quality factors.

However, the misfits for the 2010 Maule earthquake were not improved. The probable reason is that the fit of the mode ${}_0S_4$ in the case of the 2010 Maule earthquake is poor for any choice of the quality factors and most of the misfit is thus created by this mode as shown in Fig. 6.5. The source of this misfit remains unclear but comparing Figs. 6.2 and 6.5 one can see that the mode ${}_0S_4$ misfit is lower for shorter time windows. The dependence of the misfit on source depth is rather weak up to 30 km and it gets worse for higher depths for both earthquakes. In principle, it confirms the already published results showing that the centroid was located at shallow depths. The values for the centroid depth 20 km are summarized in Table 6.4; they are in good agreement with the values in Table 6.3.

The inversion of M_{rr} from the rather short 60-hr signal is only slightly influenced by considered choices of quality factors, and the resultant differences are smaller than differences of the published CMT solutions that are used here for comparison. The Global CMT solution PS1 yields the M_{rr} component in very good agreement with our inversion. This agreement confirms the analyses of frequency dependence of the scalar moment showing that there were no slow components of the two studied earthquake sources (Tanimoto et al., 2012; Okal, 2013). Moreover, there is a good agreement with the independent results of Zábranová et al. (2012) where the value of M_{rr} was obtained directly from the radial modes. Note that M_{rr} is clearly depth-dependent since it is influenced mainly by the shear-modulus profile. The moment-tensor-diagonal term $(M_{\vartheta\vartheta} - M_{\varphi\varphi})/2$ as well as the $M_{\vartheta\varphi}$ component are determined well for all the studied quality factor sets. It is of interest that the results of inversions of these two components are almost independent of the choice of the quality factors, and they exhibit sensitivity to the centroid depth for the 2011 Tohoku earthquake.

[1] http://earthquake.usgs.gov/earthquakes/eqinthenews/2010/us2010tfan/neic_tfan_cmt.php
[2] http://earthquake.usgs.gov/earthquakes/eqinthenews/2010/us2010tfan/neic_tfan_wmt.php

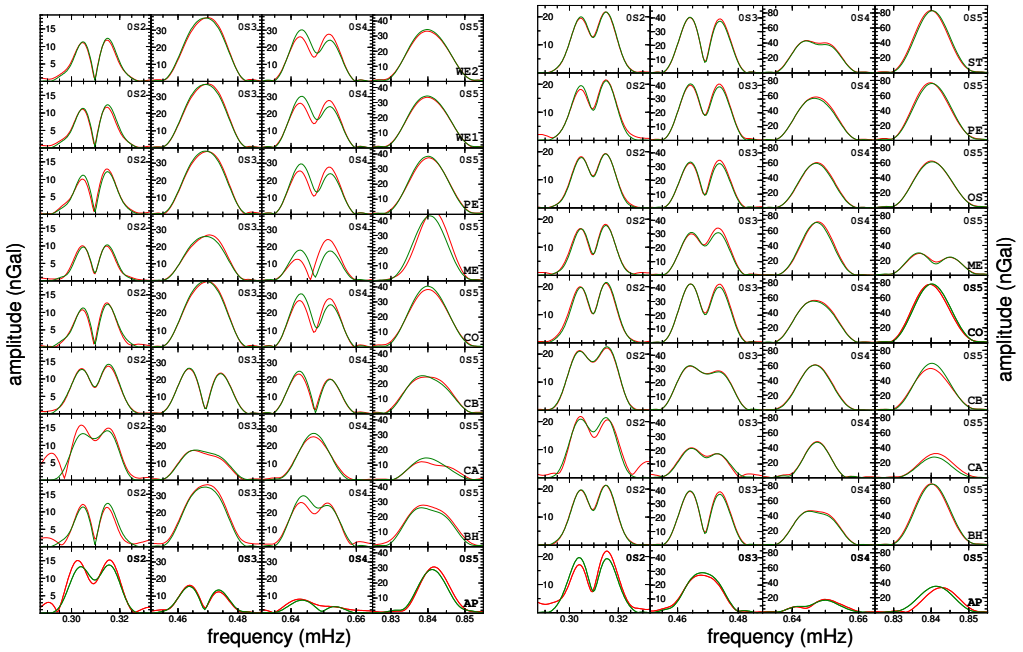

Figure 6.5: Vertical acceleration amplitude spectra of the studied modes from the SG data (red) and synthetics (green) after the 2010 Maule (left panel) and the 2011 Tohoku (right panel) earthquakes. The synthetic signal was calculated for the optimal CMT solution at the depth 20 km (10 km) for the Maule (Tohoku) earthquake when the quality factors were fixed at the Q_1 values from Table 6.2. A Hann filter and Fourier transform were applied to the time series of 60-hrs length starting 2 hrs after the origin times and averaged by the length of the time window.

Fig. 6.6 shows modal-amplitude attenuations with shifts Δt of different time windows (last column in Table 6.3) applied to the superconducting-gravimeter and synthetic data after the 2011 Tohoku earthquake for mechanisms shown in Table 6.4. Deviations of the real data from the synthetic curves appear at "critical-time shifts" when modal amplitudes are so small that the role of noise in the signal becomes substantial. Combining these "critical-time shifts" for data from fifteen records with the used lengths of time windows, one can clearly see that maximal length of the signal undisturbed by the noise is only about 200 hrs for the modes ${}_0S_4$ and ${}_0S_5$ and 280 hrs for the modes ${}_0S_3$ and ${}_0S_2$. These numbers are only illustrative for this particular earthquake as signal/noise ratio depends on earthquake parameters and the station quality. Nevertheless, we think that they represent typical maximal lengths of the signals from the GGP network that can be used for individual modes after megathrust events. Naturally, one can omit "more noisy" stations to obtain an agreement between data and the synthetics for longer times. This figure clearly demonstrates that applications of very long records, used to determine quality factors of individual singlets, can be affected by noise. On the other hand, if we do not deal with clear separation of multiplets into singlets, e.g., when only the low-frequency components of the CMT are determined, relatively short records are sufficient and they have excellent signal/noise ratio.

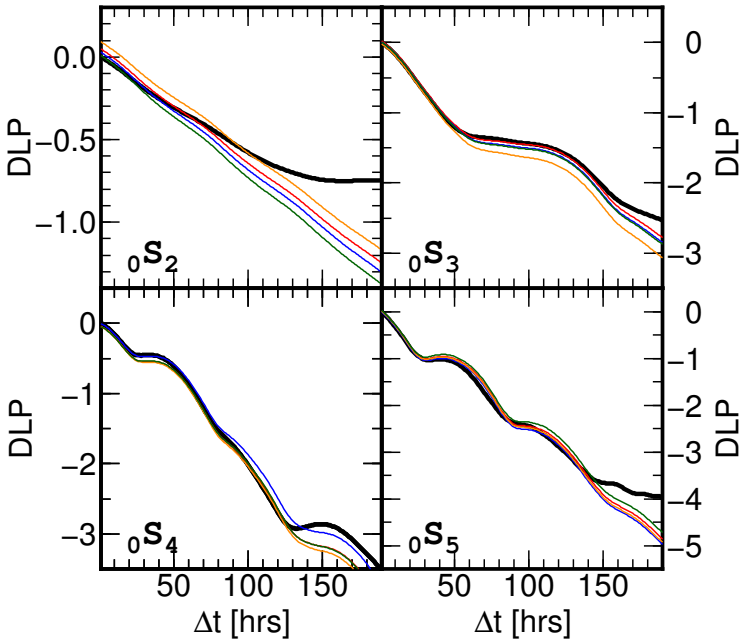

Figure 6.6: Decadic logarithm of the powers (DLP) of the studied modes (integral over narrow frequency range covering all singlets for each mode) with time shifts of time windows applied to the data (black lines) and synthetic signals after the 2011 Tohoku earthquake calculated for the four sets of quality factors (red Q_0, green Q_1, blue Q_2, orange Q_3) and for the CMT values from Table 6.4. All powers are normalized by the powers of data for the time shifts $\Delta t = 0$, i.e. time windows starting 2 hrs after the origin time. Lengths of time windows are written in the last column of Table 6.2. The slope of the curves for synthetic data corresponds to the values of the quality factors. Since the modal multiplets consist of several singlets with slightly different frequencies, the curves are oscillating.

6.5 Conclusions

In several studies (e.g., Okal and Stein, 2009; Okal et al., 2012; Okal, 2013; Tanimoto and Ji, 2010; Tanimoto et al., 2012) ultralong-period normal modes were employed to determine only one low-frequency source parameter of giant earthquakes—the scalar moment M_0—assuming double-couple focal mechanism and fixing the three remaining parameters (dip, strike and rake) by means of values chosen a priori from independent studies. It is well known that there is a trade-off between these parameters; the choice of the dip, strike and rake thus also influences the obtained value of the scalar moment M_0. We demonstrated here the three low-frequency components—M_{rr}, $(M_{\vartheta\vartheta} - M_{\varphi\varphi})/2$ and $M_{\vartheta\varphi}$—can be obtained from SG records after the 2010 Maule and 2011 Tohoku earthquakes assuming that the isotropic component of the CMT is negligible, and dealt with their trade-off with the quality factors of the modes. For shallow earthquakes sensitivity of data to the two remaining components—$M_{r\vartheta}$ and $M_{r\varphi}$—is very weak, these components cannot thus be inverted from the used data, and the results are independent on their choice made a priori (cf. Dziewonski et al., 1981; Ferreira and Woodhouse, 2006; Bukchin et al., 2010; Bogiatzis and Ishii, 2014).

We first performed inversion of quality factors jointly with the three studied CMT components from long records of optimal lengths to obtain amplitudes for each mode (last column in Table 6.2). The resulted modal quality factors are in good agreement with the PREM values and the results published by Deuss et al. (2013), however, they differ more from the results by Tanimoto et al. (2012). We then inverted the CMT components fixing the quality factors on these published values. The resultant span of the CMT values is smaller than mutual differencies of the Global CMT, USGS CMT and USGS Wphase solutions.

The question thus arises whether it is necessary to use such long records. We thus finally employed only 60-hrs long records and performed again the CMT inversions for the fixed four quality factor sets shown in Table 6.2. The best solutions for each quality-factor set are summarized in Table 6.4. They can be considered as the low-frequency estimates of the CMT components independent of previous results obtained in higher frequency ranges. The optimal centroid depth were located into shallow depths and the differences of the obtained inversion results are again smaller than the mutual differences of the published aganecy CMT solutions. Problem of proper determination of the modal quality factors in inversion procedures of the low-frequency CMT of giant earthquakes utilizing relatively short records can thus be omitted and the inversion can be, in principle, routinely performed for any of the studied quality-factor sets.

Acknowledgments

We thank F. Gallovič for long, inspiring and fruitful discussions, J. Zahradník, and L. Špaček for comments and two anonymous reviewers for constructive reviews. The data were downloaded from the GGP webpage: http://www.eas.slu.edu/GGP/ggphome.html. This research was supported by the Grant Agency of the Czech Republic (GAČR) under the project No. 14-04372S and the LM2010008 project CzechGeo/EPOS.

References

Bogiatzis, P., Ishii, M., 2014. Constraints on the moment tensor of the 2011 Tohoku-Oki earthquake from Earth's free oscillations. *Bull. Seism. Soc. Am.*, 104, 875–884.

Bukchin, B., Clévédé, E., Mostinskiy, A., 2010. Uncertainty of moment tensor determination from surface wave analysis for shallow earthquakes. *J. Seismol.* 14, 601–614.

Dahlen, F.A., 1982. The effect of data windows on the estimation of free oscillation parameters. *Geophys. J. R. Astron. Soc.*, 69, 537–549.

Dahlen, F.A., Sailor, R.V., 1979. Rotational and elliptical splitting of the free oscillations of the Earth. *Geophys. J. R. Astron. Soc.*, 58, 609–623.

Dahlen, F.A., Tromp, J., 1998. *Theoretical Global Seismology.* Princeton University Press, Princeton.

Deuss, A., Ritsema, J., van Hejst, H., 2013. A new catalogue of normal-mode splitting function measurements up to 10 mHz. *Geophys. J. Int.*, 193, 920–937.

Ding, H., Shen, W.B., 2013. Determination of the complex frequencies for the normal modes below 1mHz after the 2010 Maule and 2011 Tohoku earthquakes. *Annals Geophys.* 56, S0563, doi:10.4401/ag-6400.

Duputel, Z., Rivera, L., Fukahata, Y., Kanamori, H., 2012. Uncertainty estimates for seismic source inversions. *Geophys. J. Int.*, 190, 1243–1256.

Duputel, Z., Rivera, L., Kanamori, H., Hayes, G.P., Hirshorn, B., Weinstein, S., 2011. Real-time W phase inversion during the 2011 off the Pacific coast of Tohoku earthquake. *Earth Planets Space*, 63, 535–539.

Dziewonski, A.M., Andersen, D.L., 1981. Preliminary reference Earth model. *Phys. Earth Planet. Inter.*, 25, 297–356.

Dziewonski, A.M., Chou, T.A., Woodhouse, J.H., 1981. Determination of earthquake source parameters from waveform data for studies of global and regional seismicity. *J. Geophys. Res.*, 86, 2825–2852.

Ekström, G., Nettles, M., 2010.
http://earthquake.usgs.gov/earthquakes/eqinthenews/2010/us2010tfan/neic_tfan_cmt.php

Ferreira, A.M.G., d'Oreye, N.F., Woodhouse, J.H., Zürn, W., 2006. Comparison of fluid tiltmeter data with long-period seismograms: Surface waves and Earth's free oscillations. *J. Geophys. Res.*, 111, B11307, doi: 10.1029/2006JB004311.

Ferreira, A.M.G., Woodhouse, J.H., 2006. Long-period seismic source inversions using global tomographic models. *Geophys. J. Int.*, 166, 1178–1192.

He, X., Tromp, J., 1996. Normal-mode constraints on the structure of the Earth. *J. Geophys. Res.*, 101, 20053–20082.

Hinderer, J., Crossley, D., Warbuton, R.J., 2007. Gravimetric methods - Superconducting gravity meters. In: Herring T. (Ed.), *Treatise on Geophysics*, 65–122.

Lambotte, S., Rivera, L., Hinderer, J., 2007. Constraining the overall kinematics of the 2004 Sumatra and the 2005 Nias earthquakes using the Earth's gravest free oscillations. *Bull. Seism. Soc. Am.*, 97, S128–S138.

Nettles, M., Ekström, G., Koss, H.C., 2011. Real-time W phase inversion during the 2011 off the Pacific coast of Tohoku earthquake. *Earth Planets Space*, 63, 519–523.

Okal, E., 2013. From 3-Hz P waves to ${}_0S_2$: No evidence of a slow component to the source of the 2011 Tohoku earthquake. *Pure Appl. Geophys.*, 170, 963–973.

Okal, E.A., Hongsresawat, S., Stein, S., 2012. Split-mode evidence for no ultra-slow component to the source of the 2010 Maule, Chile, earthquake. *Bull. Seism. Soc. Am.*, 102, 391–397.

Okal, E.A., Stein, S., 2009. Observations of ultra-long period normal modes from the 2004 Sumatra-Andaman earthquake. *Phys. Earth Planet. Inter.*, 175, 53–62.

Polet, J., Thio, H.K., 2011. Centroid-moment-tensor analysis of the 2011 off the Pacific coast of Tohoku Earthquake and its larger foreshocks and aftershocks. *Earth Planets Space*, 63, 519–523.

Roult, G., Rosat, S., Clévédé, E., 2006. New determinations of Q quality factors and eigenfrequencies for the whole set of singlets of the Earth's normal modes ${}_0S_0$, ${}_0S_2$, ${}_0S_3$ and ${}_2S_1$ using superconducting gravimeter data from the GGP network. *J. Geod.,* 41, 345–357.

Tanimoto, T., Ji, C., 2010. Afterslip of the 2010 Chilean earthquake. *Geophys. Res. Lett.*, 37, L22312, doi:10.1029/2010GL045244.

Tanimoto, T., Ji, C., Igarashi, M., 2012. An approach to detect afterslips in giant earthquakes in the normal-mode frequency band. *Geophys. J. Int.*, 190, 1097–1110, doi:10.1111/j.1365-246X.2012.05524.x

Valentine, A.P., Trampert, J., 2012. Assessing the uncertainties on seismic source parameters: Towards realistic error estimates for centroid-moment-tensor determinations. *Phys. Earth Planet. Inter.*, 210–211, 36–49.

Zábranová, E., Hanyk, L., Matyska, C., 2009. Matrix pseudospectral method for elastic tides modeling. In: Holota P. (Ed.), *Mission and Passion: Science*. Czech National Committee of Geodesy and Geophysics, Prague, 243–260.

Zábranová, E., Matyska, C., Hanyk L., Pálinkáš, V., 2012. Constraints on the centroid moment tensors of the 2010 Maule and 2011 Tohoku earthquakes from radial modes. *Geophys. Res. Lett.*, 39, L18302, doi:10.1029/2012GL052850.

Conclusions and perspectives

In the methodological part of this thesis we have demonstrated that the system of partial differential equations that describes the free oscillations of the Earth can be decomposed into the ordinary differential equations by spherical harmonic analysis and directly discretized by means of finite-difference schemes with pseudospectral accuracy. The original problem can thus be transformed to a series of matrix eigenvalue problems that can be solved by standard numerical routines. Using numerical libraries for matrix spectral analysis, the eigenfunctions and eigenfrequencies of the fundamental mode and corresponding overtones are simultaneously obtained and a high accuracy up to a discretization limit is achieved. Eigenfrequencies and eigenfunctions calculated from these discretized systems perfectly agree with those obtained from the classical method, as represented by the Mineos software package based on Runge-Kutta integration techniques.

In this decade, three megathrust events occurred (2010 Maule, 2011 Tohoku, 2012 Sumatra double event) that were also recorded by the network of superconducting gravimeters within the Global Geodynamic Project. We have analyzed their records and showed that the level of noise is sufficiently low for the gravest spheroidal and radial modes. We employed these data to source mechanism inversions to address the question, whether the methods routinely used to estimate centroid-moment-tensor solutions are suitable to get low-frequency limits of the moment tensor.

Since the data are compared with synthetic accelerograms, the knowledge of quality factors is crucial. Surprisingly, there is still rather high uncertainty in the published quality factors. Their direct estimates for the spheroidal modes are complicated due to multiplet splitting which causes rather complex amplitude decrease. For this reason we have decided to perform source inversions simultaneously with quality-factors determination. Although the joint structural and source inversion is, in general, a complicated non-linear problem, the advantage of the inversion in sub-mHz frequency range is a small number of inverted parameters. We have introduced an iterative procedure, where in the first step the quality factors are fixed and the source parameters are determined, whereas in the next step the source mechanism is fixed and quality factors are re-evaluated. This method converges quite fast and yields both the quality factors of the individual modes and the low-frequency estimates of the three moment-tensor components. However, very long records to obtain stable solutions of these joint inversions are needed.

We compared our results with those provided by the three agency solutions. The GCMT Project preferred solution was obtained using 8.5-hr-long seismograms from about a hundred of stations of the GSN filtered between 300 and 500 s (Nettles et al., 2011). In the GCMT Project approach, the moment tensor and source centroid are estimated by matching observed long-period three-component seismograms to synthetic waveforms calculated by summation of the Earth normal modes. The

USGS method used to compute the CMTs is based on the formulas by Dziewonski et al. (1981), and they are also used by the GCMT group, but input waveforms are filtered from 130 to 330 s (Polet and Thio, 2011). The third agency solution is based on the real-time W-phase inversions that exploit the long-period content of the broadband seismic record (200–1000 s) preceding the arrival of the surface waves (Duputel et al., 2011). The best agreement of our results is with the Harvard GCMT solution, probably due to the applied lower frequency range. However, the differences between our results and GCMT solutions are not negligible, which points to the problem of source-solutions robustness in the low-frequency range that was mentioned above.

Special attention was paid to the radial modes, where the inversion is quite simple as these modes are generated by only the M_{rr}-component of the moment tensor and the quality factors of these modes can be directly determined from changes of modal amplitudes with time since there is no splitting. Moreover, dependence of radial-mode amplitudes on geographic position of an observer is very weak and thus the data from different stations can be averaged, which yields robust results obtained from the observations of the ${}_0S_0$ and ${}_1S_0$ modes.

We believe that our approach is applicable to various problems that could be solved in future. Let us mention three of them:

1. If we consider the quality factors of the modes to be known with sufficient accuracy, the source inversions can be performed from rather short records as demonstrated in this thesis. This fact opens a space for creating routine procedures based on superconducting-gravimeter data that could be an additional product of the GGP.

2. The upper limit of modal summations is limited only by a resolution of the Chebyshev grids and, consequently, by dimensions of the obtained matrices that enter into the numerical eigenanalyses. The potential frequency range of our numerical method can thus continuously increase with increasing software and hardware power. Moreover, further development of our method should enable us to perform co-seismic modeling by means of modal summations up to high degrees and orders as a complement to common analytical formulas for the homogenous half-space by Okada (1992). Geodetic GNSS data employment could thus help to discriminate between finite-source models.

3. The structural models of the planets and moons in the Solar System are still poorly constrained by available data. Our numerical approach is very efficient in the studies when frequency dependence of the structural parameters plays a minor role and may be neglected. Therefore, it is suitable, e.g., for a fast evaluation of the dependencies of eigenfrequencies on structural parameters like depths of major interfaces (core boundaries etc.) of these bodies.

Bibliography

Agnew D.C., Berger J., Buland R., Farrell W.E. and Gilbert J.F., 1976. International deployment of accelerometers: A network for very long period seismology. *Eos Trans. AGU*, **57**, 180–188.

Agnew D.C., Berger J., Farrell W.E., Gilbert J.F., Masters G. and Miller D., 1986. Project IDA: A decade in review. *Eos Trans. AGU*, **67**, 203–212.

Agnew, D. C., 2007. Earth tides, in *Treatise on Geophysics*, Vol. 3: Geodesy, ed. by Herring T., Elsevier, Amsterdam etc., pp. 163–195.

Backus G. and Gilbert F., 1961. The rotational splitting of the free oscillations of the Earth. *Proc. Nat. Acad. Sci.*, **47**, 362–371.

Banerjee P., Pollitz F.F. and Biirgmann R., 2005. The size and duration of the Sumatra- Andaman earthquake from far-field static offsets. *Science*, **308**, 1769–1772.

Bogiatzis P. and Ishii M., 2014. Constraints on the moment tensor of the 2011 Tohoku-Oki earthquake from Earth's free oscillations. *Bull. Seism. Soc. Am.*, **104**, 875–884.

Braitenberg C. and Zadro M., 2007. Comparative analysis of free oscillations generated by the Sumatra-Andaman Islands 2004 and the Chile 1960 earthquakes. *Bull. Seism. Soc. Am.*, **97**, S6–S17.

Buland R., Berger J. and Gilbert F., 1979. Observations from the IDA network of attenuation and splitting during a recent earthquake. *Nature*, **277**, 358–362.

Crossley D.J., 1992. Eigensolutions and seismic excitation of the Slichter mode triplet for a fully rotating Earth model. *Eos Trans. AGU*, **73**, 60.

Crossley D., Hinderer J., Casula G., Francis O., Hsu H.-T., Imanishi Y., Jentzsch G., Kaarianen J., Merriam J., Meurers B., Neumeyer J., Richter B., Shibuya K., Sato T. and van Dam T., 1999. Network of superconducting gravimeters benefits a number of disciplines. *Eos Trans. AGU*, **80**, 121–126.

Crossley D. and Hinderer J., 2009. A review of the GGP network and scientific challenges. *J. Geodyn.*, **48**, 299–304. doi:10.1016/j.jog.2009.09.019

Dahlen F.A., 1968. The normal modes of a rotating, elliptical Earth. *Geophys. J. R. Astron. Soc.*, **16**, 329–367.

Dahlen F.A., 1972. Elastic dislocation theory for a self-gravitating elastic configuration with an initial static stress field. *Geophys. J. R. Astron. Soc.*, **28**, 357–383.

Dahlen F.A. and Sailor R.V., 1979. Rotational and elliptical splitting of the free oscillations of the Earth. *Geophys. J. R. Astron. Soc.*, **58**, 609–623. doi: 10.1111/j.1365-246X.1979.tb04797.x

Dahlen F.A. and Tromp J., 1998. *Theoretical Global Seismology*. Princeton University Press, Princeton, New Jersey.

de Groot-Hedlin C.D., 2005. Estimation of the rupture length and velocity of the great Sumatra earthquake of December 26, 2004 using hydroacoustic signals. *Geo-*

phys. Res. Lett., **32**, L11303. doi:10.1029/2005GL022695

Ding H. and Shen W., 2013a. Search for the Slichter modes based on a new method: Optimal sequence estimation. *J. Geophys. Res. Solid Earth*, **118**, 5018–5029. doi:10.1002/jgrb.50344

Ding H. and Shen W., 2013b. Determination of the complex frequencies for the normal modes below 1 mHz after the 2010 Maule and 2011 Tohoku earthquakes. *Annals of Geophysics*, **56**, S0563. doi:10.4401/ag-6400

Duputel Z., Rivera L., Kanamori H., Hayes G.P., Hirshorn B. and Weinstein S., 2011. Real-time W phase inversion during the 2011 off the Pacific coast of Tohoku earthquake. *Earth Planets Space*, **63**, 535–539.

Durek J.J. and Ekström G., 1996. A radial model of anelasticity consistent with long period surface wave attenuation. *Bull. Seism. Soc. Am.*, **86**, 144–158.

Dziewonski A.M. and Gilbert F., 1971. Solidity of the inner core of the Earth inferred from normal mode observations. *Nature*, **234**, 465–466.

Dziewonski A.M. and Sailor R.V., 1976. Comments on 'The Correction of Great Circular Surface Wave Phase Velocity Measurements From the Rotation and Ellipticity of the Earth' by F. A. Dahlen *J. Geophys. Res.*, **81**, 4947–4950.

Dziewonski A.M. and Anderson D.L., 1981. Preliminary reference Earth model. *Phys. Earth Planet. Inter.*, **25**, 297–356.

Dziewonski A.M., Chou T.-A. and Woodhouse J.H., 1981. Determination of earthquake source parameters from waveform data for studies of global and regional seismicity. *J. Geophys. Res.*, **86**, 2825–2852.

Ekström, G. and Nettles M., 2010.
http://earthquake.usgs.gov/earthquakes/eqinthenews/2010/us2010tfan/neic_tfan_cmt.php

Fang M., 1998. Static deformation of the outer core, in *Dynamics of the Ice Age Earth: A Modern Perspective*, ed. by Wu P., Trans Tech Publ., Zürich, pp. 155–190.

Ferreira A.M.G., d'Oreye N.F., Woodhouse J.H. and Zürn W., 2006. Comparison of fluid tiltmeter data with long-period seismograms: Surface waves and Earth's free oscillations. *J. Geophys. Res.*, bf 111, B11307. doi: 10.1029/2006JB004311

Fornberg B., 1996. *Practical Guide to Pseudospectral Methods*, Cambridge University Press, New York.

Freybourger M., Hinderer J. and Trampert J., 1997. Comparative study of superconducting gravimeters and broadband seismometers STS-1/Z in sub-seismic frequency bands. *Phys. Earth Planet. Inter.*, **101**, 203–217.

Gahalaut V.K., Subrahmanyam C., Kundu B., Catherine J.K. and Ambikapathy A., 2010. Slow rupture in Andaman during 2004 Sumatra-Andaman earthquake: a probable consequence of subduction of 90° E ridge. *Geophys. J. Int.*, **180**, 1181–1186.

Gilbert F. and Dziewonski A.M., 1975. An application of normal mode theory to the retrieval of structural parameters and source mechanisms from seismic spectra. *Phil. Trans. R. Soc. Lond.*, , Series A, **278**, 187–269.

Grinfeld P. and Wisdom J., 2010. The effect of phase transformations at the inner core boundary on the Slichter modes. *Phys. Earth Planet. Inter.*, **178**, 183–188. doi:10.1016/j.pepi.2009.10.006

Guilbert J., Vergoz J., Schisselé E., Roueff A. and Cansi Y., 2005. Use of hydroacoustic and seismic arrays to observe rupture propagation and source extent of the Mw=9.0 Sumatra earthquake. *Geophys. Res. Lett.*, **32**, L15310.

doi:10.1029/2005GL022966.

Hanyk L., 1999. Viscoelastic response of the Earth: Initial-value approach, *PhD Thesis*, Faculty of Mathematics and Physics, Charles University in Prague. http://geo.mff.cuni.cz/theses.htm

Hanyk L., Matyska C. and Yuen D.A., 2002. Determination of viscoelastic spectra by matrix eigenvalue analysis, in *Ice Sheets, Sea Level and the Dynamic Earth*, ed. by Mitrovica J.X. and Vermeersen B.L.A., Geodynamics Series, 29, AGU, Washington, pp. 257–273.

Hartmann T. and Wenzel H-G., 1995a. The HW95 tidal potential catalogue. *Geophys. Res. Lett.*, **22**, 24, 3553–3556.

Hartmann T. and Wenzel H-G., 1995b. Catalog HW95 of the tide generating potential. *Bull. Inf. Marées Terrestres*, **123**, 9278–9301.

He X. and Tromp J., 1996. Normal-mode constraints on the structure of the Earth. *J. Geophys. Res.*, **101**, 20053–20082.

Hinderer J., Crossley D. and Jensen O., 1995. A search for the Slichter triplet in superconducting gravimeter data. *Phys. Earth Planet. Inter.*, **90**, 183–195.

Hinderer J., Crossley D. and Warbuton R.J., 2007. Gravimetric methods – Superconducting gravity meters, in *Treatise on Geophysics*, Vol. 3: Geodesy, ed. by Herring T., Elsevier, Amsterdam etc., pp. 65–122.

Ishii M., Shearer P.M., Houston H. and Vidale J.E., 2005. Extent, duration and speed of the 2004 Sumatra-Andaman earthquake imaged by the Hi-Net array. *Nature*, **435**, 933–936.

Jekeli Ch., 1989. Earth's external gravity field, in *The Encyclopedia of Solid Earth Geophysics*, ed. by James D.E., VNR, New York, pp. 322–331.

Jobert N., Lévêque J.J. and Roult G., 1978. Evidence of lateral variations from free oscillations and surface waves. *Geophys. Res. Lett.*, **5**, 569–572.

Kanamori H. and Anderson D.L., 1977. Importance of physical dispersion in surface waves and free oscillation problems. *Rev. Geophys. Space Phys.*, **15**, 105–112.

Krüger F. and Ohrnberger M., 2005. Spatio-temporal source characteristics of the 26 December 2004 Sumatra earthquake as imaged by teleseismic broadband arrays. *Geophys. Res. Lett.*, **32**, L24312.

Lawrence J.F. and Wysession M.E., 2005. QLM9: A new radial quality factor (Q_μ) model for the lower mantle. *Earth Planet. Sci. Lett.*, **241**, 962–971. doi:10.1016/j.epsl.2005.10.030

Love A.E.H., 1911. *Some Problems of Geodynamics*, Cambridge University Press, Cambridge.

Martinec Z., 1984. Free oscillations of the Earth. *Travaux Géophysics*, **591**, 117–263.

Masters G., Jordan T.H., Silver P.G. and Gilbert F., 1982. Aspherical Earth structure from fundamental spheroidal mode data. *Nature*, **298**, 609–613.

Masters G. and Gilbert F., 1983. Attenuation in the Earth at low frequencies. *Phil. Trans. R. Soc. Lond.*, **308**, 479–522.

Mitsui Y. and Heki K., 2012. Observation of Earth's free oscillation by dense GPS array: After the 2011 Tohoku megathrust earthquake. *Sci. Rep.*, **2**, 931. doi:10.1038/srep00931

Nettles, M., Ekström G. and Koss H.C., 2011. Centroid-moment-tensor analysis of the 2011 off the Pacific coast of Tohoku earthquake and its larger foreshocks and aftershocks. *Earth Planets Space*, **63**, 519–523.

Okada Y., 1992. Internal deformation due to shear and tensile faults in a half-space. *Bull. Seism. Soc. Am.*, **82**, 1018–1040.

Okal E.A. and Stein S., 2009. Observations of ultra-long period normal modes from the 2004 Sumatra-Andaman earthquake. *Phys. Earth Planet. Inter.*, **175**, 53–62. doi:10.1016/j.pepi.2009.03.002

Park J., Song T.-R.A., Tromp J., Okal E., Stein S., Roult G., Clevede E., Laske G., Kanamori H., Davis P., Berger J., Braitenberg C., van Camp M., Lei X., Sun H., Xu H. and Rosat S., 2005. Earth's free oscillations excited by the 26 December 2004 Sumatra-Andaman earthquake. *Science*, **308**, 1139–1144.

Pekeris C.L. and Jarosch H., 1958. The free oscillations of the Earth, *Contributions in Geophysics in Honor of Beno Gutemberg*, Pergamon Press, London, 171–192.

Polet J. and Thio H.K., 2011. Centroid-moment-tensor analysis of the 2011 off the Pacific coast of Tohoku Earthquake and its larger foreshocks and aftershocks. *Earth Planets Space*, **63**, 519–523.

Rieutord M., 2002. Slichter modes of the Earth revisited. *Phys. Earth Planet. Inter.*, **131**, 269–278.

Rochester M.G. and Peng Z.R., 1993. The Slichter modes of the rotating Earth: a test of the subseismic approximation. *Geophys. J. Int.*, **111**, 575–585.

Rogister Y., 2003. Splitting of seismic-free oscillations and of the Slichter triplet using the normal mode theory of a rotating, ellipsoidal Earth. *Phys. Earth Planet. Inter.*, **140**, 169–182.

Romanowicz B. and Roult G., 1986. First-order asymptotics for the eigenfrequencies of the Earth and application to the retrieval of large-scale lateral variations of structures. *Geophys. J. R. Astron. Soc.*, **87**, 209–239.

Romanowicz B. and Bréger L., 2000. Anomalous splitting of free oscillations; a reevaluation of possible interpretations. *J. Geophys. Res.*, **105**, 21559–21578.

Rosat S., Hinderer J. and Crossley D., 2002. A comparison of the seismic noise levels at various GGP stations. *Bull. Inf. Marées Terrestres*, **135**, 10689–10700.

Rosat S., Hinderer J., Crossley D. and Rivera L., 2003. The search for the Slichter mode: comparison of noise levels of superconducting gravimeters and investigation of a stacking method. *Phys. Earth Planet. Inter.*, **140**, 183–202.

Rosat S., Hinderer J., Crossley D. and Boy J.P., 2004. Performance of superconducting gravimeters from long-period seismology to tides. *J. Geodyn.*, **38**, 461–476.

Rosat S., 2007. Optimal seismic source mechanisms to excite the Slichter mode. *Int. Assoc. of Geod. Symposia*, vol. 130, Dynamic Planet, Cairns, Australia, Springer, Berlin, Heidelberg, New York, pp. 571–577.

Rosat S. and Hinderer J., 2011. Noise levels of superconducting gravimeters: Updated comparison and time stability. *Bull. Seism. Soc. Am.*, **101**, 1233–1241. doi: 10.1785/0120100217

Rosat S. nad Rogister Y., 2012. Excitation of the Slichter mode by collision with a meteoroid or pressure variations at the surface and core boundaries. *Phys. Earth Planet. Inter.*, **190–191**, 25–33. doi:10.1016/j.pepi.2011.10.007

Rosat S., Calvo M., Hinderer J., Riccardi U., Arnoso J. and Zürn W, 2015. Comparison of the performances of different spring and superconducting gravimeters and STS-2 seismometer at the Gravimetric Observatory of Strasbourg, France. *Stud. Geophys. Geod.,* **59**, 58–82. DOI: 10.1007/s11200-014-0830-5

Sailor R.V. and Dziewonski A.M., 1978. Measurements and interpretation of normal mode attenuation. *Geophys. J. R. Astron. Soc.*, **53**, 559–581.

Slichter L.B., 1961. The fundamental free mode of the Earth's inner core. *Proc. Nat. Acad. Sci.*, **47**, 186–190.

Smylie D.E., 1992. The inner core translational triplet and the density near Earth's centre. *Science*, **255**, 1678–1682.

Smylie D.E., Jiang X., Brennan B.J. and Sato K., 1992. Numerical calculation of modes of oscillation of the Earth's core. *Geophys. J. Int.*, **108**, 465–490.

Smylie D.E. and McMillan D.G., 2000. The inner core as a dynamic viscometer. *Phys. Earth Planet. Inter.*, **117**, 71–79.

Tolstoy M. and Bohnenstiehl D.B., 2005. Hydroacoustic constraints on the rupture duration, length, and speed of the great Sumatra-Andaman earthquake. *Seis. Res. Lett.*, **76**, 419–425.

Tromp J., 1993. Support for anisotropy of the Earth's inner core from free oscillations. *Nature*, **366**, 678–681.

Van Camp M., 1999. Measuring seismic normal modes with the GWR C021 superconducting gravimeter. *Phys. Earth Planet. Inter.*, **116**, 81–92.

Vigny C., Simons W.J.F., Abu S., Bamphenyu R., Satirapod C., Choosakul N., Subarya C., Socquet A., Omar K., Abidin H.Z. and Ambrosius B.A.C., 2005. Insight into the 2004 Sumatra-Andaman earthquake from GPS measurements in southeast Asia. *Nature*, **436**, 201–206.

Wahr J.M., 1989. Earth tides, in *The Encyclopedia of Solid Earth Geophysics*, ed. by James D.E., VNR, New York, pp. 359–363.

Wenzel H-G., 1996a. Accuracy assessment for tidal potential catalogues. *Bull. Inf. Marées Terrestres*, **124**, 9394–9416.

Wenzel H-G., 1996b. The nanogal software: Earth tide processing package ETERNA 3.30. *Bull. Inf. Marées Terrestres*, **124**, 9425–9439.

Widmer R., Master G. and Gilbert F., 1991. Spherically symmetric attenuation within the Earth from normal mode data. *Geophys. J. Int.*, **104**, 541–553.

Widmer-Schnidrig R., 2003. What can superconducting gravimeters contribute to normal-mode seismology? *Bull. Seism. Soc. Am.*, **93**, 1370–1380.

Woodhouse J.H. and Dahlen F.A., 1978. The effect of a general aspherid perturbation on the free oscillations of the Earth. *Geophys. J. R. Astron. Soc.*, **53**, 335–354.

Woodhouse J.H., Giardini D. and Li X.D., 1986. Evidence for inner core anisotropy from splitting in free oscillations data. *Geophys. Res. Lett.*, **13**, 1549–1552.

Zábranová E., Hanyk L. and Matyska C., 2009. Matrix pseudospectral method for elastic tides modeling. In: Holota P. (Ed.), *Mission and Passion: Science*. Czech National Committee of Geodesy and Geophysics, Prague, 243–260.

Zábranová E., Matyska C. and Hanyk L., 2012a. Tests of the 2011 Tohoku earthquake source models using free-oscillation data from GOPE. *Stud. Geophys. Geod.,* **56**, 585–594. doi:10.1007/s11200-011-9033-5

Zábranová E., Matyska C., Hanyk L. and Vojtech Pálinkáš, 2012b. Constraints on the centroid moment tensors of the 2010 Maule and 2011 Tohoku earthquakes from radial modes. *Geophys. Res. Lett.*, **39**, L18302. doi:10.1029/2012GL052850

Zábranová E. and Matyska C., 2014. Low-frequency centroid-moment-tensor inversion from superconducting-gravimeter data: The effect of seismic attenuation. *Phys. Earth Planet. Inter.*, **235**, 25–32. doi:10.1016/j.pepi.2014.06.013

Appendix

Analytical solution at the center

In order to obtain the boundary conditions at the center of the Earth model, $r = 0$, we analyze solutions of the ordinary differential equations derived in the previous text by means of power series of the second order and study the behavior of coefficients of these series at the neighborhood of the center. For some cases, several boundary conditions can be derived from the solution at the center of the models. In the previous text we chose a required number of them; the remained unused conditions are then naturally satisfied. Note that this approach is different from the classical treatment where a solution for the homogeneous small sphere surrounding the center is employed (e.g. Crossley, 1975; Martinec, 1984; Dahlen and Tromp, 1998).

Toroidal oscillations

The eigenfunctions W_n decomposed into the power series get the form for $r \to 0$,

$$W_l = a_0 + a_1 r + a_2 r^2 + O(r^3). \tag{A.1}$$

By substitution of this expression into (1.36), we obtain the relation

$$(6 - N)\, a_2 + \frac{2 - N}{r} a_1 - \frac{N a_0}{r^2} = -\frac{\rho_0 \omega^2}{\mu} a_0, \tag{A.2}$$

which has three different branches dependent on the angular degree l. We abbreviate $N = l(l + 1)$.

- $l = 1$ and $N = 2$

Expansion coefficients a_0 and a_2 must be equal to zero to satisfy (A.2). Thus, we have conditions for the zero and second derivatives of toroidal displacement,

$$W_1(0) = W_1''(0) = 0. \tag{A.3}$$

- $l = 2$ and $N = 6$

We obtain conditions for the zero and first derivatives of W_2, since $a_0 = a_1 = 0$,

$$W_2(0) = W_2'(0) = 0. \tag{A.4}$$

- $l > 2$ and $N > 6$

Since $a_0 = a_1 = a_2 = 0$, all derivatives have to vanish in the center,

$$W_l(0) = W_l'(0) = W_l''(0) = 0. \tag{A.5}$$

Radial oscillations

The expansions of the displacement and incremental gravitational potential in the case of $l = 0$ have the form for $r \to 0$,

$$U_0 = a_0 + a_1 r + a_2 r^2 + O(r^3), \tag{A.6}$$
$$F_0 = c_0 + c_1 r + O(r^2). \tag{A.7}$$

By substitution of these expressions into (1.51)–(1.52) and using $g_0(r) = \frac{4}{3}\pi G\rho_0 r$, we obtain the system of equations

$$4\beta a_2 + \left(\frac{16}{3}\pi G\rho_0^2 - \frac{2\beta}{r^2}\right) a_0 = -\rho_0\omega^2 a_0, \tag{A.8}$$
$$c_1 + 4\pi G\rho_0 a_0 = 0, \tag{A.9}$$

which yields $a_0 = 0, c_1 = 0, a_2 = 0$, and results in the conditions

$$U_0(0) = U_0''(0) = F_0'(0) = 0. \tag{A.10}$$

Spheroidal oscillations

In the case of spheroidal oscillations, $l > 0$, we have three eigenfunctions represented by the power-series expansions,

$$U_l = a_0 + a_1 r + a_2 r^2 + O(r^3), \tag{A.11}$$
$$V_l = b_0 + b_1 r + b_2 r^2 + O(r^3), \tag{A.12}$$
$$F_l = c_0 + c_1 r + c_2 r^2 + O(r^3). \tag{A.13}$$

By substitution into the (1.41)–(1.43) and using $g_0(r) = \frac{4}{3}\pi G\rho_0 r$, we obtain the system of equations for $r \to 0$,

$$(4\beta - N\mu)\, a_2 - \frac{N\mu}{r} a_1 + \left(\frac{4}{3}\pi G\rho_0^2 - \frac{2\beta + N\mu}{r^2}\right) a_0 + N\,(\mu + \lambda)\, b_2 +$$
$$+ \frac{2N\mu}{r} b_1 + N\left(\frac{3\mu + \lambda}{r^2} - \frac{4}{3}\pi G\rho_0^2\right) b_0 - \rho_0 c_1 = -\rho_0\omega^2 a_0, \tag{A.14}$$

$$(4\lambda + 6\mu)\, a_2 + \frac{3\lambda + 5\mu}{r} a_1 + \left(\frac{2\beta}{r^2} - \frac{4}{3}\pi G\rho_0^2\right) a_0 +$$
$$+ (6\mu - N\beta)\, b_2 + \frac{2\mu - N\beta}{r} b_1 - \frac{\beta N}{r^2} b_0 - \rho_0 c_1 - \frac{\rho_0}{r} c_0 = -\rho_0\omega^2 b_0, \tag{A.15}$$

$$4\pi G\rho_0 \left(3a_1 + \frac{2}{r} a_0 - N b_1 - \frac{N}{r} b_0\right) +$$
$$+ (6 - N)\, c_2 + \frac{2 - N}{r} c_1 - \frac{N}{r^2} c_0 = 0. \tag{A.16}$$

Similarly as in the case of the toroidal oscillations, we have three different branches.

- $l = 1$ and $N = 2$

From (A.14) we obtain

$$\begin{aligned}
(2\beta + 2\mu)a_0 &= 2(\lambda + 3\mu)b_0 \\
&\Rightarrow a_0 = b_0 \\
-2\mu a_1 + 4\mu b_1 &= 0 \\
&\Rightarrow a_1 = 2b_1 \\
(4\lambda + 6\mu)a_2 - \frac{4}{3}\pi G\rho_0^2 a_0 - (2\lambda - 2\mu)b_2 - \rho_0 c_1 &= -\rho_0\omega^2 a_0
\end{aligned}$$

From (A.14)–(A.15) it follows that

$$\begin{aligned}
2\beta a_0 - 2\beta b_0 &= 0 \\
&\Rightarrow a_0 = b_0 \\
2(3\lambda + 5\mu)b_1 + (2\mu - 2\beta)b_1 - \rho_0 c_0 &= 0 \\
&\Rightarrow b_1 = \frac{\rho_0}{4\beta}c_0 \\
(4\lambda + 6\mu)a_2 - \frac{4}{3}\pi G\rho_0^2 a_0 - (2\lambda - 2\mu)b_2 - \rho_0 c_1 &= -\rho_0\omega^2 a_0
\end{aligned}$$

From (A.16) we get

$$\begin{aligned}
2c_0 &= 0 \\
&\Rightarrow c_0 = 0 \\
4\pi G\rho_0(2a_0 - 2b_0) &= 0 \\
&\Rightarrow a_0 = b_0 \\
4\pi G\rho_0(3a_1 - 2b_1) + 4c_2 &= 0 \\
&\Rightarrow a_1 = -\frac{c_2}{2\pi G\rho_0}
\end{aligned}$$

It follows that $c_0 = 0 \Rightarrow b_1 = 0 \Rightarrow a_1 = 0 \Rightarrow c_2 = 0$, and

$$U_1'(0) = V_1'(0) = F_1(0) = F_1''(0) = 0, \quad U_1(0) = V_1(0). \tag{A.17}$$

For $l = 1$, (A.14) and (A.15) are identical. Thus, we have only one equation constraining the remaining coefficients,

$$\rho_0\left(\omega^2 - \frac{4}{3}\pi G\rho_0\right)a_0 + (4\lambda + 6\mu)a_2 - (2\lambda - 2\mu)b_2 - \rho_0 c_1 = 0.$$

- $l = 2$ and $N = 6$

From (A.14) we obtain

$$\begin{aligned}
(-2\lambda - 10\mu)a_0 + (6\lambda + 18\mu)b_0 &= 0 \\
&\Rightarrow a_0 = b_0 = 0 \\
-6\mu a_1 + 12\mu b_1 &= 0 \\
&\Rightarrow a_1 = 2b_1 \\
(4\lambda + 2\mu)a_2 + 6(\mu + \lambda)b_2 - \rho_0 c_1 &= 0
\end{aligned}$$

From (A.14)–(A.15) it follows that

$$\begin{aligned} a_0 = b_0 &= 0 \\ (3\lambda+5\mu)2b_1 + (2\mu - 6\beta)b_1 - \rho_0 c_0 &= 0 \\ &\Rightarrow c_0 = 0 \\ (4\lambda+6\mu)a_2 - 6(\mu+\lambda)b_2 - \rho_0 c_1 &= 0 \end{aligned}$$

From (A.16) we get

$$\begin{aligned} c_0 &= 0 \\ c_1 &= 0 \\ a_1 &= 2b_1 \end{aligned}$$

We get $a_0 = b_0 = c_0 = c_1 = 0$, b_1 and c_2 can be arbitrary and $a_1 = 2b_1$, consequently $a_2 = b_2 = 0$, and, finally,

$$U_2(0) = U_2''(0) = V_2(0) = V_2''(0) = F_2(0) = F_2''(0) = 0,\ U_2'(0) = 2V_2'(0). \quad \text{(A.18)}$$

- $l > 2$ and $N > 6$

From (A.14) we obtain

$$\begin{aligned} -(2\beta+\mu N)a_0 + (3\mu+\lambda)Nb_0 &= 0 \\ \overset{b_0=\frac{2}{N}a_0}{\Longrightarrow} a_0 &= b_0 = 0, \text{ if } \mu > 0 \\ -\mu N a_1 + 2\mu N b_1 &= 0 \\ \Longrightarrow a_1 &= 2b_1, \text{ if } \mu > 0 \\ (4\beta - \mu N)a_2 + \frac{4}{3}\pi G\rho_0^2(a_0 - Nb_0) - (\lambda-\mu)Nb_2 - \rho_0 c_1 &= -\rho_0\omega^2 a_0 \quad \text{(A.19)} \end{aligned}$$

From (A.14)–(A.15) it follows that

$$\begin{aligned} -\beta N b_0 + 2\beta a_0 &= 0 \\ \Longrightarrow a_0 &= \frac{N}{2}b_0 \\ (2\mu - \beta N)b_1 + (3\lambda+5\mu)a_1 - \rho_0 c_0 &= 0 \\ \overset{c_0=0,\ a_1=2b_1}{\Longrightarrow} a_1 &= b_1 = 0 \\ (6\mu - \beta N)b_2 + (4\lambda+6\mu)a_2 - \frac{4}{3}\pi G\rho_0^2 a_0 - \rho_0 c_1 &= -\rho_0\omega^2 b_0 \quad \text{(A.20)} \end{aligned}$$

From (A.16) we get

$$\begin{aligned} c_0 &= 0 \\ (2-N)c_1 + (2a_0 - Nb_0)4\pi G\rho_0 &= 0 \\ \overset{a_0=\frac{N}{2}b_0}{\Longrightarrow} c_1 &= 0, \text{if } \mu > 0 \\ (6-N)c_2 + (3a_1 - Nb_1)4\pi G\rho_0 &= 0 \\ \overset{a_1=b_1=0}{\Longrightarrow} (c_2 + 4\pi G\rho_0 b_1) &= 0, \text{if } \mu > 0 \end{aligned}$$

We get $a_0 = a_1 = b_0 = b_1 = c_0 = c_1 = c_2 = 0$ and from (A.19)–(A.20) we obtain $a_2 = b_2 = 0$. Thus, finally,

$$U_n(0) = U_n'(0) = U_n''(0) = V_n(0) = V_n'(0) = V_n''(0) = F_n(0) = F_n'(0) = F_n''(0) = 0. \quad \text{(A.21)}$$

List of tables

List of abbreviations

CMB	core-mantle boundary
CMT	centroid moment tensor
CW	Chandler wobble
FCN	free core nutation
FICN	free inner-core nutation
GCMT	Global Centroid Moment Tensor (Project)
GGP	Global Geodynamics Project
GOPE	Geodetic Observatory Pecný
ICB	inner-core boundary
IDA	International Deployment of Accelerometers
ODE	ordinary differential equation
PDE	partial differential equation
PREM	Preliminary Reference Earth Model
SG	superconducting gravimeter
SNREI	spherical non-rotating elastic isotropic (model)
USGS	United States Geological Survey

List of symbols

$a(\boldsymbol{x}, t)$	acceleration in the direction $\boldsymbol{\nu}$
a	splitting parameter
${}_n\mathbf{A}_l$	amplitude of excitation
α_2	second-order Coriolis correction
α_{ij}	weight-matrix elements
b	splitting parameter
β	abbreviation for $\lambda + 2\mu$
β_{ij}	weight matrix elements
c	splitting parameter
$(\boldsymbol{e}_r, \boldsymbol{e}_\vartheta, \boldsymbol{e}_{phi})$	unit spherical vector basis
ϵ	hydrostatic ellipticity
ϵ_R	hydrostatic surface ellipticity
$\boldsymbol{\varepsilon}$	strain tensor
$\boldsymbol{\varepsilon}_m$	strain tensor corresponding to the m-th singlet
f	frequency
$\boldsymbol{f}$	forcing term (1.29)
F_{lm}	spherical harmonic coefficients of φ
G	Newton gravitational constant
g_0, g	gravitational acceleration
γ_2	second-order Coriolis correction
γ_{ij}	weight matrix elements
h_l	tidal Love number
I	moment of inertia
$\mathbf{I}$	identity matrix
k_l	tidal Love number
K	number of model layers
κ	incompressibility modulus, $\kappa = \lambda + \frac{2}{3}\mu$
l	angular degree
l_l	tidal Love number
λ	elastic Lamé parameter
m	azimuthal order
M	number of grid points within a layer, mass of the Earth model
M_0	scalar moment tensor
$\mathbf{M}$, M_{rr}, $M_{r\vartheta}$, ...	moment tensor and its spherical components
μ	elastic Lamé parameter (shear modulus)
n	overtone number
$\boldsymbol{n}$	unit normal vector
N	abbreviation for $l(l+1)$

$\boldsymbol{\nu}$	polarization of the accelerometer
π	Ludolph's number
Q	quality factor, abbreviation for auxiliary coefficients Q_{lm} (1.33)
Q_κ	bulk quality factor
Q_μ	shear quality factor
r	radius
r_m	complex receiver scalar
R	surface radius
R_{CMB}	radius of the core-mantle boundary
R_{ICB}	radius of the inner-core boundary
ρ_0, ρ	reference density
${}_n\mathrm{S}_l$	spheroidal mode
s_m	complex source scalar
$\boldsymbol{S}_{lm}^{(0)}, \boldsymbol{S}_{lm}^{(-1)}, \boldsymbol{S}_{lm}^{(1)}$	vector spherical harmonic functions
t	time
Δt	time increment
T	period
${}_n\mathrm{T}_l$	toroidal mode
$\mathcal{T}$	kinetic energy
$\boldsymbol{T}_r$, T_{rr}, $T_{r\vartheta}$, $T_{r\phi}$	traction vector and its spherical components
$\boldsymbol{\tau}_0$, $\boldsymbol{\tau}$	Cauchy stress tensor
$\boldsymbol{u}, u_r, u_\vartheta, u_\phi$	displacement vector and its spherical components
U_{lm}, V_{lm}, W_{lm}	spherical harmonic coefficients of $\boldsymbol{u}$
v_p	P-wave velocity
v_s	S-wave velocity
$\boldsymbol{x}$	position vector of the receiver
$\boldsymbol{x}_s$	position vector of the source
Y_{lm}, Y_l	scalar spherical harmonic functions
$\boldsymbol{y} = (U, V, F, W)^{\mathrm{T}}$	vector of unknowns (1.68)
$\boldsymbol{Y}$, $\tilde{\boldsymbol{Y}}$	vectors of unknowns (1.89) and (1.94)
ϕ	longitude
φ	incremental gravitational potential
φ_0	hydrostatic gravitational potential
φ_d	gravitational potential caused by deformation
φ_t	tidal potential
Φ	azimuth to the receiver
ϑ	colatitude
Θ	angular epicentral distance
χ	Coriolis splitting parameter
ω	angular frequency, eigenfrequency
${}_n\omega_l^S$, ${}_n\omega_l^T$	angular frequency of the spheroidal or toroidal mode
ω_0	fiducial angular frequency, angular frequency of the degenerated multiplet
ω_{ref}	reference angular frequency of the PREM
$\delta\omega$, $\delta\omega_m$	frequency perturbation
Ω	sidereal angular frequency